Revisiting the field geology of Taurus–Littrow

H.H. Schmitt [a,*], N.E. Petro [b,*], R.A. Wells [c], M.S. Robinson [d], B.P. Weiss [e], C.M. Mercer [f]

[a] Department of Engineering Physics, University of Wisconsin-Madison, P.O. Box 90730, Albuquerque, NM 87199-0730, USA
[b] Planetary Geology, Geochemistry, and Geophysics Laboratory, Code 698, Goddard Space Flight Center, 8800 Greenbelt Road, Greenbelt, MD 20771-2400, USA
[c] Tranquillity Enterprises, s.p., 445 Fairway Drive, Abingdon, VA 24211-3634, USA
[d] School of Earth and Space Exploration, Arizona State University, Box 871404, Tempe, AZ 85287-1404, USA
[e] Department of Earth, Atmospheric, and Planetary Sciences, Massachusetts Institute of Technology, 77 Massachusetts Avenue, Cambridge, MA 02139-4301, USA
[f] School of Earth and Space Exploration, Arizona State University, Box 876004, Tempe, AZ 85287-6004, USA

ARTICLE INFO

ABSTRACT

Integration of Apollo 17 field observations and photographs, sample investigations, Lunar Reconnaissance Orbiter Camera images, Chandrayaan-1 Moon Mineralogy Mapper (M^3) spectra, and Miniature Radio Frequency (Mini-RF) S-band radar images provides new insights into the geology of the valley of Taurus–Littrow on the Moon. Connecting the various remote observations to sample data enables a set of new conclusions to be drawn regarding the geological evolution of the valley. Structural considerations and published and recalculated $^{40}Ar/^{39}Ar$ analyses of samples from the North Massif and the Sculptured Hills indicate that the Crisium basin formed about 3.93 Ga; the Serenitatis basin about 3.82 Ga; and the Imbrium basin no earlier than 3.82 Ga and no later than the average of 3.72 Ga for 33 age dates from samples of the valley's mare basalts. Strong evidence continues to support the conclusion of others (Lucchitta, 1972; Spudis et al., 2011; Fassett et al., 2012) that the Sculptured Hills physiographic unit consists of Imbrium ejecta. Interpretation of M^3 spectral data and Apollo 17 samples indicate that rock units of the Sculptured Hills consist of a largely coherent, Mg-suite pluton. LROC NAC stereo images and Mini-RF data indicate the presence of several exposed pyroclastic fissures across the Sculptured Hills. Rim boulders at Camelot Crater constitute nearly in situ wall rocks of that crater rather than ejecta and provide an opportunity for investigations of remanent magnetic field orientation at the time of the eruption of late mare basalt lavas in the valley. Paleomagnetic field orientation information also may be obtained relative to melt-breccia contacts in North Massif boulders that suggest original horizontal orientations. LROC images indicate the existence of two temporally separate light mantle avalanche deposits. The origin, potential flow mechanisms, and geology of the youngest avalanche from the South Massif have been clarified. The existence of two distinct light mantle avalanches raises doubt about the association of either light mantle avalanche with secondary impacts related to the Tycho impact event. Alternatively, the Lee-Lincoln thrust fault appears to have triggered the second light mantle avalanche between 70 and 110 Ma. A simple structural analysis shows that this thrust fault dips 20–25° to the southwest where it crosses the North Massif and to the west where it crosses the valley floor. Mini-RF data reveal a line of reduced reflections roughly perpendicular to contours on the North Massif about 3 km to the east of the Lee-Lincoln fault. Although this line is possibly an older ancillary fault, LROC NAC stereo images indicate that it may be best explained as a pyroclastic fissure. A debris flow of dark, apparent pyroclastic ash lies below the southeast end of the potential fissure. Finally, young lunar impact glass sample 70019 has been precisely located within LROC NAC images and oriented for the first time using 60 mm (f.l.) sample documentation photographs. Sample 70019 can now be employed in lunar paleomagnetic field orientation studies.
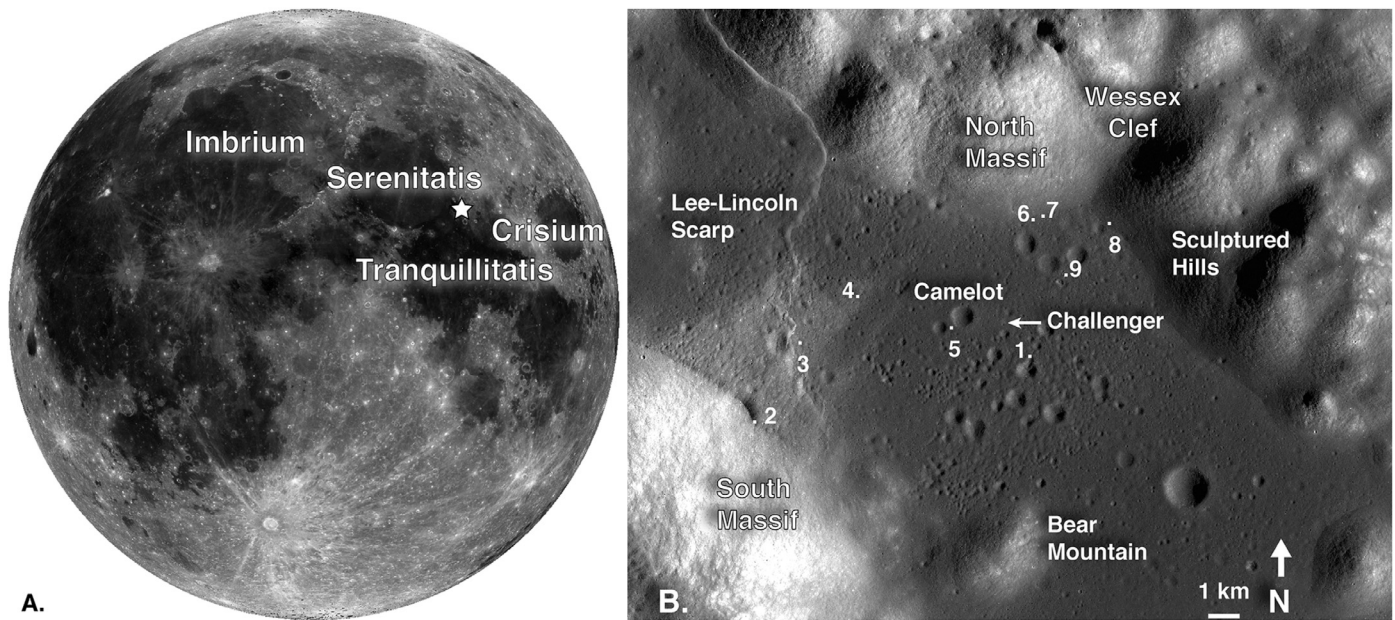
Published by Elsevier Inc.

1. Introduction

Apollo 17 astronauts explored the Taurus–Littrow valley on the Moon, December 11–14, 1972 (Schmitt, 1973). NASA's operational and scientific advisors recommended landing in the valley largely

Fig. 1. (A) LROC WAC nearside mosaic, showing the location of the Apollo 17 landing site (marked by a star) in the valley of Taurus–Littrow, as well as the four primary basins discussed in the text. (B) Overhead view of the valley of Taurus–Littrow showing key features described in the text. Numbered points are the major Apollo 17 exploration stations. Apollo 17 Orthorectified NAC mosaic, LROC Image M104311715LR.

because its rugged and multifaceted topography and apparently complex geological history provided fitting diversity for this last Apollo mission to the Moon (Fig. 1). During exploration of Taurus–Littrow, the astronauts examined, sampled and photographed the major physiographic features of the valley, including the North and South Massifs, the Sculptured Hills, Camelot Crater, the Lee-Lincoln Scarp, the "subfloor" basaltic lavas that underlie the valley floor, the dark mantle regolith and related pyroclastic ash deposits, and the light mantle unit that radiates from the northeast-facing slope of the South Massif. Various teams have reported extensively on the initial geological and experimental results from Apollo 17's observations, samples, photographs and deployed instruments. The interested reader should seek these reports for additional detail (e.g., NASA, 1973; Lunar Science Institute, 1973-present; Wolfe et al., 1981; Wilhelms, 1987; Heiken et al., 1991; Schmitt, 2003; Meyer, 2008).

Over four decades after completion of field observations and sampling activities in Taurus–Littrow, new orbital data sets provide opportunities for an enhanced understanding and reinterpretation of the geological underpinnings of the valley's physiographic features. Images and other remotely sensed information come from the Lunar Reconnaissance Orbiter Camera (LROC) (Robinson et al., 2010), Lunar Orbiter Laser Altimeter (LOLA) (Zuber et al., 2010), and Miniature Radio Frequency (Mini-RF) radar (Raney, R. K., 2007; Nozette et al., 2010; Raney et al., 2011) flying aboard NASA's Lunar Reconnaissance Orbiter (LRO); and the Moon Mineralogy Mapper (M^3) (Boardman et al., 2011; Green et al., 2011) that flew on India's Chandrayaan-1 spacecraft. Access to LROC Narrow Angle Camera (NAC) stereo images (Henriksen et al., 2017) provided unique high-resolution information on surface details of this locality's geological features.

We also reconsider a number of Apollo 17 samples for paleomagnetic field orientation studies. Recent data from lunar samples have shown that the Moon generated a dynamo magnetic field from at least 4.2 to 3.56 Ga and possibly extending to as recent as 1.3 Ga (Shea et al., 2012; Weiss and Tikoo, 2014). Because all of these studies worked with randomly oriented rock fragments from the lunar regolith, they were only able to measure the lunar magnetic field's paleointensity but not its paleodirection. New paleodirectional measurements could be used to test the

hypothesis that the magnetization in lunar rocks originated from a core dynamo. Studies of Earth rocks and magneto-hydrodynamic theory demonstrate that a lunar dynamo generated by convective cooling of the liquid core would be expected, on average, to be selenocentric, that is, oriented along the lunar spin axis, and predominantly dipolar (Merrill et al., 1998). This geometry is distinct from that of other postulated sources for lunar paleofields. For instance, fields from distant external sources like the solar wind or young Earth would be uniform and probably not oriented along the spin axis, while impact-generated or amplified fields (Hood and Huang, 1991) will be highly non-dipolar and vertically (or possibly randomly) oriented at the lunar surface.

This paper revisits the geological evolution of the Taurus–Littrow valley in light of its initial exploration, coupled with observations and interpretations related to recent remotely sensed datasets, new radiometric age determinations for several Apollo samples, and new insights based on over 44 years of work by a multitude of investigators. In particular, the new data from lunar orbit provide improved context for the samples and in situ data collected by Apollo 17 astronauts, enabling reinterpretation and expansion of earlier results from that mission.

2. North Massif stratigraphy - constraints on regional basin history

2.1. Geological setting

The North and South Massifs of Taurus–Littrow bound the east-southeast trending valley and lie a few tens of kilometers outside the inner edge of the principle rim of the Serenitatis basin, a 740 km diameter mascon basin (Fig. 1 and Wolfe et al., 1981; Stuart-Alexander and Howard, 1970; Hartmann and Wood, 1971; Head 1974, 1979; Wilhelms, 1987). The valley has a similar position with respect to Tranquillitatis, an older ~800 km diameter non-mascon basin roughly centered to the southwest (Wilhelms, 1987, Plate 4A). GRAIL data (Zuber et al., 2013) indicates nearly full, post-formation isostatic adjustment of Tranquillitatis and other irregular non-mascon basins as suggested by Schmitt (1989). Past photogeological mapping suggests that two, possibly simultaneous, impacts may have formed the Serenitatis basin
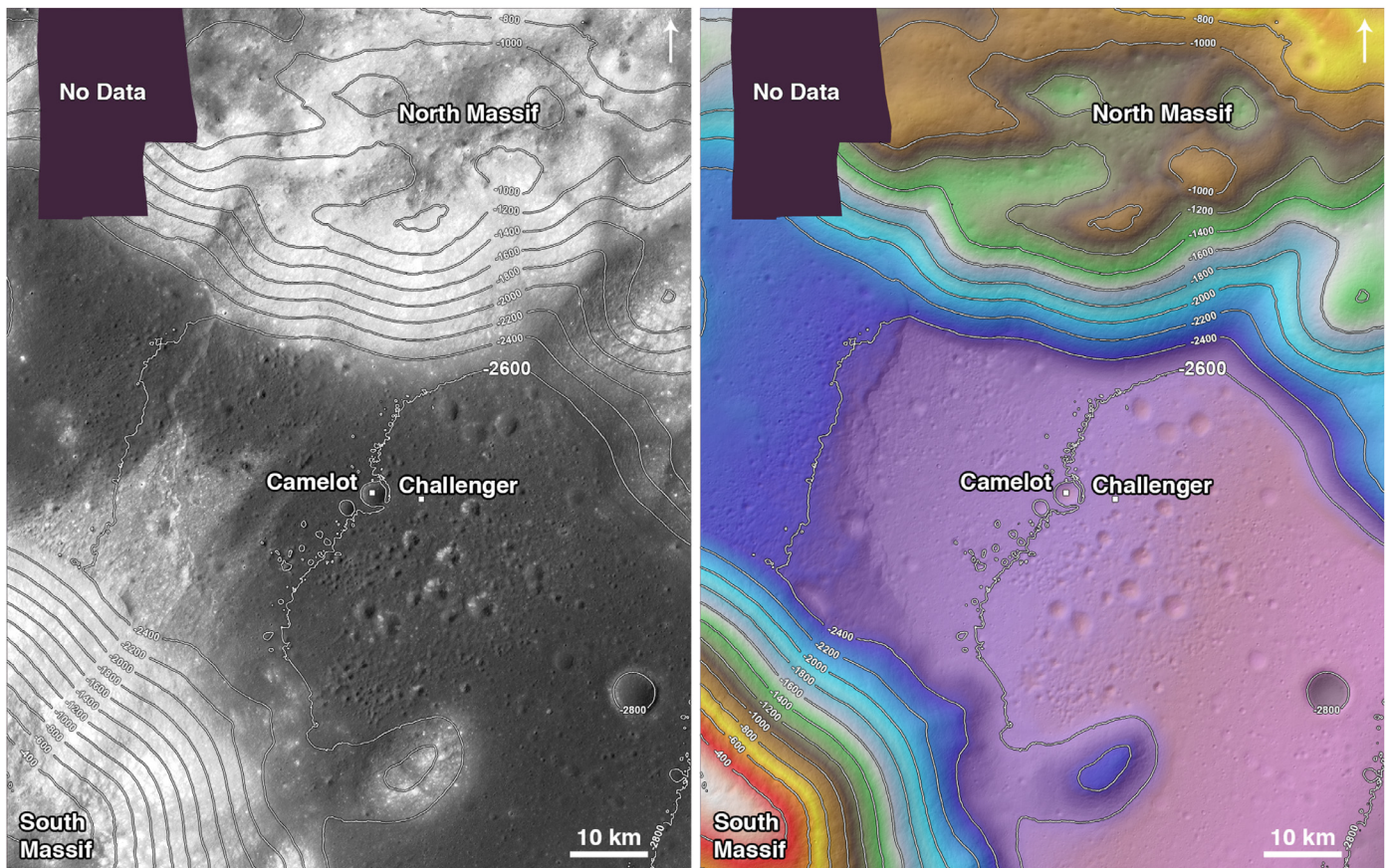
Fig. 2. LROC NAC Digital Terrain Model (DTM) for the Taurus–Littrow valley. At left, the contours (200 m contour interval) are plotted over the Apollo 17 Orthorectified NAC Mosaic. At right, the DTM is color coded to accentuate topographic variations within the North and South Massifs. The contour that passes near Camelot Crater is −2600 m.

(Wilhelms, 1987, p. 171) with gravity signatures of two impacts also suggested by GRAIL data. The area that includes the Taurus–Littrow Massifs and the Montes Taurus range to the north resembles a portion of a basin rim equivalent to the Montes Rook ring of the Orientale basin (Head, 1974; Wilhelms, 1987, p. 171; McCauley, 1981, p. 69. Fig. 4.4B). As the valley lies radial to the center of the primary Serenitatis basin, previous workers have interpreted it as being bound by a >50 km long fault graben system formed in response to dilation stresses produced by the Serenitatis impact event (Wolfe et al., 1981, p. 7). Similar radial valleys, bounded by massifs comparable to those of Taurus–Littrow, also cut across the Montes Rook ring of Orientale (McCauley, 1981, p. 69. Fig. 4.4B).

Previous photogeological mapping of this region, as well as studies of the Orientale basin, give strong indications that, along with ejecta from Serenitatis, ejecta from the Crisium (1060 km diameter and ∼550 km to basin edge) and the Imbrium (∼1165 km diameter and ∼750 km to basin edge) basin-forming impact events were deposited in the immediate area of Taurus–Littrow (Wilhelms, 1987, Plate 8A and 7A and p. 204 and 171–172). The probable existence of Crisium and Imbrium ejecta in this region also is consistent with early photogeologial mapping (Wilhelms, 1987, Plate 7A). Older events that contributed significantly to local basin ejecta stratigraphy (Wilhelms, 1987, p. 64–65) include Fecunditatis (∼990 km diameter and ∼650 km to basin edge) and a more controversial Procellarum (∼3200 km diameter and ∼300 km to possible basin edge). In addition, isolated material from more distant pre-Serenitatis basin-forming events may be present in the stratigraphic sections within the North and South Massifs as suggested by Petro and Pieters (2008).

Analysis of data from the Apollo 17 Seismic Profiling Experiment (Kovach et al., 1973) deployed during the Apollo 17 mission,

indicates that, after the irregular deposition of Imbrium ejecta, about 1.2 km of basaltic lava partially filled the center of the valley over which seismic charges were detonated. With this depth added to the current 1.6 km height of the North Massif, based on LOLA-derived topography and LROC photogrammetric elevations (Fig. 2), the pre-lava valley floor lay about 2.8 km below the summit of the North Massif. As will be discussed below, Imbrium ejecta probably contributed ∼ 100 m of pre-lava fill in the valley as well as larger masses that project as hills above that fill (e.g., Petro and Pieters, 2006; Fassett et al., 2011). The original valley depth relative to the North Massif summit, therefore, would have been significantly greater than 2.8 km.

2.2. Stratigraphic and structural analysis

Given early indications that the North Massif might contain stratigraphic units representing multiple basin-forming impact events, sampling boulders at its base became a high priority for Apollo 17 (Schmitt, 1973, p. 659). Upon landing, the crew could see a well-defined boulder track leading to the largest group of such boulders at planned Station 6 (Schmitt and Cernan, 1972, Post-Landing Activities, Ground Elapsed Time (GET) 113:09:18–113:09:47). High-resolution LROC images (Fig. 3) now show that both the large boulders sampled at the base of the Massif (Stations 6 and 7), as well as many other boulders, have tracks leading upslope. These tracks have their origins at concentrated sources of rock hundreds of meters above the current locations of the boulders (Schmitt and Robinson, 2010; Schmitt, 2013; Hurwitz and Kring, 2016). The upper termination of the rock sources from which the tracks initiate tend to be elongated coherent groupings of boulders, strongly suggesting that they comprise outcrops or
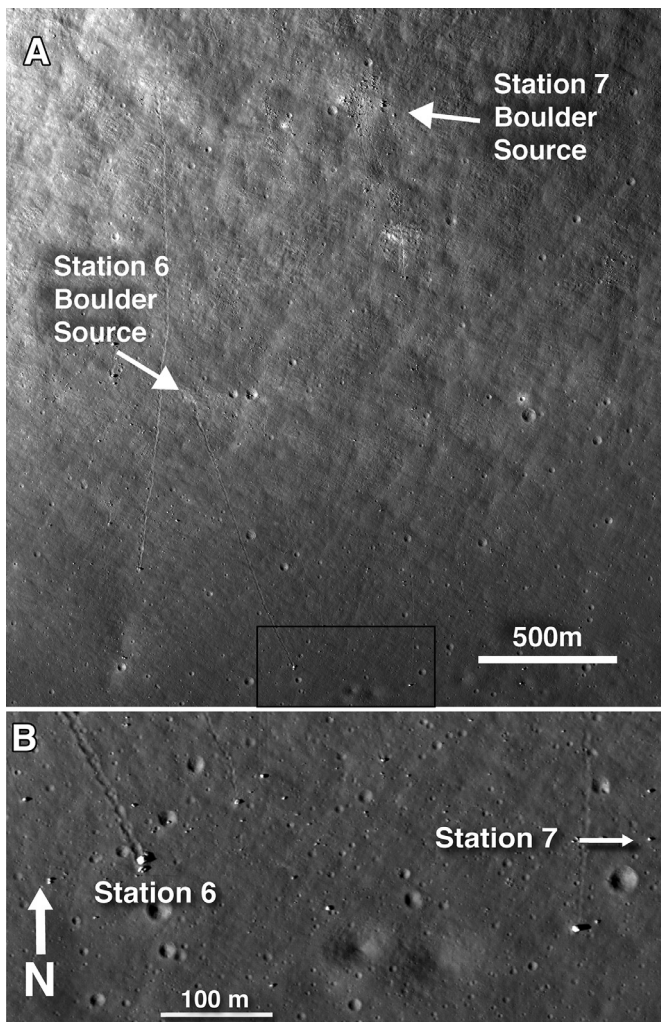
Fig. 3. Nadir view of the boulders sampled at Stations 6 and 7 (Fig. 1B) with boulder tracks down the southeastern flank of the North Massif (A). The boulders originated about 430 m and 930 m, respectively, above the floor of the Valley of Taurus–Littrow. Boxed in region in (A) shows enlarged view of Stations 6 and 7 in (B). The Station 7 boulder track is less well defined than the track leading to Station 6 due to its 8–15 Myr older age. LROC Image M134991788R.

near-outcrops ("source-crops"). Similar alignments of rock sources (Schmitt and Cernan, 1972, Post-Landing Activities, GET 113:10:36 to 113:11:16) exist along the northeast-facing slope of the South Massif (Fig. 4).

There are two primary physical constraints on the relative ages of major units of basin ejecta present in the North Massif that help the interpretation of sample data from the boulders. First, the materials comprising the Sculptured Hills physiographic unit (Fig. 4) are of Imbrian-age as they are superposed on the east and north borders of the Massif. As such, they constitute ejecta from the last major basin-forming event in this region of the Moon (Wilhelms, 1987, p. 195–226; Spudis et al., 2011; Fassett et al., 2012). LROC images of the plateau area on top of the North Massif (Fig. 5), however, appear to show significantly more craters of various diameters than are apparent on Sculptured Hills-style physiographic forms that surround the Massif. The cratered surface on top of the North Massif, therefore, seems to constitute a regolith surface developed prior to the Imbrium event.

Second, the pre-Imbrium stratigraphic section in the North Massif likely contains both Crisium and Serenitatis ejecta units due to the proximity of those basins. Indeed, early photogeological mappers (Wilhelms, 1987, Plate 7A) show the North and South

Massifs of Taurus–Littrow as a window in later basin ejecta that exposes older Crisium ejecta. We are not aware of any photogeological evidence that Crisium ejecta overlie ejecta from Serenitatis, or vice versa, but recognize that Imbrian ejecta may have locally obscured such evidence. Additionally, the apparently Serenitatis-related northwest-southeast graben fault cuts the North Massif (Head, 1974; Wolfe et al., 1981, p. 7). If this fault and its companions that bound the valley relate to the Serenitatis event, as postulated, and in the absence of ejecta superposition evidence to the contrary, the Crisium basin likely is older than Serenitatis (see also Wilhelms, 1981, p. 173). Any Crisium-age ejecta deposits in the North Massif, therefore probably underlie those of Serenitatis. We recognize that new image data have not been fully incorporated into regional photogeological mapping. Consequently, these conclusions remain subject to future revision.

This second tentative conclusion, that Crisium is older than Serenitatis, provides a framework for the interpretation of radiometric ages of samples (Section 2.3) from the North Massif stratigraphic section. Spudis et al. (2011) and Fassett et al. (2012), however, reach an opposite conclusion based on densities of what appear to be primary impact craters > 20 km in diameter on ejecta surfaces interpreted to be related to the two basins. This opposite conclusion implies that the fault-bounded structure of the valley of Taurus–Littrow is not of Serenitatis origin, as previously proposed (Head, 1974), but resulted from stresses imposed by either Imbrium or a Crisium basin-forming event that was younger than Serenitatis.

If the valley formed post-Serenitatis and is related to a possibly younger Crisium event or to the Imbrium event, it would likely have been modified or obscured by a combination of the ejecta from those events. Indeed, as discussed in Section 3, Imbrium ejecta, including the Sculptured Hills, covers portions of the area around Taurus–Littrow and partially fills the valley beneath the subfloor basalt. The top and south-facing slope of the North Massif and other major features defining the valley, however, remain unobscured. Also, the Imbrian-age Sculptured Hills appears to overlie the southeastward extension of the North Massif bounding fault, but no Crisium-related modification to the valley structures has been identified. Although a Crisium- or Imbrium-related origin of the valley structure that cuts an older Serenitatis basin rim may remain a possibility, it would seem unlikely in view of similar valley structures in the comparable Rook ring of Orientale, the youngest and least modified large impact basin (McCauley, 1981). The contradictory crater density data, reported by Spudis et al. (2011) that suggests the Serenitatis event occurred before the Crisium event may be explained by uncertainties in primary versus high angle (high velocity) secondary impact crater densities. Serenitatis also lies much closer to Imbrium than Crisium and the densities of high angle secondary impacts related to the Imbrium event generally would vary inversely with distance from Imbrium. This variation potentially would give an older crater count age for Serenitatis ejecta surfaces than for those related to Crisium. A definitive answer to this question awaits detailed photogeological mapping utilizing all the image and compositional data now available and a clear understanding of the spectra of trajectories and velocities of ejecta from large impact basins.

2.3. Sample data – stations 6 and 7 boulders

Comparison of LROC NAC images with LOLA topography (Fig. 2) show that the Station 6 boulder originated about 430 m above the valley floor. The LROC images also show that the relatively faint track leading to the boulder at Station 7 begins at an outcrop-like source about 500 m above the source of the boulder at Station 6. This subtle Station 7 track was not noticed from a distance or during the surface investigations at Station 7 and is significantly
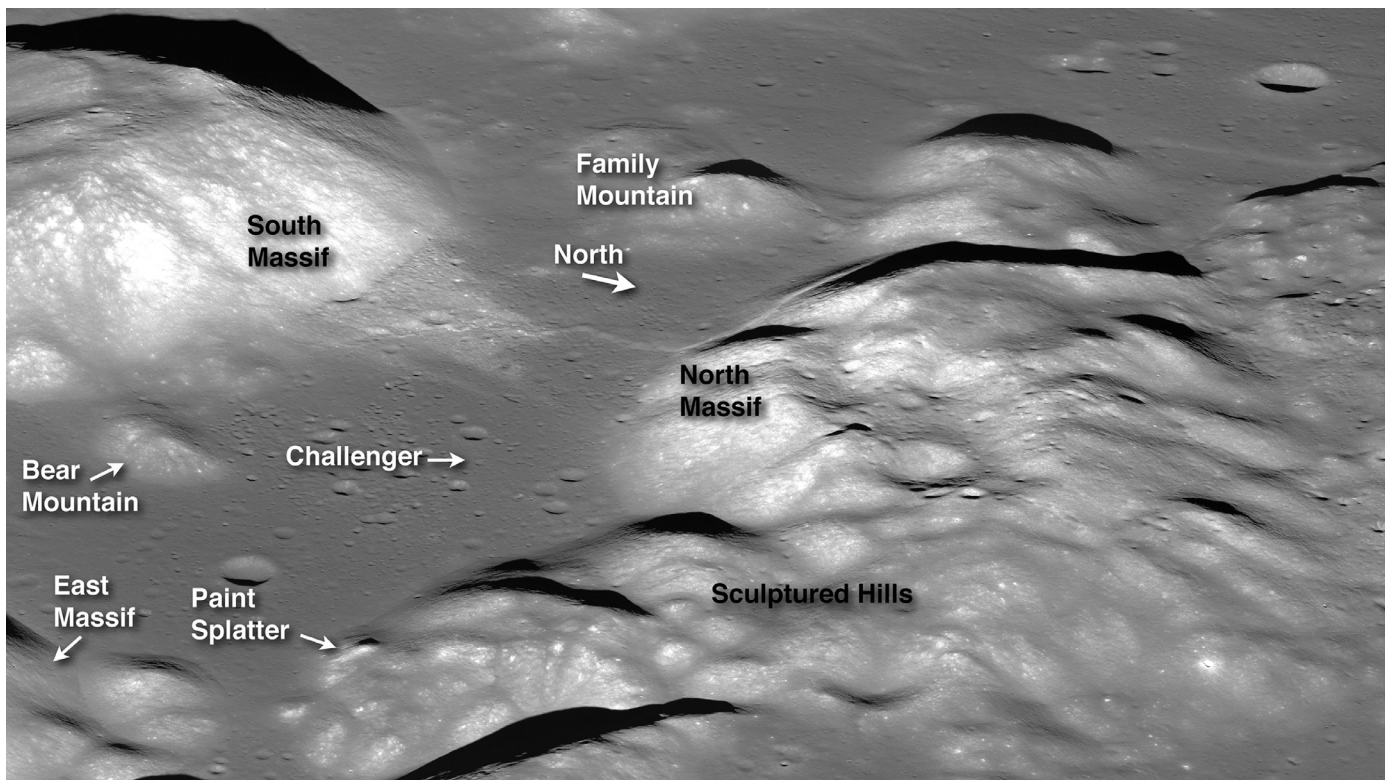
Fig. 4. East to west oblique view of the Taurus–Littrow area showing the distribution of Sculptured Hills' physiographic features to the south, east and north of the North Massif, partially surrounding an older cratered area on the North Massif plateau. The image also shows the low and high albedo light mantle units of the plume-like avalanche deposit projecting from the base of the South Massif in the center left and the "Paint Splatter" feature at the eastern portion of the Sculptured Hills. LROC Frame M1184583087LR.
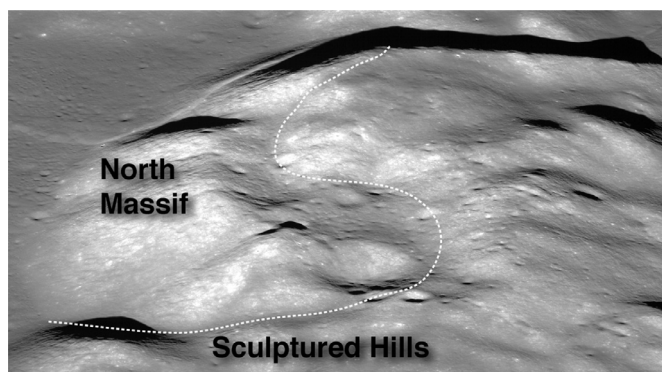
Fig. 5. Enlarged view of a portion of Fig. 4 illustrating the window of cratered, pre-Imbrium regolith on the plateau area of the North Massif, surrounded by relatively less-densely cratered Sculptured Hills material. The dotted white line marks the approximate boundary between the two surfaces. LROC image M1184583087LR.

less distinct than the track leading to Station 6. Exposure ages for the Station 6 and Station 7 boulders, 17–21 million years (Crozaz et al., 1974; Turner and Cadogan, 1975) and 25–32 million years (Stettler et al., 1974; Turner and Cadogan, 1975; Crozaz et al., 1974; Eberhardt et al., 1974), respectively, indicate that the difference in track definition results from about 10 million years longer exposure of the Station 7 track to impact degradation.

The blue-gray impact melt-breccias in the Station 6 and 7 boulders (Fig. 6) have very similar appearances in the field (Schmitt and Cernan, 1972, EVA-3, GET 164:53:11–165:35:52 and 166:09:51–166:21:39) and in thin sections. Post-mission examinations describe the two rocks (Meyer, 2008, samples 76295 and 77115) as polymict with an aphanitic matrix of intergrown plagioclase and clinopyroxene. The clasts in both samples consist of very fine-grained, crushed plagioclase-rich rock, fine-grained

dark breccia, and mineral fragments of plagioclase, olivine and orthopyroxene. Scattered vesicles and vugs are present in 77115, while these features appear to have collapsed into irregular void spaces in 76295. Both samples contain significant evidence of partial equilibration between compositionally diverse mineral clasts and the matrix to those clasts.

Table 1 and Fig. 7 summarize the ^{40}Ar/^{39}Ar age data available on samples from the Station 6 and 7 boulders. (All published ^{40}Ar/^{39}Ar data mentioned in this paper have been recalculated to use a consistent set of ^{40}K decay constants and monitor mineral ages. Details are given in Supplemental Methods. Analytical uncertainties are reported at the 2σ, ca. 95% confidence level unless otherwise noted.) The recalculated ^{40}Ar/^{39}Ar plateau age and 2σ uncertainty limits for the matrix of blue-gray melt-breccia 76295 are 3.915 ± 0.039 Ga. If this blue-gray melt breccia represents a single melt sheet in the North Massif, that unit may extend upwards several hundred meters above its source outcrop (Fig. 8). An ultraviolet laser ablation micro-probe (UVLAMP) ^{40}Ar/^{39}Ar date indicates that the Station 7 blue-gray melt-breccia 77115 solidified at 3.834 ± 0.020 Ga (Mercer et al., 2015). While this new estimate agrees within uncertainties with the recalculated plateau date for 77115 (3.854 ± 0.039 Ga) it is statistically distinct from the recalculated date for 76295. This important conclusion was checked in two ways: (1) with a test of the overlap probabilities (the OVL coefficient) between the 77115 and 76295 dates, and (2) null hypothesis testing with two-sample *t*-tests between the dates for 77115 and 76295. Both sets of statistical tests suggest that the dates for 77115 and 76295 are not equal. The plateau dates for 77115 and 76295 overlap by about 16% at 2-sigma, but not enough to be considered statistically identical.

The lack of overlap between the ages for similar blue-gray melt breccias in boulders at Station 6 and 7 may be the result of partial argon loss from 77115 due to heating by the adjacent, apparently
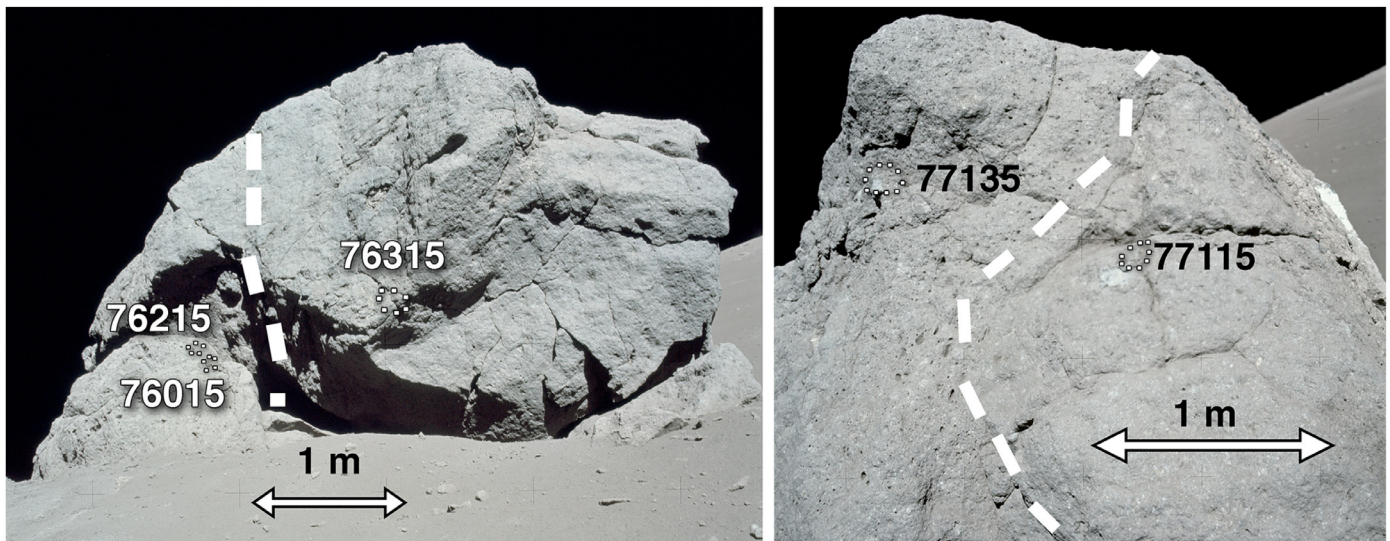
Fig. 6. Boulders at Stations 6 (left) and 7 (right) at the base of the North Massif showing the juxtaposition of blue-gray (right) and vesicular light-gray (left) impact melt-breccias in both boulders. Sampling locations for a number of the samples described in Fig. 7 are illustrated. Dashed lines indicate contact between blue-gray melt-breccia and light-gray melt-breccia in both boulders. Field observation disclosed an approximately 1 m wide, vesicular contact zone in the blue-gray melt breccia to the right of the contact in the boulder at Station 6. No similar contact zone is apparent to the right of the contact in the boulder at Station 7, however, similar $^{40}Ar/^{39}Ar$ ages indicate contact metamorphic equilibration across the contact. NASA Photographs AS17-140-21443 (left) and AS17-146-22305 (right).

Table 1
Summary of $^{40}Ar/^{39}Ar$ age data available on samples from the Station 6 and 7 boulders. Age dates for samples 1, 2, and 4–8 have been recalculated (Mercer, 2015) to use the decay constants of Steiger and Jäger (1977) and a consistent set of monitor mineral ages (see Supplemental Methods). The 2σ apparent age uncertainties represent full propagation of analytical uncertainties.

Sample	Recalculated $^{40}Ar/^{39}Ar$ Age (Ga)	2σ (Ga)	Probable basin of origin	Reference
76315,36 Blue-gray contact zone	3.934	±0.039	Crisium	Cadogan and Turner, 1976
76315,150A Blue-gray melt-breccia	3.933	±0.016	Crisium	Dalrymple and Ryder, 1996
76295,3 Blue-gray melt-breccia	3.915	±0.039	Crisium	Cadogan and Turner, 1976
76215,30 Light-gray melt-breccia	3.896	±0.039	Crisium	Cadogan and Turner, 1976
76015,38 Light-gray melt-breccia	3.886	±0.039	Crisium	Cadogan and Turner, 1976
77115,75 Blue-gray melt-breccia	3.854	±0.039	Senenitatis reset	Stettler et al., 1978
77115,121 Blue-gray melt-breccia	3.834	±0.020	Senenitatis reset	Mercer et al., 2015
77135,57 Light-gray melt-breccia (olivine-rich)	3.825	±0.048	Serenitatis	Stettler et al., 1978
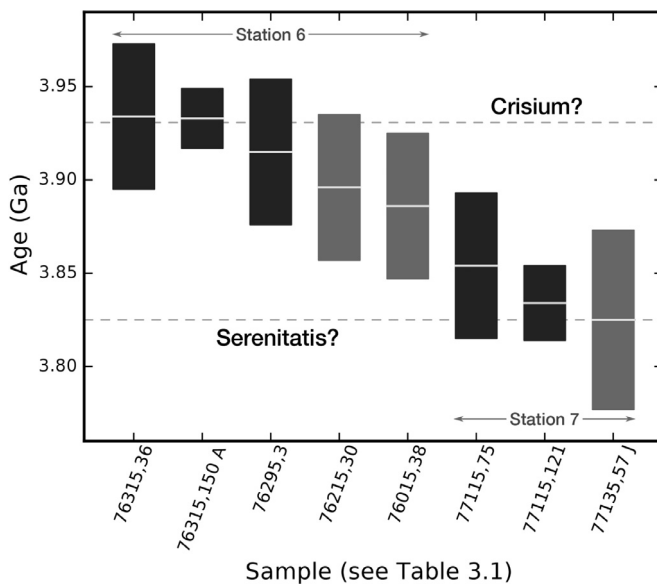
**Fig. 7.** $^{40}Ar/^{39}Ar$ dates for samples from the Station 6 and 7 boulders (Table 1), shown as the mean of ± 2σ analytical uncertainties. All dates are from incremental heating plateaux except for 77115,121, which is an isochron date from UVLAMP analyses. Black bars represent blue-gray melt breccias, while the gray bars represent light-gray melt breccias.

younger, vesicular light-gray melt-breccia (see Fig. 6). The vesicles in the light-gray melt-breccia are ovoid in shape, apparently flattened by viscous flow, and are aligned parallel to the contact. Also, as seen in Table 1, both the recalculated and newly measured ages for 77115 (3.854 ± 0.039 and 3.834 ± 0.020 Ga, respectively) lie within the 2σ uncertainty limits of the recalculated age of 3.825 ± 0.048 Ga for sample 77135 of the light-gray melt-breccia. These apparent ages are consistent with the Station 7 blue-gray melt-breccia having been annealed significantly by the partially molten light-gray melt breccia.

In addition to the clearly defined Imbrium source of Sculptured Hills materials discussed in Section 3, Imbrium melt-breccia might have been draped over the Taurus–Littrow massifs and valley and possibly reset the $^{40}Ar/^{39}Ar$ system. The primary evidence that this did not occur comes from the heavily cratered material that covers a physiographic window in the top plateau area of the North Massif (Fig. 5). This older cratered terrain appears to be partially surrounded by and to underlie the Imbrium-derived Sculptured Hills materials. In addition to the lack of evidence of a draped unit on the relatively uniform slopes of the North and South Massifs, the boulder sources exposed on that slope, as discussed above, appear to reflect a roughly planar internal structure rather than the remnants of a draped melt unit (see Fig. 8). Additionally, as also discussed in Section 3.3, Imbrium ejecta in the Taurus–Littrow region, as represented by the Sculptured Hills, does not appear to consist of melt-breccia, although this type of Imbrium ejecta may not have been recognized to date.
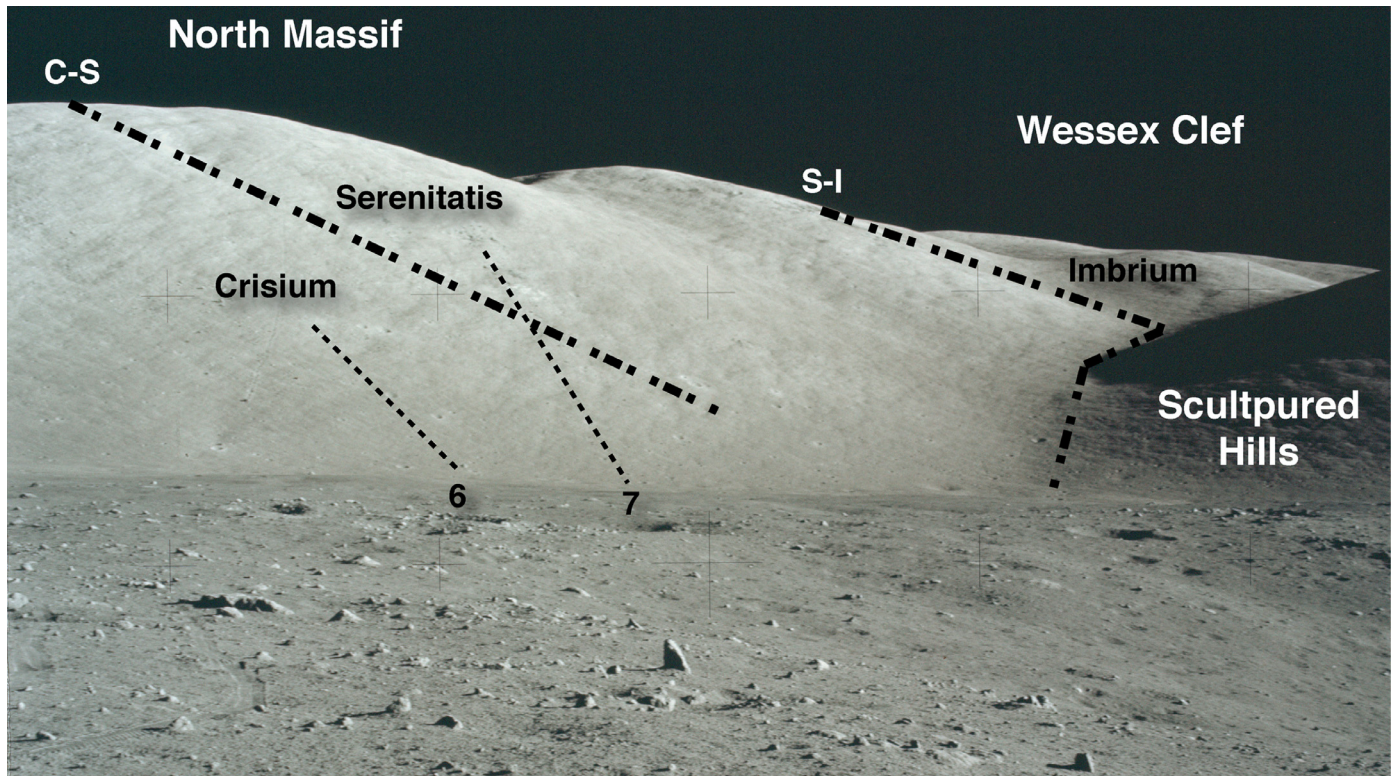
Fig. 8. Postulated contacts between major ejecta units that constitute the North Massif and the Sculptured Hills. Elevation of the left crest of the North Massif above the valley floor is about 1600 m. Numbers 6 and 7 refer to boulders sampled at Stations 6 and 7. Dotted lines indicate approximate trace of tracks leading to Station 6 and 7 boulders. The left dash-dot line denotes the inferred contact between Crisium and Serenitatis ejecta (C-S) based on the topographic break along that line. This inferred contact is consistent with the sources and $^{40}Ar/^{39}Ar$ plateau and isochron dates for samples from Stations 6 and 7. The right dash-dot line denotes the inferred contact between Serenitatis and Imbrium ejecta (S-I) based on the mapped boundary between the North Massif and the Sculptured Hills. Note that, on both sides of the inferred contacts, lineaments roughly parallel each. Based on the 25° apparent plunge of the contacts, and a comparison of the elevation of the North Massif with the difference in apparent elevation of the two contacts, the inferred thickness of Serenitatis ejecta is greater than a kilometer. NASA Photo AS17-134-20430.

As noted above, the blue-gray melt-breccia unit in the Station 7 boulder is in contact with younger light-gray melt-breccias (see Fig. 6). This also is the case in the Station 6 boulder (Fig. 6); however, samples of the two boulders are petrographically distinct. Based on the compilation of Meyer (2008, samples 76015 and 76215), the Station 6 light-gray melt-breccia consists of micro-poikilitic, very coarsely vesicular melt-breccia. The matrix is a very fine-grained tabular plagioclase enclosed in pigeonite (poikilitic texture). The matrix and the pigeonite crystals also contain rounded augite grains. Minor olivine, ilmenite, armalcolite and metallic iron are concentrated between pyroxene crystals. Mineral and rock clasts amount to 5–15% and vesicles amount to about 20% of the samples. A meter-wide vesicular contact zone in the blue-gray breccia indicates that the light-gray melt-breccia had sufficient heat to partially melt the relatively older blue-gray breccia. It is not clear, however, whether the light-gray melt-breccia intruded the pre-existing blue-gray melt-breccia or was deposited on an exposed surface with removal or assimilation of any pre-existing regolith.

In contrast to this petrographic characterization of the Station 6 light-gray melt-breccia, post-mission examinations of 77135 (Meyer, 2008, sample 77135) from the Station 7 light-gray melt-breccia, show that its clasts consist of olivine aggregates (dunite); plagioclase-rich, partially recrystallized crushed rock; and fragments of plagioclase and olivine. These clasts are in a highly vesicular matrix made up of clinopyroxene crystals (pigeonite and augite) that enclose fine-grained plagioclase and olivine (poikilitic texture). In the field, this melt-breccia resembles the light-gray melt-breccia samples from the boulder at Station 6; however, the Station 6 light-gray melt-breccia samples are distinguished by the

presence of only minor olivine versus about 15% olivine in 77135. These petrographic contrasts, however, suggest that the Station 6 and Station 7 light-gray melt-breccias were derived from significantly different target sources. Contrasts in bulk chemical composition between samples of the two breccia units, on the other hand, do not appear to be outside the probable error in those analyses.

The matrices of samples of the Station 6 light-gray melt-breccia, 76015 and 76215, have recalculated $^{40}Ar/^{39}Ar$ plateau dates of 3.886 ± 0.039 and 3.896 ± 0.039 Ga, respectively. These dates and their 2σ uncertainties are consistent with the light-gray melt-breccia being penecontemporaneous with the adjacent blue-gray melt-breccia, 76295 (3.915–3.854 ± 0.039 Ga; Cadogan and Turner, 1976). The apparent partial re-melting and annealing of blue-gray melt-breccia (76315) in the vesicular contact zone indicates the blue-gray melt-breccia may have had its argon isotopic system fully reset. Recalculation of the $^{40}Ar/^{39}Ar$ age for 76315 gives 3.934 ± 0.039 Ga (Cadogan and Turner, 1976). $^{40}Ar/^{39}Ar$ age determinations for 76315, using a "continuous laser system" on very small fragments gave a recalculated age of 3.933 ± 0.016 Ga (Dalrymple and Ryder, 1996). Both these ages for 76315 also are consistent (within 2σ uncertainties) with the similar recalculated dates for Station 6 blue-gray and light-gray melt-breccias.

In contrast to the apparent ages of the Station 6 light-gray melt-breccia, the matrix of Station 7 light-gray melt-breccia sample 77135 has a recalculated $^{40}Ar/^{39}Ar$ age of 3.825 ± 0.048 Ga (Stettler et al., 1978). This date appears younger than the two dates determined for 77115 (Fig. 7) from the adjacent blue-gray melt-breccia, possibly due to incomplete resetting of the K-Ar isotopic system in 77115 by contact metamorphism. The absence in the Station 7 boulder of blue-gray melt-breccia that might
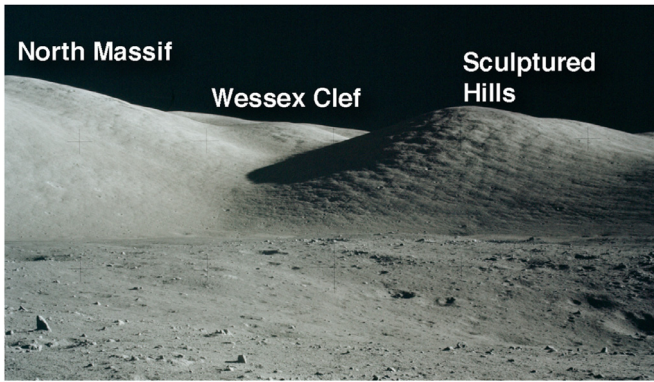
Fig. 9. Surface view from the southwest to northeast of Wessex Clef with the North Massif on the left and the Sculptured Hills on the right. The crest of the North Massif is approximately 1600 m above the valley floor. Intersecting ocean swell-like lineaments with a 100–200 m wavelength are visible on the facing slope of the Sculptured Hills. NASA Photograph AS17-134-20431.

be unmetamorphosed leaves open the possibility that the two melt-breccias in that boulder also might be penecontemporaneous.

Light gray melt-breccia 77135, with a recalculated date of 3.825 ± 0.048 Ga, also appears to be about 100 million years younger than the blue-gray melt-breccias at Station 6, a difference lying outside 2σ uncertainties for the dates on blue-gray melt-breccia samples (weighted mean of 3.93 Ga). In fact, the 77135 date is statistically distinct from the dates of all of the Station 6 blue-gray and light-gray breccias. Based on these data, the Station 7 light gray melt-breccia (77135) appears to have originated from an impact event younger than that represented by the Station 6 blue-gray and light-gray melt-breccias. Based on discussions in Section 2.2, we postulate that the younger of these events formed Serenitatis. The $^{40}Ar/^{39}Ar$ age of the Station 7 blue-gray melt-breccia apparently has been reset close to that of Serenitatis by proximity to the younger light-gray melt-breccia.

2.4. North Massif stratigraphic summary

Fig. 8 shows an interpretation of the proposed stratigraphic relationships in the North Massif and Sculptured Hills superposed on a photograph taken from the lunar surface. A sloping, topographic ramp, with an apparent ~25° surface plunge to the east, may reflect the contact between Crisium ejecta and overlying Serenitatis ejecta. That possibility is consistent with the relative sources and ages of the boulders sampled at Stations 6 and 7. An apparently parallel and much more pronounced topographic break (Wessex Clef, Figs. 1 and 9) exists at the previously mapped boundary (Lucchitta, 1972) between the North Massif and the Sculptured Hills. As discussed above (Section 2.2), we interpret this upper boundary to be the contact between Imbrium ejecta and older ejecta units.

The apparently younger age of the Station 7 light-gray melt-breccia 77135 relative to Station 6 samples, its higher stratigraphic source in the North Massif, and its olivine-rich impact target source suggest that the Station 7 breccia constitutes ejecta from the upper portion of the North Massif stratigraphic section. If so, that younger melt arrived on top of Station 6/7 blue-gray ejecta with sufficient energy to remove or assimilate a few tens of million years of accumulated regolith, as no obvious residual regolith is apparent at the contact exposed in the Station 7 boulder. The same lack of evidence of residual regolith exists at the contact in the boulder at Station 6; however, age data suggests little time lapsed between emplacements of the two contrasting melt-breccias in that boulder. The strong foliation shown by vesicles in both Station 6 and 7 light-gray melt-breccias is consistent with

high-energy deposition and flow of these impact melts. In this regard, LROC images have documented extensive, clearly defined flows of impact melt elsewhere on the Moon (Bray et al., 2010; Denevi et al., 2010; Plescia and Spudis, 2014).

High pressure injection of impact melt and its movement as intrusive magma away from the area of impact also should be considered as a possible explanation for the contact relationships noted between light-gray melt-breccia and blue-gray melt-breccia at both Stations 6 and 7. Radial and concentric extension fractures such as those that bound the valley of Taurus–Littrow could provide channels for movement of intrusive impact melt. We are not aware of definitive evidence of surface eruptions of intrusive impact melt related to large basin formation; however, future studies should investigate this possibility.

Given relative age relationships, the Station 6 blue-gray and light-gray melt-breccias and the Station 7 blue-gray breccia probably originated with the Crisium event and the Station 7 light-gray melt-breccia with the Serenitatis event. If these correlations prove correct, then about 700 m of post-Crisium Serenitatis ejecta lie vertically above the source of the Station 7 boulder. Additional radioisotopic dating of melt-breccia matrices from Stations 6 and 7 and other breccia samples from North Massif regolith may refine ages within this North Massif stratigraphic sequence.

If the Station 6 and 7 light-gray melt-breccias were deposited on older surfaces of blue-gray melt-breccias, these surfaces probably were roughly horizontal. If so, then light-gray melt-breccia samples 76015, 76215 and 77135, and blue-gray melt-breccia samples 76255, 76275, 76295 and 77115 present targets for paleodirectional measurements of magnetic fields at the time of their cooling. Using photogrammetric techniques discussed and illustrated in Section 7, photographic documentation should be sufficient to establish the original orientations of these samples in the Station 6 and 7 boulders as well as subsequent rotation of such orientations to the horizontal. If paleomagnetic field measurements for the samples are consistent within the age range of the samples, this would support the hypothesis that the contacts in the boulders are ejecta contacts and, in comparison with other potential measurements (Section 4.2), may help determine the in situ attitude of the contacts. Additionally, future textural analyses of vesicle and mineral orientations in the samples and photographs also may provide information related to the question of original contact orientation.

In summary, available new and recalculated age data, physiographic relationships, and photogeological mapping (Wilhelms, 1987, Plate 7A) suggest the following sequence of large basin-related events in the immediate vicinity of the North Massif:

1. Aggregation of basin ejecta that constitutes pre-Crisium terrain.
2. Deposition of Station 6 and 7 blue-gray melt-breccia [early arriving ejecta from the Crisium event [about 3.93 Ga].
3. Deposition of Station 6 vesicular light-gray melt-breccia [late arriving ejecta from the Crisium event].
4. Serenitatis rim uplift and deposition of 100s of meters of Serenitatis-age blue-gray and light-gray melt-breccias [about 3.83 Ga].
5. Graben faulting to form the valley of Taurus–Littrow and expose both Crisium and Serenitatis ejecta in the North Massif [delayed response to Serenitatis event].
6. Deposition of Imbrium age Sculptured Hills to the north, northeast and east of the North Massif and in the valley [3.83 – 3.72 Ga]. The minimum age for the Imbrium basin-forming event is based on the average of various isotopic age determinations for post-Imbrium basalt samples collected in Taurus–Littrow (Table 2).

The overall geological relationships discussed above establish a plausible relative formation sequence for the Crisium, Serenitatis and Imbrium basin-forming events, in that order. Clearly, however,

Table 2
Summary of age dates of subfloor basalt samples provided by Meyer (2008). ^{40}Ar/^{39}Ar age dates are recalculated as described in Section 2.3 and Supplemental Methods. Although the range of age dates is large, the average age for all measurements is 3.72 Ga; for ^{40}Ar/^{30}Ar (14 reports) is 3.74 Ga; for Rb-Sr (15 reports) is 3.70 Ga; and for Sm-Nd (4 reports) is 3.73 Ga.

Sample	Method	Age (Ga)	Reference
70017,65	^{40}Ar/^{39}Ar	3.772	Phinney et al., 1975
70017,25,67	^{40}Ar/^{39}Ar	3.805	Schaeffer et al., 1977
70035,6	^{40}Ar/^{39}Ar	3.699	Stettler et al., 1973
70215,21	^{40}Ar/^{39}Ar	3.783	Kirsten and Horn, 1974
70215,182,65	^{40}Ar/^{39}Ar	3.795	Schaeffer et al., 1977
75035	^{40}Ar/^{39}Ar	3.722	Turner and Cadogan, 1974
75055,11,2	^{40}Ar/^{39}Ar	3.753	Kirsten et al., 1973
75055	^{40}Ar/^{39}Ar	3.722	Turner et al., 1973
75055 plag	^{40}Ar/^{39}Ar	3.741	Huneke et al., 1973
75075,84	^{40}Ar/^{39}Ar	3.687	Horn et al., 1975
75075,84 etched	^{40}Ar/^{39}Ar	3.658	Horn et al., 1975
75075,84 plag	^{40}Ar/^{39}Ar	3.687	Horn et al., 1975
78503,13,B	^{40}Ar/^{39}Ar	3.774	Kirsten and Horn, 1974
79155,24	^{40}Ar/^{39}Ar	3.745	Kirsten and Horn, 1974
70017,35	Rb-Sr	3.60	Nyquist et al., 1975
70035,9	Rb-Sr	3.74	Evensen et al., 1973
70035,6	Rb-Sr	3.65	Nyquist et al., 1974
70135	Rb-Sr	3.67	Paces et al., 1991
71055	Rb-Sr	3.54	Tera et al., 1974
71539,6	Rb-Sr	3.67	Paces et al., 1991
74255	Rb-Sr	3.63	Paces et al., 1991
74255	Rb-Sr	3.75	Paces et al., 1991
74275	Rb-Sr	3.77	Murthy and Coscio, 1977
74275	Rb-Sr	3.73	Paces et al., 1991
75035	Rb-Sr	3.75	Paces et al., 1991
75055	Rb-Sr	3.75	Tatsumoto et al., 1973
75055	Rb-Sr	3.69	Paces et al., 1991
75075	Rb-Sr	3.76	Paces et al., 1991
75075	Rb-Sr	3.78	Paces et al., 1991
70135	Sm-Nd	3.77	Nyquist et al., 1979
70139	Sm-Nd	3.71	Paces et al., 1991
71539,6	Sm-Nd	3.75	Paces et al., 1991
75075	Sm-Nd	3.70	Lugmair et al., 1975

within measurement limits, overlap exists between the published ^{40}Ar/^{39}Ar ages of most North Massif samples. Dates for Station 6 and 7 melt-breccias without 2σ uncertainty bars appear to indicate that the Crisium event occurred about 3.93 Ga, Serenitatis about 3.83 Ga, and Imbrium at a geologically brief time after Serenitatis (see Section 2.3). Several modern laboratories have undertaken the task of re-evaluating and re-determining ^{40}Ar/^{39}Ar ages reported during early examination of Apollo samples, using more precise standard comparisons and laser ablation techniques. Laser ablation allows the analysis of very small areas of thin-sections, thus avoiding contamination from rock and mineral clasts that have older relic ages. For example, the new UVLAMP ^{40}Ar/^{39}Ar age for the matrix of blue-gray melt-breccia sample 77115, discussed above, is 3.834 ± 0.020 Ga (Mercer et al., 2015) versus earlier determinations of about 3.854 ± 0.039 Ga. Unfortunately, until the ages of true melt matrices of other samples of Station 6 and 7 melt-breccias are re-examined, no firm conclusions can be reached on their relative and absolute ages. In addition, new determinations of ^{40}Ar/^{39}Ar ages of melt-breccias from the South Massif collected at Stations 2 and 3 will bear on overall strati-graphic interpretations for the Taurus–Littrow region as a whole.

3. Sculptured Hills

3.1. Geology of the Sculptured Hills

The Sculptured Hills physiographic unit forms the eastern part of the north boundary of the valley of Taurus–Littrow (Lucchitta, 1972), separated from the North Massif on the west by a pronounced, northeastward rising valley called Wessex Clef (Figs. 1 and 9). The Sculptured Hills unit does not appear to have been cut by the north graben faults that bound the valley. Rather, the

unit probably covers one or more such faults. In sharp contrast to the relatively even, continuous slopes and cratered upper plateaus that characterize the North and South Massifs, the Sculptured Hills consist of rounded knobs on a scale of a few kilometers wide and a few hundreds of meters high (Figs. 2, 4 and 10). High-resolution LROC images show that fields of boulders cover large portions of the upper slopes of individual hills.

In the Taurus–Littrow study area, the Sculptured Hills physiographic map unit constitutes an area approximately 10 km by 15 km. Similar hills, however, surround the North Massif on the north and west and project through the valley floor. Based on M^3 spectra, Family Mountain, Bear Mountain, a northwestern foothill to the East Massif, and the East Massif itself appear to comprise additional Sculptured Hills material (Fig. 12).

Unlike pre-Apollo 17 images of the North Massif, early images of the Sculptured Hills resolved no boulders or ledges on their slopes and no boulder accumulations at their bases. The only obvious surface anomaly consisted of a bright irregular spot, resembling a paint splatter, on the top of a single knob at the southeastern corner of the unit. Pre- and immediate post-mission speculation (Wolfe et al., 1981, Plate 2) as to the nature and origin of material making up the Sculptured Hills generally centered on their formation from late ejecta from the Serenitatis Basin, although early photogeological mapping (Luchitta, 1972; Wilhelms, 1987, Plate 8A and p. 204) included the area as discontinuous ejecta from Imbrium.

LROC images now show that no younger basin ejecta cover the Sculptured Hills. Based on the geologic relationships between the Sculptured Hills and the North Massif described above, we conclude, as have others (Lucchitta, 1972; Spudis et al., 2011; Fassett et al., 2012), that the Sculptured Hills consist of Imbrium Basin ejecta that arrived both after ejecta from earlier basins covered the region and graben faulting had defined the Taurus–Littrow valley.

An east to west oblique view of the region around Taurus–Littrow (Fig. 4) provides a broad perspective of the distribution of Sculptured Hills-style surfaces. This physiographic unit appears to partially surround the North Massif on the east, north and west, leaving a more highly cratered summit plateau directly above the slope that forms the north wall of the valley. High trajectory Serenitatis and Imbrium ejecta may have cratered this plateau and accompanying regolith. Alternatively, an extended period of primary cratering may have followed Serenitatis, prior to the deposition of the Sculptured Hills. This distribution of features indicates that the Sculptured Hills arrived after the main units forming the North Massif were emplaced, some large craters had formed on its summit plateau, and the valley had been created by a complex arrangement of graben faults.

LROC images, as well as overhead photographs taken from lunar orbit by Apollo 17, show that the "sculpture" of the main body of the Sculptured Hills consists of linear swales that comprise roughly orthogonal, north-northeast to south-southwest and west-northwest to east-southeast trends (Fig. 10) (Schmitt and Robinson, 2010). The west-northwest to east-southeast trend in swales may define structural rather than compositional breaks in underlying deposits as they lie roughly radial to the Imbrium basin, Study of surface 60 mm (f.l.) Hasselblad photographs of the southwestern prominence of the Sculptured Hills, taken from about 5 km to the south at Apollo 17's Station 1 with a glancing sun angle (Fig. 9), also indicates the presence of two sets of broad wavelength (100–200 m), ocean swell-like lineaments. The most prominent lineament set trends approximately north-south, plunging south at about 20° to the slope. This lineament set also extends to more distant portions of the Sculptured Hills. The other, less prominent surface lineament set trends roughly northeast-southwest and may reflect the same structural trends as the northeast-southwest set of swales noted above. We note that
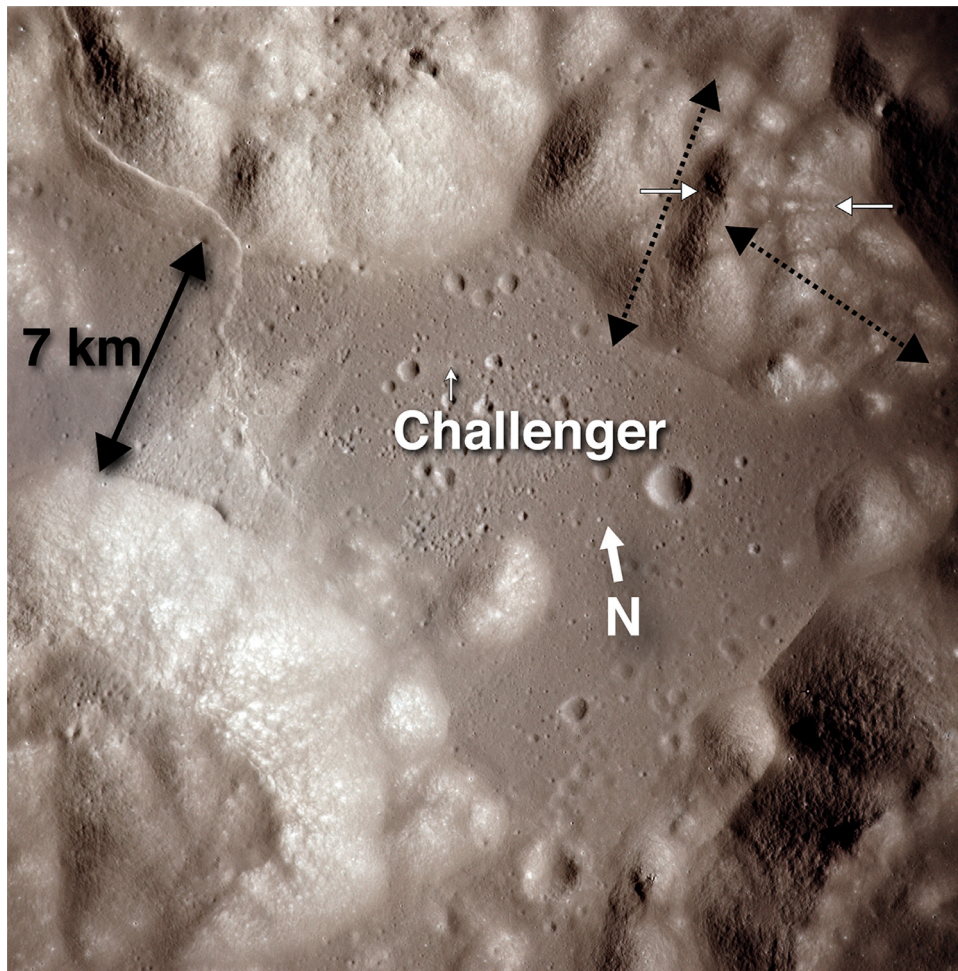
Fig. 10. North-northeast to south-southwest and west-northwest to east-southeast trends in the swales of the Sculptured Hills. The two white arrows within the Sculptured Hills indicate the approximate ends of the large pyroclastic fissure discussed in the text. NASA Apollo 17 Photograph AS17-151-23255.

other workers have interpreted images of small-scale lineaments as indicating lighting artifacts (Howard and Larsen, 1972). In the case of the lineaments shown in Fig. 9, however, their scale and apparent correlation with swale trends indicate structural controls.

3.2. Pyroclastic fissures in the Sculptured Hills

LRO's 12.6 cm wavelength Mini-RF data (Fig. 11) show reduced radar reflections in swales and other low areas of the Sculptured Hills. Even more highly reduced radar reflections exist along east-west trending elongate areas that cross local topography. The largest of these elongate areas is about 150 m by 4.7 km. These radar-dark areas also have very low albedo in LROC images taken at high sun angles. Examination of stereo pairs of LROC NAC images shows that these elongate dark areas cross ridges and knobs. Small impact craters in these dark areas have ejected low albedo material, even darker than the impacted surface, indicating that dark material extends several meters in depth. We postulate that these features are pyroclastic fissures, filled at least in part with ash similar to the black ash discovered at Shorty Crater (Schmitt, 1973; Meyer, 2008, sample 74001).

The location of these black ash fissures in the apparently highly fractured Sculptured Hills may be a consequence of late volatile-rich magma being diverted by the earlier basaltic fill in the valley into more accessible conduits under surrounding areas. The results of the Active Seismic Experiment deployed in the valley

(Kovach et al., 1973) do not indicate any detectable ash horizons in the ∼1200 m of basalt fill; however, the pure ash layers exposed at Shorty Crater (Station 4) and the 10–15% ash content of the dark mantle regolith indicate that some late pyroclastic eruptions occurred in the valley as well as in the surrounding highlands. Further definition of the distribution and dynamics of pyroclastic eruptions around southeastern Serenitatis warrants a regional comparison of Mini-RF data with LROC images.

Reduced radar reflections and visual albedo in swales throughout the Sculptured Hills probably indicate concentrations of black ash in the local regolith as suggested by Luccitta (1972). On the other hand, bright Mini-RF radar reflections from the crests and slopes of knobs reflect concentrations of decimeter or larger fragments in the regolith at these locations that can be sensed by the 12.6 cm radar.
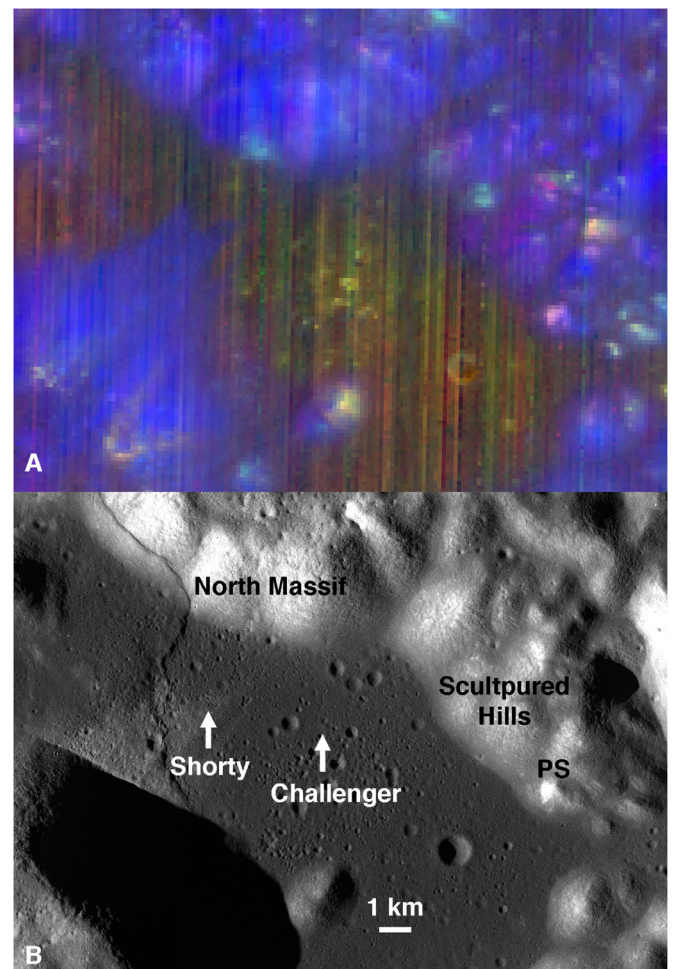
3.3. M^3 spectral Data: composition of the Sculptured Hills

Mineralogical information derived from M^3 near-infrared spectroscopic data (Green et al., 2011) adds significant insights about the internal structure and composition of the Sculptured Hills (Schmitt, 2014; Petro et al., 2015). These data confirm that complex rock units with varying mafic and anorthositic compositions underlie the regolith on the Sculptured Hills. Following suggestions by Robinson and Jolliff (2002) based on Clementine data, M^3 data indicate that the rocks contain varying amounts of plagioclase,
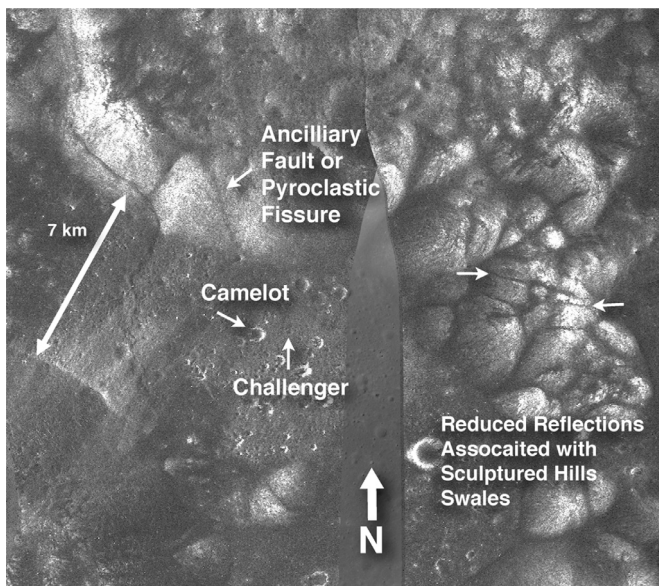
Fig. 11. LRO Mini-RF total power (S$_1$) images show reduced radar reflections associated with linear swales and other low areas in the Sculptured Hills. These reduced reflections may relate to the concentration of regolith fragments that are finer than those which can be sensed by the 12.6 cm radar wavelength of the Mini-RF. The two white arrows indicate the approximate ends of the large (∼150 m by 4.7 km) pyroclastic fissure discussed in the text. Bright Mini-RF 12.6 cm radar reflections are generally associated with the crests and slopes of knobs that indicate concentrations of significantly coarser fragments in the regolith at these locations. Mini-RF Frames LSZ_02595_1CD_XKU_17N031_V1 and LSZ_06589_1CD_XKU_10N031_V1. Mini-RF images overlay the LROC NAC Apollo 17 Orthomosaic.

orthopyroxene, olivine and clinopyroxene with anorthositic and gabbroic asseembleges possibly predominating (Klima et al., 2011; Staid et al., 2011). A M^3 color composite image (Fig. 12. See on-line issue for color image.) illustrates variations in mafic mineralogy using high-spectral resolution over the 1 and 2 μm regions that contain characteristic absorption features of common lunar mafic minerals. (The three-color composite shown in Fig. 12 uses the integrated band depth of the 1 μm region for the red channel, the integrated band depth of the 2 μm region for the green channel, and the albedo at 1.58 μm for the blue channel.)

Variations in the composition of the regolith developed on major geological features sampled during Apollo 17 traverses provide some calibration of the M^3 data for the Sculptured Hills. The clear definition in the color composite of the clinopyroxene-dominated basalt in and around the 100 m diameter Shorty Crater shows an image resolution of about 25 m per pixel. The greenish hues for the clinopyroxene-rich basaltic regolith (∼50% cpx, Wolfe et al., 1981; Meyer, 2008) over the valley floor, and for block concentrations in Camelot and Shorty Craters support the interpretation that M^3 green hues represent abundant clinopyroxene (gabbroic rocks). The bluish hues for the plagioclase-rich (25–30%, Wolfe et al., 1981; Meyer, 2008) regolith on the slopes of the North Massif support the interpretation that bluish hues represent plagioclase concentrations (anorthositic rocks). The deep blue area in the M^3 image at the crest of the large hill just east of Wessex Clef may indicate a high concentration of plagioclase and that the boulder fields Apollo 17 astronauts reported and photographed (Fig. 13) near that crest consist of anorthositic rocks. This is similar to what is seen in M^3 data on other basin massifs, for example, around the Orientale Basin (Cheek et al., 2013).

Other M^3 color interpretations cannot be derived directly from Apollo 17 samples; however, yellow and red hues in the color composite image (Fig. 12) are interpreted to show concentrations of orthopyroxene (norite) and olivine (dunite), respectively. Blue-green and pink hues indicate mixtures of

Fig. 12. M^3 false color image of the Sculptured Hills (top) from M^3 image M3G20090107T011405 (see on-line version). Color composite is based on the integrated band depth of the 1000 nm (Red) and 2000 nm (Green) bands and reflectance at 1580 nm (Blue). Key to color hues: yellow=orthopyroxene (gabbro to pyroxenite), blue=anorthite (anorthosite or anorthositic); green=clinopyroxene (norite); red=olivine (dunite); pink=anorthite plus clinopyroxene (gabbro); blue-red = anorthite plus olivine (troctolite). Bottom image is the LROC NAC Apollo 17 Orthomosaic.

plagioclase and clinopyroxene (gabbro) and plagioclase-olivine (troctolite), respectively. The colored areas in M^3 data generally correspond to clusters of boulders visible in high-resolution LROC NAC images.

The most prominent variations in M^3 color composite data show that, from crest to crest, knobs in the Sculptured Hills have distinct variations in the distribution of plagioclase, clinopyroxene, orthopyroxene and olivine. These variations appear to correspond to areas bounded by the roughly orthogonal physiographic trends of swales discussed above. Regolith surfaces below each knob show a gradual downward decrease in the concentrations of these minerals, likely the result of down-slope mixing and space weathering. The Mini-RF total power image in Fig. 11 also indicates concentrations of rock fragments on each knob as it shows a brighter 12.6 cm radar return from the crests than from the surrounding slopes and swales.

Prominent calibration artifacts (vertical lines) complicate extrapolation of the M^3 data (Fig. 12) except (1) where prominent color spots cross scan lines and correspond to topographic highs or, (2) where sharp linear breaks in color cross those scan lines. Apart from one linear break that correlates with a strong reduction in Mini-RF reflections (compare Figs. 11 and 12), these sharp linear

breaks in color follow the north-northeast to south-southwest trend in swale direction and delineate major internal mineralogical changes.

The M^3 data on mineral distributions reveal significant variation in composition over the relatively small area comprising the Sculptured Hills. They possibly define portions of an ejected, layered Mg-suite pluton composed largely of anorthositic rocks but with significant masses of gabbroic anorthosite, norite, clinopyroxenite and dunite (Schmitt, 2014). The available data, however, show only a few knobs that might consist of related outcrops or near outcrops of the same rock layer. Bear Mountain, Family Mountain, and the knob northwest of the East Massif also display multiple compositions, further connecting the origin of these features, now surrounded by basalt, to that of the Sculptured Hills. In contrast, such spectral variations are largely absent on most slopes of the North and South Massifs facing the valley providing an indication that those slopes are currently largely free of Imbrium ejecta deposits.

3.4. Sample data – stations 8 and 9 samples

Though not initially recognized as being from the Sculptured Hills, at least two sets of Apollo 17 samples may be related to Sculptured Hills material. These are Mg-suite samples collected at Apollo 17 Stations 8 and 9 (Fig. 1). Station 8 lies well within the mapped boundary of the unit (Luchitta, 1972), and the large norite boulder sampled there (Meyer, 2008, samples 78235, 78236 and 78238) supports the M^3 evidence of exposed plagioclase and orthopyroxene elsewhere in the Sculptured Hills (Schmitt, 2014; Petro et al., 2015). A fragment of an olivine-bearing (2%) norite, 78527, in the Station 8 rake sample, resembles the boulder norite samples in most respects and possibly is also a fragment of Sculptured Hills material. The Station 8 boulder is intensely fractured and largely glass coated, indicating an impact derivation. It consists of about equal parts plagioclase and orthopyroxene. The nearly complete glass coating (Fig. 14) indicates that this boulder came from a larger norite mass and is not the remains of a clast plucked from a Station 6- or 7-type breccia. Several 50–100 m diameter impact craters, that are possible sources for this glass-covered boulder, lie 1–2 km northeast to east-southeast of Station 8. A possibility exists that the norite boulder came from the boulder field on the knob above and to the north of Station 8 for which M^3 data suggests a noritic composition, although no boulder trail was identified during sampling or in documentation photographs. The krypton cosmic ray exposure age for 78235 of 292 ± 14 Ma (Drozd et al., 1977) indicates why any signs of the boulder's disturbance of the local regolith surface upon landing have disappeared. The lack of any remaining track or impact disturbance of the surrounding regolith contrasts with the continued presence of tracks associated with the boulders at Stations 6 and 7 where measured boulder exposure ages are about a factor of 10 less (17–21 and 25–32 million years, respectively).

^{40}Ar/^{39}Ar ages for the Station 8 norite of 4.39 (average of last 84% release) and 4.14 ± 0.02 Ga (Nyquist et al., 1981; Aeschlimann et al., 1982) appear not to have been fully reset by either the basin impact that delivered its host rock to the Taurus–Littrow area or the impact that moved the boulder to its present position. They approach the norite's apparent crystallization age of about 4.34 Ga, as indicated by consistent Rb-Sr, Sm-Nd, and Pb-Pb isotopic systems (Edmunson et al., 2009).

The impact excavation of Van Serg Crater at Station 9 (Fig. 1) probably exposed Mg-suite fragments underlying the regolith that had covered a Sculptured Hills-related knob projecting just above or lying just below the upper surface of the subfloor basalt covering the valley floor. Although regolith breccia samples from the rim of Van Serg are largely basaltic in composition (Meyer, 2008, 79515, 79516, 79121), only a few basalt fragments were

observed in the Van Serg impact ejecta, and breccia blocks on the floor contain large light-colored clasts (Schmitt and Cernan, GET 168:12:51). An apparently recrystallized Mg-suite troctolite sample from Van Serg ejecta, 79215 (Meyer, 2008, 79215), also is consistent with the M^3 indication of significant olivine as well as plagioclase at the surface of the Sculptured Hills (Fig. 12). Although much remains to be done to finalize and rationalize ^{40}Ar/^{39}Ar ages of all impact affected samples (Mercer et al., 2015), we note that a relatively young spot fusion date of 3.827 ± 0.040 Ga (measured by infrared laser probe) was reported for troctolite 79215 (Hudgins et al., 2008). Inasmuch as the incremental release spectrum of this analysis of 79215 did not yield a ^{40}Ar/^{39}Ar plateau, and other spot fusion dates ranged up to 4.034 Ga, it is likely that the ^{40}Ar/^{39}Ar system in 79215 was not fully reset by the latest impact affecting it. The 3.827 ± 0.040 Ga date could therefore represent a maximum age for Imbrium. This age would be consistent with the conclusion (within measurement limits) that Sculptured Hills-related materials constitute Imbrium ejecta as discussed in Section 2.2.

Other workers (Dalrymple and Ryder, 1993), applying ^{40}Ar/^{39}Ar laser step-heating methods to twelve Apollo 15 melt-breccias of possible Imbrium origin, concluded that Imbrium is no older than 3.87 Ga, and is probably no older than 3.836 Ga. Recalculation of the Dalrymple and Ryder data using decay constants and monitor ages consistent with those used throughout this paper would adjust these limits to about 3.90 Ga (firm upper limit) and 3.85 Ga (likely upper limit), respectively. One of these samples, however, has a recalculated ^{40}Ar/^{39}Ar age of 3.843 ± 0.016 Ga, which is statistically indistinguishable from the 3.825 ± 0.048 Ga date for Serenitatis inferred in Section 2.3. If this inference were correct, then Imbrium likely would be no older than about 3.83 Ga.

A number of dates attributed to the Imbrium basin-forming event, ranging between ca. 3.909–3.944 Ga, have been reported based on the Pb-Pb and U-Pb isotopic systematics of zircons and phosphates in lunar meteorites and Apollo 12, 14, and 17 samples (e.g., Gnos et al., 2004; Grange et al., 2009; Nemchin et al., 2009; Liu et al., 2012; Merle et al., 2014; Snape et al., 2016). Some of these dates have been variously interpreted to represent the ages of impact events that produced the Humorum, Serenitatis, and/or Imbrium basins. On the other hand, these interpretations of the ages of these basins, and of Imbrium in particular, are subject to the possibility that components of the breccias may have been formed or modified in one or more earlier impact events. Such relict components may have subsequently been incorporated into basin ejecta with little or no effect on the U-Pb systematics of zircons and phosphates. Combined U-Pb and ^{40}Ar/^{39}Ar datasets reported for lunar meteorite Sayh al Uhaymir 169 (Gnos et al., 2004) and Apollo 17 breccia 73217 (Grange et al., 2009; Mercer et al., 2015) provide examples of this possibility. We encourage more work to determine the absolute age of Imbrium and other basins; however, the available ^{40}Ar/^{39}Ar data from the North Massif melt-breccias provide a relatively consistent sequence of ages for three of the large basins, Crisium, Serenitatis and Imbrium, that contributed ejecta to the Taurus–Littrow region.

3.5. Paint splatter feature and granular debris flows

Another feature of note, superposed on the Sculptured Hills and imaged by Apollo 15, Apollo 17, and LROC (Fig. 15) is an irregular area of high reflectance material (1.5 to 2x higher than underlying material). It lies like paint splatter on and around a steep sided (slopes exceeding 32° in places), southeastern knob (20.116°N, 31.080°E). The high-resolution LROC images show that this bright material consists of multiple channels and tongues of high reflectance granular debris flows originating from near the top of the peak (Fig. 15). Sharply defined pairs of boulder levees exist throughout the paint splatter feature. We interpret the
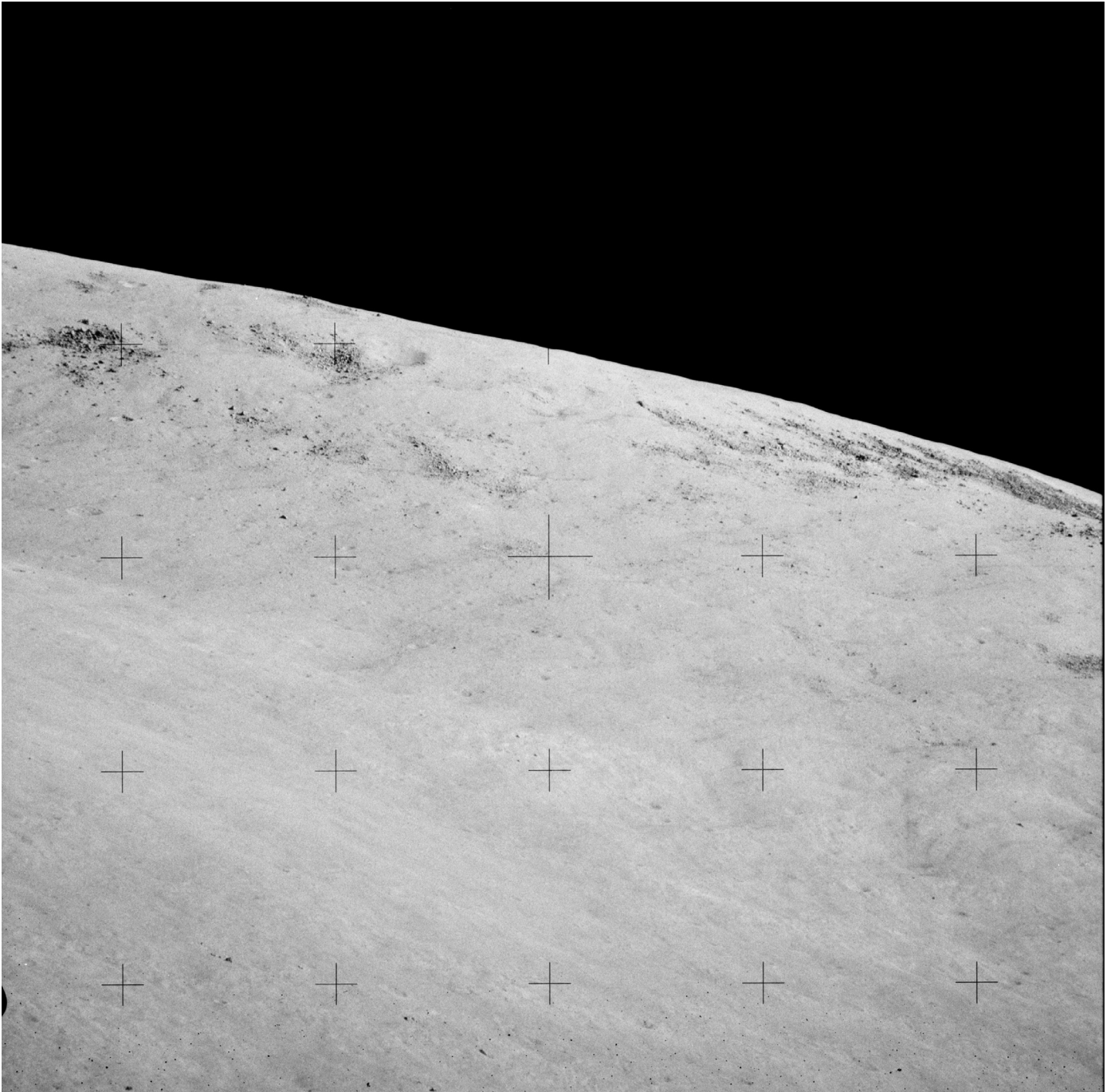
Fig. 13. Boulder fields of probable anorthositic and noritic rocks near the crest of the Sculptured Hills knob just east of the Wessex Clef. NASA Photograph AS17-144-22113.

debris flows to have different relative ages based on small albedo variations (∼30%) and overlapping flow patterns.

M³ data (Fig. 12) are not definitive on the mineral composition of the paint splatter material. If it were predominately plagioclase, a bluish hue would be expected. As the M³ color composite for this knob is pink, the parent rock may be an anothositic orthopy-roxenite. Examination of LROC NAC stereo pairs indicates that a few of the flows originate at small impact craters; however, in many cases no obvious impact triggers are apparent. Repeated seismic shocks, such as those associated with the formation of the Lee-Lincoln Scarp (see Section 6, below), also may have triggered many of these debris flows.

3.6. Sculptured Hills summary

In view of analysis of the LROC and M³ images and data, we interpret the boulder sampled at Station 8 to have originated from an impact on a noritic crystalline rock mass somewhere in the Sculptured Hills. The 4.34 Ga crystallization age (Edmunson et al., 2009) determined for this norite probably relates to a portion of a large layered igneous intrusive, ejected about ∼3.8 billion years ago from the lower crust by the Imbrium impact and ballistically transported as a fractured but largely intact single unit to the Taurus–Littrow area. This mass arrived prior to the eruption and solidification of the main mass of valley basalt (subfloor), loosely
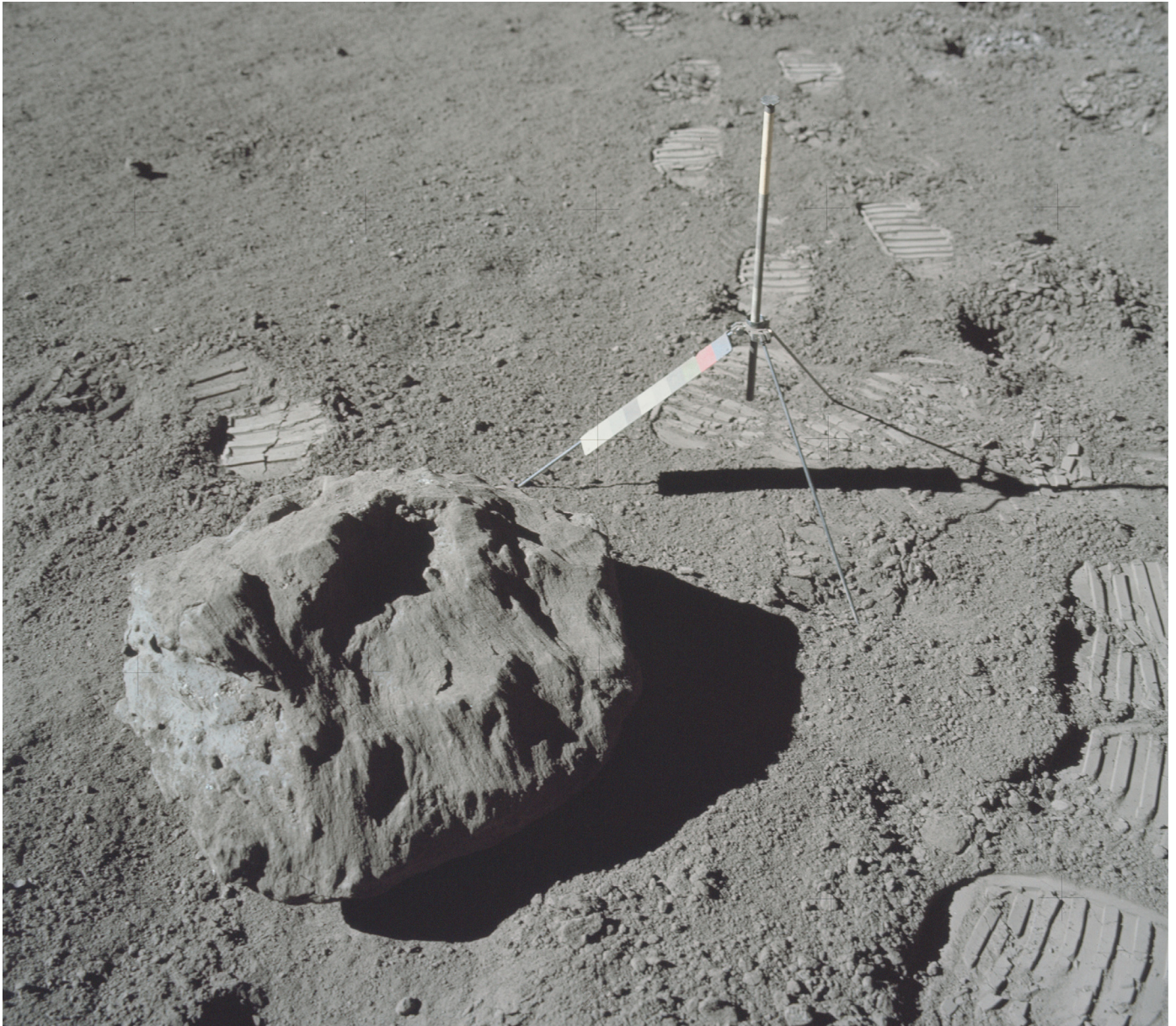
Fig. 14. Station 8 norite boulder in its original position on the slope of the Sculptured Hills. Note the striated glass coating that covers most of the boulder's surface. Gnomon vertical rod is 40 cm long. NASA Photograph AS17-146-22369.

dated at about 3.72 Ga (Table 2) as the average of 33 isotopic ages determined for Apollo 17 basalts (Schmitt, 2014; Meyer, 2008). The latter conclusion on the younger relative age of the valley basalt derives from M^3 data showing the existence of apparent Sculptured Hills-related materials (Family Mountain, Bear Mountain, and others) projecting above the basaltic valley fill (kipukas) (compare Figs. 1 and 12).

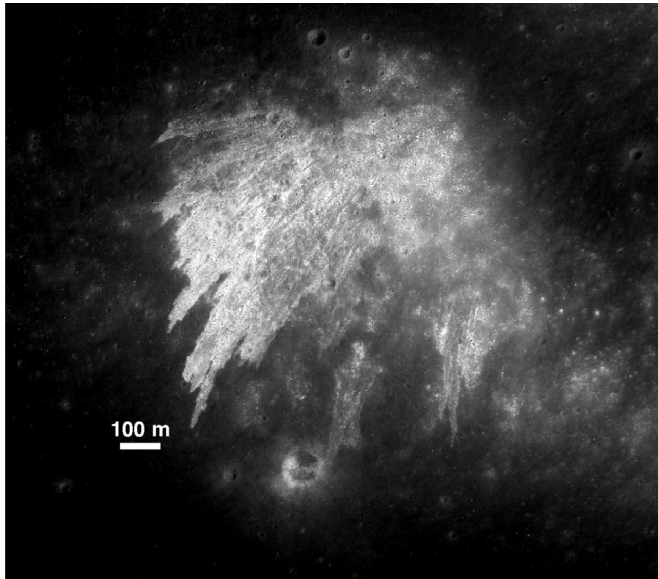## 4. Source and orientation of rim boulders at Camelot Crater

4.1. Source and exposure age of Camelot rim boulders

Apollo 17 astronauts reported on and photographed (Schmitt and Cernan, 1972, GET 141:42:45 – 141:44:28, GET 141:42:45 – 146:28:31–146:50:03) the ejecta blanket, rim and interior of Camelot Crater at Station 5 (color and black and white panoramas AS17-133-20339-61 and AS17-145-22159-83). These photographs and LROC images of Camelot Crater (Fig. 1) provide details on

the distribution of block concentrations in the crater and on its rim. Concentrations of blocks on the rim of Camelot appear to be surface extensions of groups of block concentrations on the crater interior wall. Plumes of dark mantle material extend down the wall, separating various block fields from each other. These darker plumes narrow with depth as they become increasingly confined by the crater's bowl.

Although Camelot is now only about 80 m deep (Fig. 16), with an original diameter of ∼600 m, the formative impact probably exposed subfloor basalt to a depth of 120 m or more, based on Pike's (1974) conclusion that original depth/diameter ratios are about 0.2. Croft (1980) further suggests that excavation of target material reaches to about one-half the original depth, or ∼60 m in the case of Camelot. Based on LROC images of comparably sized young craters elsewhere in Mare Serenitatis basalts (Fig. 17), the initial impact that formed Camelot would eject concentrations of large boulders significantly beyond the initial crater rim, probably out to about one crater diameter. This is not what is observed

Fig. 15. Paint splatter feature on the southeastern peak of the Sculptured Hills, showing granular debris flows of two different apparent ages based on contrasting reflectance. Thin, bright lines within individual flows are levees of boulders. LROC Image M126724656L.

Exposure ages on samples collected from the rim of Camelot (Meyer, C., 2008, samples 75035, 75055 and 75075) suggest that the boulders from which they came reached the surface 40–140 million years ago, with a median exposure age of 105 ± 10 million years. With estimated micro-meteor erosion rates of 0.5–2 mm per million years (Hörz et al., 1973, p 170; Fleischer et al., 1975; Crozaz et al., 1974, p. 2492), this median exposure age does not allow for more than about 5–20 cm of post-impact boulder erosion. This is hardly enough erosion to eliminate all large boulders on the ejecta blanket.

A possible solution to this puzzle about Camelot boulder distribution may be that the crater formed much earlier than suggested by the cited exposure ages. Down slope movement of continuously forming wall regolith would steadily expose additional large blocks along the rim crest and in the crater wall while blocks on the ejecta blanket were being ground into regolith. This is analogous to a similar process thought to be exposing fractured bedrock and boulders at the edge of Hadley Rille (Swann et al., 1972; Apollo Lunar Geological Investigation Team, 1972). The relatively young exposure ages of the rim blocks actually may represent the length of time since their exposure by down-slope movement of crater rim and wall regolith rather than recording the time since an ejection from Camelot.

If Camelot Crater formed significantly earlier than suggested by exposure age determinations for Station 5 samples, it is likely that the blocks at the current rim of Camelot consist of former wall rocks rather than rim ejecta. Instead of having been excavated from the initial transient crater, these wall rocks may constitute either roughly in situ bedrock, possibly tilted upwards, or part of the overturned flap of higher portions of the subfloor. Highly rounded topographic profiles across the crater (Fig. 16) suggest that any overturned flap may have disappeared through impact erosion if, indeed, such a flap forms at all in block-fractured basalt. A detailed analysis of vesicle orientations and shape using the Station 5 samples and photographs might show if the sampled boulders were overturned or not as well as confirming their original horizontal orientation.

The possibility that the Station 5 samples come from a relatively shallow portion of the subfloor could be investigated further by detailed analysis of the contrasting physiography and crater count ages of Camelot-class impact craters and their ejecta blankets. LROC images and LOLA topographic profiles now provide data for such an analysis. The question is at what rate are the rims of such craters eroded down and back with a subsequent increase in the diameter and decrease in depth of a given crater? It may be

at Camelot, creating the physiographic puzzle that rim block concentrations do not extend outward onto Camelot's surrounding ejecta blanket (Fig. 18).
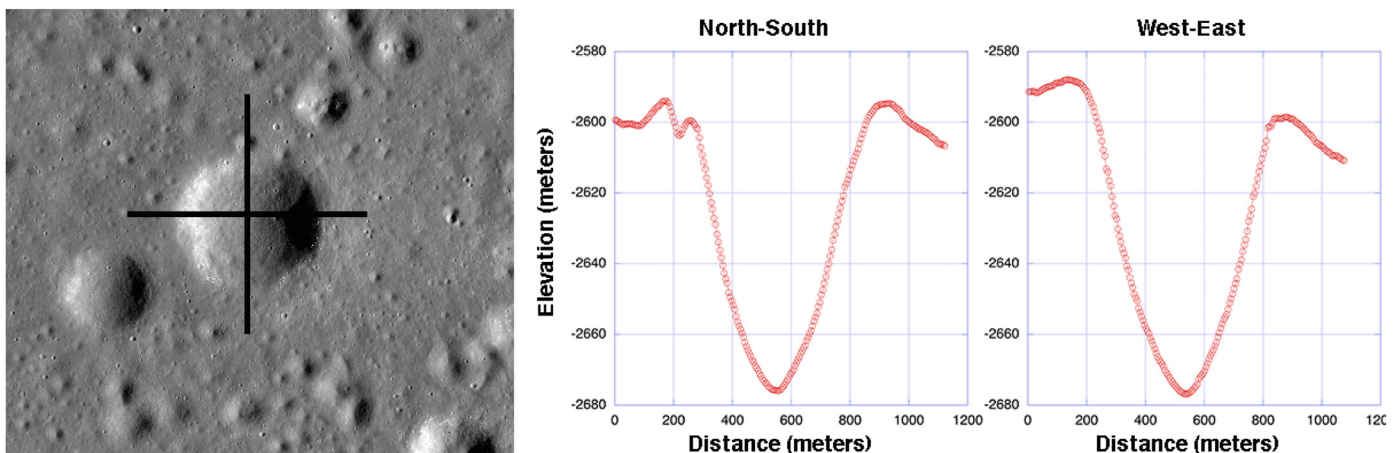
Observations and photographs obtained during a Lunar Roving Vehicle (LRV) traverse across Camelot's ejecta blanket revealed very few exposed blocks greater than half a meter in size. Along a line just outside the rim crest, the surface area concentration of blocks greater than 10 cm in size drops off markedly from about 50% along the crater rim to less than 1% (Schmitt and Cernan, 1972, EVA-2 GET 141:42:45 – 141:44:28). On this gently sloping ejecta blanket, new regolith accumulates largely in place. A high resolution LROC image (Fig. 19) of numerous relatively young, blockless impact craters on the ejecta blanket confirms that relatively few blocks remain intact and unincorporated into regolith as also reported by Schmitt (Schmitt and Cernan, 1972, GET 141:46:11 – 141:47:02). Similarly, a Mini-RF S1 image (Fig. 11) indicates a low abundance of decimeter-sized blocks remaining at and near the surface of Camelot's ejecta blanket.

Fig. 16. Topographic profiles through Camelot Crater (Fig. 1). At left is a LROC NAC image of Camelot (~600 m diameter) with North-South and East-West profiles marked. At right are NAC DTM (Fig. 2) derived topographic profiles showing the present depth of the crater is ~80 m.
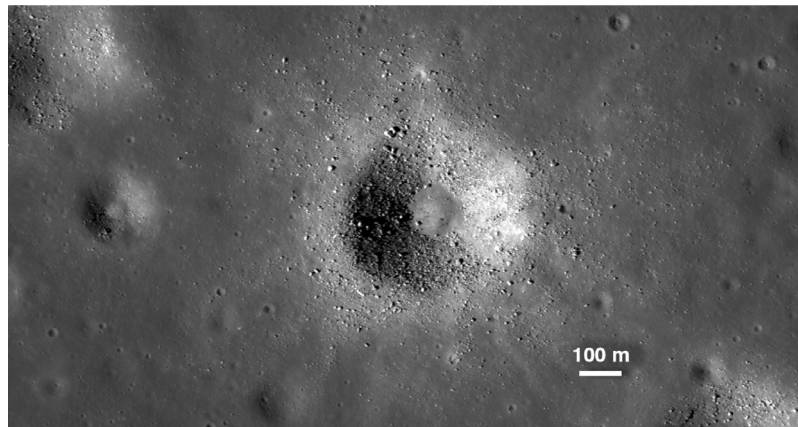
Fig. 17. A fresh ~600 m diameter impact crater in mare basalt with numerous boulders in and on its ejecta blanket and on the crater wall. The largest blocks are ~20 m in diameter. The relatively young age of this crater, as compared to Camelot Crater in Taurus–Littrow, is shown by its bright ray pattern as well as by the abundant boulders away from the crater rim. Crater is located in Mare Serenitatis at 23.20°N, 25.15°E, approximately 220 km to the northwest of the Taurus–Littrow Valley. LROC Image M104354575L.

that the ratio between crater diameter and rim height relative to the crater floor shows relative age better than rock exposure ages, as proposed through topographic diffusion analysis by Fassett and Thomson (2014). In fact, working with topographic profiles across Camelot like the one illustrated in Fig. 16, the approach described by Fassett and Thomson (2014) estimates the age of Camelot to be about 500 ± 150–200 Myr, consistent with the considerations given above.

4.2. Possible determination of ancient lunar magnetic field orientation

Remanent magnetization in Apollo samples and regional magnetic anomalies indicate that the Moon had an ancient global lunar magnetic field (Weiss and Tikoo, 2014). The orientation and history of that field, however, has not been determined due to the absence of dated samples that can be oriented absolutely in three-dimensions relative to the time at which they cooled through their Curie point. Consideration of Apollo 17 sample documentation in the context of LROC images provide new insights into orienting samples of basaltic lava bedrock sampled at the rim of Camelot Crater.

As a consequence of the above hypothesis that the samples we obtained at Camelot Crater (especially, 75035, 75055 and 75075) likely constitute crater wall rocks rather than randomly oriented ejecta, there exists an opportunity for possible measurements of remanent magnetic field orientations for the upper portion of the subfloor basalt. The Station 5 rim boulders can be assumed to have cooled initially in a roughly horizontal position. The flat tops and the flow structures of the large boulders from which samples were obtained give a close approximation of their original horizontal positions. Whether overturned or not, any remanent magnetization in the samples would provide a constraint on the inclination of the lunar magnetic field orientation about 3.7 billion years ago, the approximate cooling age of upper portions of Taurus–Littrow mare basalt (Table 2).

All three of the Station 5 samples noted above have had orientations relative to their host boulders determined by the Lunar Field Geological Team (Wolfe et al., 1981, p. 113–120.). Using the image of the gnomon and its shadow in the documentation photographs and the above geological interpretation, these orientations can be refined by more detailed stereographic analyses (see Section 7, for example). In particular, measurements on the samples can be rotated into their two possible original horizontal and azimuthal positions relative to pre-impact locations. Whether

overturned or not, the remanent field determinations can be compared for consistency with each other.

5. Light mantle avalanche geology

5.1. Light mantle geology and age

The primary geological targets for the exploration of Taurus–Littrow included a plume-like unit of high albedo material superposed on the valley floor, extending northeastward from the South Massif (Fig 20). Pre-mission photographs of Taurus–Littrow show fair detail of this "light mantle" deposit overlying the valley floor. Fingers of the unit extend as much as 5 km from the base of the 28° slope of the ~2.2 km high South Massif. This unit has an area of ~20 km^2 with an estimated volume of at least 0.06 km^3, based on apparent depths of post-deposition impact craters.

Exposure ages of regolith fragments from Station 2 and 3 are assumed to potentially represent the age of the light mantle emplacement event (see Table 3). Rake sample 72539 at Station 2, from regolith created after this event, has an exposure age of 107 ± 4 million years (Meyer, 2008, sample 72539). Exposure ages of samples of Station 2 boulders are less than this amount by at least 50% (Table 3) and presumably rolled to their present positions well after the light mantle was emplaced. Several rock samples from a small crater rim at Station 3 on the light mantle near Lara Crater (Figs. 2 and 21) have exposure ages ranging from ~243 to ~90 million years. The Station 2 exposure age of 107 million years for rake sample fragments from the present slope of the South Massif may provide a maximum age of deposition as some of the Station 3 samples probably were exposed on the South Massif prior to their incorporation into the light mantle. Some samples from Station 3 on the light mantle support a light mantle age of between 70 and 110 Ma, specifically, the exposure ages of 71–97 (ave. 90) million years for sample 73255 and of 110–195 million years for sample 73235 (note that 73235 may have experienced pre-avalanche exposure on the South Massif and the 195 Ma date may reflect that, Table 3). A bracketing of ages between 70 and 110 Ma also would include the possible 75–86 million years discussed in Section 6.2 as the reported crater frequency and topographic diffusion analyses for the Lee-Lincoln fault.

In preparation for the geological exploration of the light mantle unit, the senior author speculated that this feature might have been the result of a fluidized avalanche of South Massif regolith. The perpendicular orientation of the unit relative to the northeast-facing slope of the South Massif and its feathery distal

Fig. 18. Edge of Camelot Crater's rim boulder field, showing a sharp contact against the regolith developed on the surrounding ejecta blanket. The senior author provides relative scale of near-field boulders. NASA Photograph AS17-145-22165.

Table 3
Reported exposure ages of samples possibly related to the age of the light mantle avalanche. Note: Cosmic ray exposure ages compiled by Meyer (2008) and Wolfe et al. (1981) are minimum ages due to micrometer impact erosion of boulders and fragments. Station 2 is on slope of the South Massif, Station 3 is on the light mantle deposit, and Station 4 is on the rim of Shorty, a post-avalanche impact crater (Fig. 2).

Sample	Description	Technique and exposure age	Comments
72315	Boulder 2 sample	Cosmic Ray and micro-meteor counts Kr 0.1 Myr	Exposure after spallation of older rock surface
73131	Regolith breccia from 2 m crater on light mantle	^{22}Na^{26}Al 0.1–0.6 Myr	Exposure age probably result of exposure after a small impact
73221	Range for fragment from rim of crater in light mantle	^{22}Na^{26}Al 0.6–1.3 Myr	Recent exposure by local impact
73241	Range for single fragment	^{22}Na^{26}Al 0–2 Myr	Recent exposure by local impact
73261	Station 3 fragment	^{22}Na^{26}Al < 2.6 Myr	Recent exposure by local impact
74220	Pyroclastic ash	Tracks 9–14 Myr	Post-avalanche exposure by Shorty impact
74255	Station 4 basalt ejecta	Kr 17.3 ± 1.0 Myr	Post-avalanche exposure by Shorty impact
74275	Station 4 basalt ejecta	Kr 32 ± 1 Myr	Post-avalanche exposure by Shorty impact
72395	Boulder 2	Kr 27 Myr	Post-avalanche exposure on slope of South Massif
72255	Boulder 1 sample	Cosmic Ray 40 Myr	Post-avalanche exposure on slope of South Massif
72275	Boulder 1 sample	Kr 52.5 ± 1.4 Myr	Post-avalanche exposure on slope of South Massif
73255	Station 3 rock fragments	Ar 71–97 (Ave. 90) Myr	Possible pre- avalanche exposure on slope of South Massif
72535	Station 2 rake sample fragments	Kr 107 ± 4 Myr	Post-avalanche exposure on slope of South Massif
73235	Station 3 rock fragment	Ar 110 Myr	Possible pre- avalanche exposure on slope of South Massif
73275	Station 3 rock fragment	Kr 139 Myr	Possible pre- avalanche exposure on slope of South Massif
73255	Station 3 rock fragments	Kr 149 Myr	Possible pre- avalanche exposure on slope of South Massif
73275	Station 3 rock fragment	Ar 160 Myr	Possible pre- avalanche exposure on slope of South Massif
73235	Station 3 rock fragment	Ar 195 ± 20 Myr	Possible pre- avalanche exposure on slope of South Massif
73215	Range of 11 fragments	Ar 228–268 Myr	Possible pre- avalanche exposure on slope of South Massif
73215	1 fragment	Kr 243 Myr	Possible pre- avalanche exposure on slope of South Massif
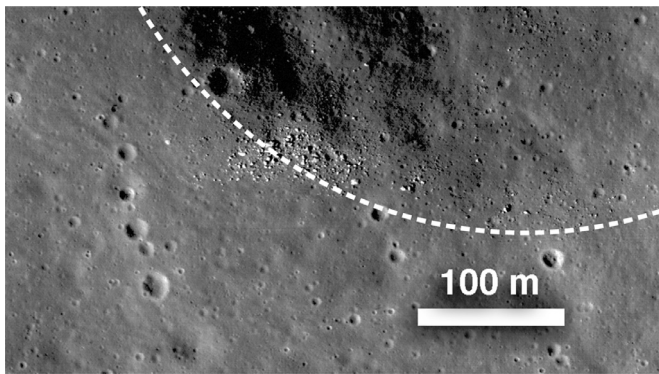
Fig. 19. Decameter-scale diameter impact craters on the southwest, near rim ejecta blanket of Camelot Crater. In contrast to the abundant large boulders at the crater rim, the lack of large blocks in and around these relatively young impact craters indicates that few boulders remain within the ejecta blanket's regolith. The dashed line shows the approximate rim crest for Camelot Crater. LROC Image M168000580LR.
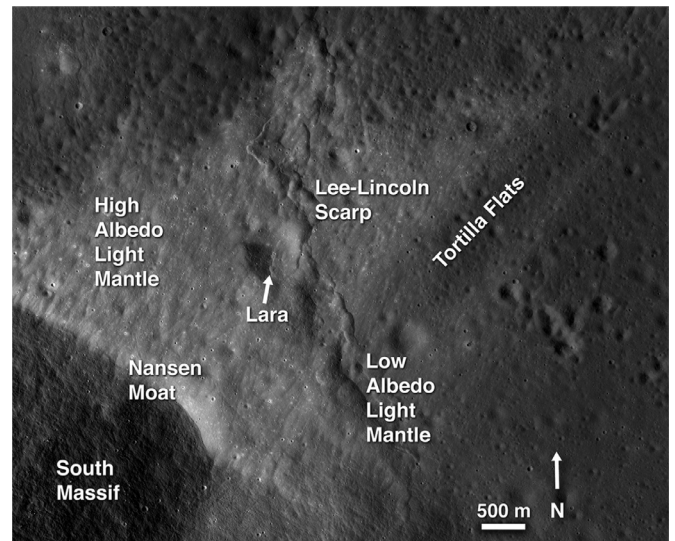

Fig. 21. Overhead view of the detailed features of the light mantle avalanche deposits and the Lee-Lincoln Scarp. LROC Image M104311715LR.

ends suggested such an origin. Prior to the Apollo 17 mission, this possibility was discussed with UCLA Professor of Geophysics Ronald Shreve, an early researcher on fluidization of rock debris avalanches (Schreve, 1968; Mitchell et al., 2015). After some discussion, it was concluded that, in order for the material of the light mantle to travel up to 5 km, gases from some source probably fluidized an avalanche of regolith previously developed on the slope of the South Massif.

Release of solar wind volatiles by agitation (Carrier et al., 1973) in the moving avalanche constitutes a possible fluidization mechanism in a one-sixth Earth's gravity environment. Acoustic fluidization also has been proposed as a means to produce long-runout debris flows (Melosh, 1979; Collins and Melosh, 2003). This second possibility may be a response to pressure variations at high frequency, generated by initial collapse and subsequent flow of debris. An alternative "pseudofluidized condition" has been proposed (Scott, 1987), involving the dynamic motion of

regolith particles at the base of the avalanche. Although acoustic fluidization and pseudofluidized conditions may contribute to lunar avalanche dynamics, the presence of significant amounts of solar wind volatiles in lunar regolith suggest that gas fluidization is the primary contributor. Analysis of regolith samples from Apollo missions indicated that solar wind hydrogen, nitrogen, carbon and helium exist in samples of these materials at levels of at least 100 ppm each (Heiken et al., 1991, p. 444 and 438). In situ concentrations probably are higher than this amount by about a factor of two due to agitation losses between sample collection and laboratory measurement (Schmitt, 2006, p. 89–92.).

The L/H net efficiency (Iverson, 1997, p. 248) of a hypothetically dry light mantle avalanche is about 2.3 (5.0 km maximum length-L /2.2 km maximum height-H). This is about a factor of
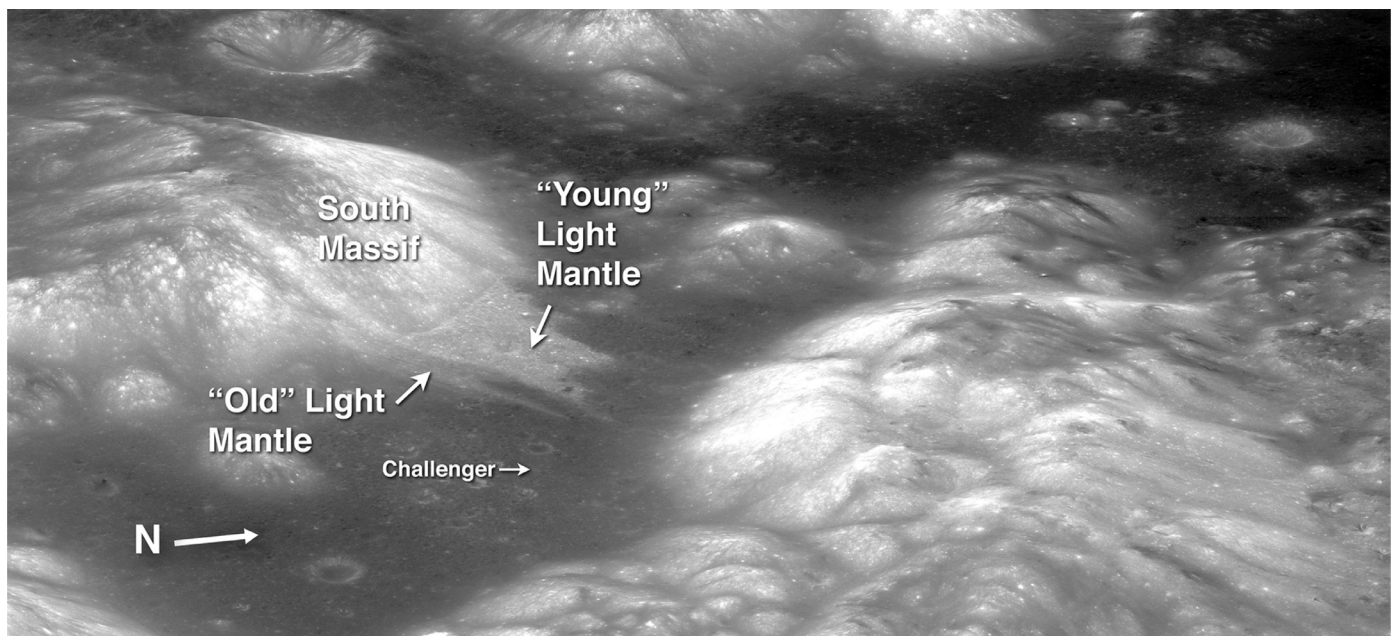
Fig. 20. East to west, high sun-angle view of Taurus–Littrow showing the plume-like avalanche deposit (center left) at the base of the South Massif. The image reveals a low albedo, and presumably older, light mantle unit apparently underlying the dominant high albedo, and apparently younger light mantle unit. LROC Image M1182232465.

Table 4

Comparison of selected components of samples from low and high albedo subunits of light mantle. Agglutinate, Impact Breccia, Orange+Black Ash, and Basalt contents are from Heiken and McKay (1974) and Maturity Indexes from Morris (1978). **Bold** indicates sample from the low albedo light mantle. 72141 from LRV-2 specifically sampled the low albedo unit; however, LRV-6, where 74121 was obtained, is located within the apparent high albedo light mantle unit (Wolfe et al., 1981, p. 94–95). The data for 74121 suggest that the impact at that location may have penetrated through the high albedo light mantle into the underlying low albedo light mantle.

Light mantle sample	Agglutinate	Maturity index	Impact breccia	Orange+Black ash	Basalt
72141 LRV-2	**50.6**	**81**	**9.6**	**6.3**	**7.2**
73121 Sta. 2A	41.7	48	32.0	2.4	0
73221 Sta. 3 Trench Skim 4 cm	26.3	43	46.6	2.6	3.0
73241 Sta. 3 Trench 5 cm light	8.4	18	61.5	6.0	1.0
73261 Sta. 3 Trench 10 cm dark	34.3	45	39.1	2.3	2.0
73281 Sta. 3 Trench 10 cm light	24.6	34	46.6	1.6	3.7
74111 LRV-5		31			
74121 LRV-6	**51.7**	**88**	**24.7**	**2.6**	**2.0**

10 less than comparable volumes of water-rich, poorly sorted terrestrial pyroclastic debris flows (Iverson, 1997, p. 249). This comparison suggests that the physics of volatile fluidization of the light mantle avalanche was not comparable to water fluidization of terrestrial debris flows of similar masses, possibly due to a rapid loss of volatiles to vacuum or to more transient acoustical or pseudofluidization processes noted above. The highly irregular surfaces of most of the particles within the avalanche also may increase the internal frictional losses of kinetic energy relative to terrestrial pyroclastic flows. A volatile-aided fluidization hypothesis to explain the dynamics of the light mantle avalanche in a one-sixth Earth's gravity environment remains speculative and requires further experimental and theoretical study to confirm.

New orbital images indicate a complex history for the light mantle unit that bears on the potential causes of the avalanche. A westward viewing, high Sun-angle LROC image (Fig. 20) reveals two distinct areas of the light mantle, one with lower reflectance (southeast of Lara Crater) than the other. Low radar reflectance in a Mini-RF total power image (Fig. 11), corresponding to the area of lower optical reflectance, indicates a lower decimeter block concentration at and near the surface of the southeastern light mantle unit. The lower reflectance and decimeter block concentration probably is due to longer exposure to space weathering, implying that this southeastern light mantle unit is significantly older than the northwestern unit.

Reflectance measurements on the two units give radiance factors (I/F) (Minnaert, 1961) of 0.076 for the older avalanche and 0.091 for the younger (LROC NAC M124369214LR). (Similar relative I/F differences exist between apparently older and younger granular debris flows in the paint splatter-like feature of the Sculptured Hills that have I/Fs of 0.082 vs. 0.11–0.12, respectively.) While it is possible that the two light-mantle units have differences in composition, differences that might cause the two flows to appear distinct in the image data, no remote compositional or sample data for either the units or their sources support that possibility (Fig. 12). Indeed, as they both consist of regolith from the same limited area of the South Massif, no significant compositional differences are expected.

Table 4 shows the agglutinate, maturity indexes (Is/FeO), and other data for Apollo 17 samples (Meyer, 2008, samples 72141, 73121, 73221, 73241, 73261, 73281, 74111, and 74121; Morris, 1978) obtained from the surfaces of the two albedo units of light mantle. The higher agglutinate content (50.6 vol. %) and maturity index (81) of sample 72141 from the low albedo light mantle unit sampled at Station LRV-2 are consistent with it being a significantly older deposit. Also, Table 4 shows that the two samples from the low albedo unit contain distinctly less total breccia fragments, possibly indicating either differences in their source areas or a loss of breccia fragments due to a longer period of impact comminution. The higher content of orange+black ash (6.3 vol. %) in

the low albedo unit also is consistent with longer duration exposure to lateral impact mixing with nearby dark mantle material (10–15 vol. % ash). Impact craters several meters in diameter in this older unit have not penetrated to the underlying dark mantle, indicating that vertical mixing has not taken place.

Companion samples to 73221 (73241, 73261, and 73281) are listed in Table 4, all of which came from the crater rim trench at Station 3 (Fig. 1). Those samples have agglutinates less than 34.3 vol.%, breccia contents more than 39.1 vol. %, orange-black ash content less than 2.6 vol. % (except for 73241), and maturity indexes (Is/FeO) less than 45 (73261). Sample 73261 with a maturity index (Is/FeO) of 45, however, also has the lowest albedo as viewed in situ (NASA photo AS17-138-21148), suggesting extended surface exposure to micro-meteor impacts. This sample possibly could be from the underlying low albedo light mantle unit, having been protected from further aging by overlying high albedo light mantle. If 73261 represents the older, now lower albedo unit of light mantle, its similarity to the high albedo light mantle in agglutinate, breccia and orange+black ash content and in maturity index suggests the avalanche that deposited it occurred about twice the time before that of the later light mantle avalanche (possible age of 75–107 Ma). This conclusion is consistent with the maturity index of the continuously exposed low albedo unit sample 72141 being nearly double that of the maturity indexes of samples of the high albedo light mantle unit.

The existence of two distinct light mantle avalanches largely rules out that Tycho Crater secondary impacts triggered the younger, high albedo avalanche as proposed by Lucchitta (1977). As discussed in Section 6.4, faulting within the valley constitutes a more likely trigger for both avalanches.

5.2. Characteristics of the youngest light mantle avalanche

The static angle of repose for regolith on the slopes of the South Massif, that is, slightly cohesive, dry regolith exposed to lunar gravity, exceeds that of similar material on Earth, probably reaching angles higher than 40° (see work of Kleinhans et al., 2011). Trenches and boreholes in lunar regolith hold vertical walls, indicating at least a short term angle of repose of 90° due to internal cohesion. The main contributors to that cohesion include van der Waals forces between particles broken in vacuum and highly irregular, interlocking particle shapes (Heiken et al., 1991, p. 285–307; Jiang et al., 2013). On the other hand, the dynamic angle of repose of such regolith would be significantly lower than on Earth (Kleinhans et al., 2011), the degree of difference depending on both the amount of dilation in reduced gravity and of fluidization during motion, other factors being equal.

The regolith on the steep northeast slope of the 2200 m high South Massif (as well as the North Massif) currently rests stably at

~28° as measured from the NAC Digital Terrain Model (Henriksen et al., 2017). This angle is not a true static angle of repose as it represents a dynamic equilibrium, established over ~3.8 billion years since the Massifs were formed, between the aggregate and gradually changing geotechnical properties of the slope's regolith and the continued impacts of micro- and macro-meteors. Once disturbed and fluidized by agitation-released volatiles, however, the dynamic angle of repose clearly became much lower than 28°. The very low slope of the light mantle avalanche deposits indicates that the dynamic angle of repose for such a large mass is less than a few degrees.

After exploration in Taurus–Littrow, and now with access to new orbital datasets, the characteristics of the youngest light mantle unit can be defined in more detail and are listed below. We conclude that the combined evidence, directly and indirectly, supports a fluidized avalanche hypothesis for the origin of the young light mantle.

- LROC images of 15 m and 30–50 m diameter impact craters that do not expose dark mantle in the approximately 5 × 4 km mapped light mantle unit indicate it is at least 3 m thick in the northwestern portion and at least 6–10 m thick in the southeastern portion, based on a 0.2 depth to diameter ratio for the craters (Pike, 1974). This potentially greater thickness in the southeast may be due to superposition of the high albedo unit on the low albedo unit. One ~ 80 m diameter impact crater in light mantle about 1 km northwest of the rim of Nansen crater and just outside the trough at the base of the South Massif excavated into dark mantle material, indicating a light mantle thickness there of less than 16 m.
- An estimate that the 5 × 4 km, > 3 m thick younger light mantle deposit contains at least 0.06 km³ (6 × 10^7 m³) of material. Although LROC and LOLA derived topography, and some near-terminator images, hint at a depression in the northeast slope of the South Massif, no specific scar is clearly visible.
- Field observations (Schmitt and Cernan, 1972, EVA-2, GET 142:52:53–143:31:25), and post-mission examination of samples from Stations 2 and 3 (Wolfe et al., 1981) show that the light mantle constituents, including fragments within it, are very similar to those of the impact breccia dominated regolith on the slope of the South Massif.
- Field observation (Schmitt and Cernan, 1972, EVA-2, GET 143:37:25–143:39:41) and post-mission comparison of Station 2 rake samples (Wolfe et al., 1981) document that the upper portions of the light mantle deposit consist of fine-grained debris, containing about one-fifth the concentration of coherent rock fragments greater than about 1 cm in diameter relative to those found in the regolith on the slope of the South Massif. This suggests a process of concentration of fine material upwards during the escape of fluidizing volatiles due to low mass to surface area ratios (>50% of mature lunar regolith is less than 100 μm in diameter (Carrier, 1973)). The fine-grained, upper portion of the deposit, below ~5 cm of new regolith, appears indurated at depth, giving significantly brighter 12.6 cm Mini-RF S1 radar returns (Fig. 11) than the surrounding dark mantle. Induration below about 5 cm also was observed in the field in the walls of small impact craters and during rake sample collection and suggests compaction by settling during the late stages of fluid (gas) escape upwards (see Shreve, 1968; Valverde and Castellanos, 2006). As Mini-RF S1 returns are sensitive to 1–1.5 m depth (Raney, R. K., 2007; Nozette et al., 2010; Raney et al., 2011), induration may extend to deeper levels; however, the possibility also exists that decimeter-sized fragments increase in concentration with depth.
- Examination of LROC images as well as photographs taken during the Apollo 17 EVA-2 LRV traverses across the light mantle shows that boulders exposed by impacts into the light mantle are concentrated in the walls of craters rather than on the light mantle surface, strongly suggesting that sorting by fragment size occurred in a fluidized medium (larger fragments lie towards the base of the light mantle). Similar size sorting is observed in some terrestrial pyroclastic flows (Valentine, 1987). Other visible light mantle boulders are either scattered as isolated large individuals between craters or concentrated on the walls and ejecta blanket of the partially buried 600 m diameter impact crater, Lara. (These concentrations of large boulders in and around Lara Crater indicate a young age for Lara relative to other comparable sized craters in the valley such as Camelot.)
- Post-mission examination of samples of the fine-grained upper portion of the youngest light mantle deposit shows it to be rich in agglutinates (>40%) and poor in dark mantle components (<5%) consistent with the existing regolith at Station 2 on the slope of the South Massif.
- LROC images (Fig. 21) show that parallel, ridge and swale longitudinal lineations on the surface of the light mantle extend perpendicular to the base of the South Massif, with the same bearing as its distal plumes. These lineations exhibit a crest-to-crest wavelength of 100–200 m and appear to record the laminar flow dynamics of the avalanche. The LROC images also highlight a lineation pattern of much shorter wavelength (20–50 m) on the southwest-facing slope of the Nansen moat at the base of the South Massif. Finally, a few shallow, graben-like depressions cross the lineations at an oblique angle within a kilometer or so of the base of the Massif. The graben may have developed by extensional stress late in the flow and settling history of the avalanche. Watters et al. (2010, p. 937) attribute these features to stresses imposed by the Lee-Lincoln fault (Section 6); however, graben form under extensional stress rather than the continuous compressive stress associated with thrust faulting.
- A comparison of the volatile contents of South Massif slope regolith (72501) and light mantle regolith (72701) show only minor differences except for a significant depletion of sulfur in the light mantle. South Massif regolith contains ~1100 ppm of sulfur vs. 617 ppm in the light mantle (Petrowski et al., 1974, p. 1943.). North Massif regolith has roughly the same relatively high sulfur content as that on the South Massif. Solar wind hydrogen, nitrogen, helium and carbon, however, appear to have reached current saturation levels in all three of these near surface samples. Sulfur depletion in near-surface portions of the light mantle might result from the settling of small, dense grains containing troilite in the fluidized avalanche. It does not appear that final conversion of kinetic energy to thermal energy (Iverson, 1997, p.248) would raise the avalanche temperature to the levels required to decompose troilite (Kissin, 1982), but this possibility might be studied further.

6. Lee-Lincoln thrust faults

6.1. Lee-Lincoln fault structural geology

Close inspection of orbital photographs taken by Apollo 17 Command Module Pilot R. E. Evans, stimulated by the much higher resolution images from LROC and data from Mini-RF radar, have improved our understanding of the Lee-Lincoln Scarp that crosses the valley of Taurus–Littrow (Watters et al., 2010, p. 936–938). The physiographic appearance of the Scarp (Figs. 1 and 21) clearly is consistent with its being the surface expression of a thrust fault that post-dated both the formation of the valley and its partial filling by basalt (Schmitt, 1973; Wolfe et al., 1981, p. 217). Many other relatively young scarps and wrinkle ridges on the Moon have formed, and may still be forming, as surface expressions of thrust faults, resulting from the gradual thermal contraction of the

Moon and the possible effects of tidal interaction with the Earth (Watters et al., 2010).

As the northwest-southeast surface trend of the Scarp parallels contours across the lower reaches of the North Massif, the strike of the fault plane there is about N60W. Its dip, of necessity, is greater than the corresponding 23° slope of the Massif it crosses, as measured from the NAC Digital Terrain Model (Henriksen et al., 2017). In contrast, the fault plane's strike is about N00W as it crosses the relatively level valley floor. A bend in the strike of about 60° takes place near Hanover Crater over a distance of about 2 km and across the contact between the North Massif and the subfloor basalt.

The dip of the Lee-Lincoln fault plane across the valley probably roughly matches the dip where it crosses the slope of the North Massif. A very approximate calculation of the tangent of this dip can be obtained by dividing the change in LROC/LOLA derived elevation across the Scarp, that is, ~50 m, by the distance over which that change takes place, that is, 500–1000 m. This gives a dip of between 6° and 26° degrees, consistent with the minimum dip of 23° where the fault crosses the slope of the North Massif.

The low dip angle of the Lee-Lincoln fault as it crosses the valley may explain the existence of a number of apparent lobes in its surface exposure (Fig. 21). As faulting occurred, sections of the unsupported hanging wall, including several meters of regolith as well as underlying subfloor basalt, probably broke off and settled to the surface, creating the appearance of separate, horsetail-like breaks in the fault plane.

High-resolution LROC images and crater frequency measurements (van der Bogert et al., 2012) indicate that the number and sharpness of small craters in the regolith on either side of the Lee-Lincoln Scarp are less than for surrounding dark mantle surfaces, giving rise to "shaken-not-stirred terrain" (Schmitt and Robinson, 2010). This change is interpreted to be the result of seismic shaking in the vicinity of the fault.

6.2. Age of Lee-Lincoln scarp

Increasingly, it appears that the thrust fault that formed the Lee-Lincoln Scarp occurred as one or more sharp, near surface moonquakes. Where the scarp crosses the lower slope of the North Massif (Fig. 22), the smoother, shaken-not-stirred appearance of the hanging wall surface is far more pronounced than on the surface of the footwall. The massif would have been far more stable and resistant to seismic shaking than the thin, hanging wall of the Scarp overriding it.

As there appear to be two light mantle deposits significantly separated in time, the exposure age bracket of 70–110 million years for the light mantle avalanche (see Section 5.1) likely does not date the Tycho impact event. This exposure age, however, commonly is used as a proxy for the age of Tycho as part of the calibration of crater size-frequency distribution (CSFD) measurements relative to absolute time (e.g., Hiesinger et al., 2012). Ages derived from CSFD measurements thus may be systematically biased if the true age of the Tycho impact is significantly different from that of the light mantle avalanche. CSFDs for the surfaces in the vicinity of the high-albedo light mantle deposit at Taurus–Littrow may be comparable to CSFDs in the vicinity of Tycho (e.g., van der Bogert et al., 2012; Hiesinger et al., 2012), but uncertainties as to the true age of Tycho suggest the need for additional work in the future. For this paper, we proceed under the traditional assumption that the present CSFD age calibration is correct. Relative differences in CFSDs would remain the same if this assumption proves unwarranted in the future.

In particular, the CSFD measurements of van der Bogert et al. (2012) can be used to address the question of the age of the Lee-Lincoln fault. The model ages they report appear consistent with the photogeological delineations of shaken-not-stirred terrain,
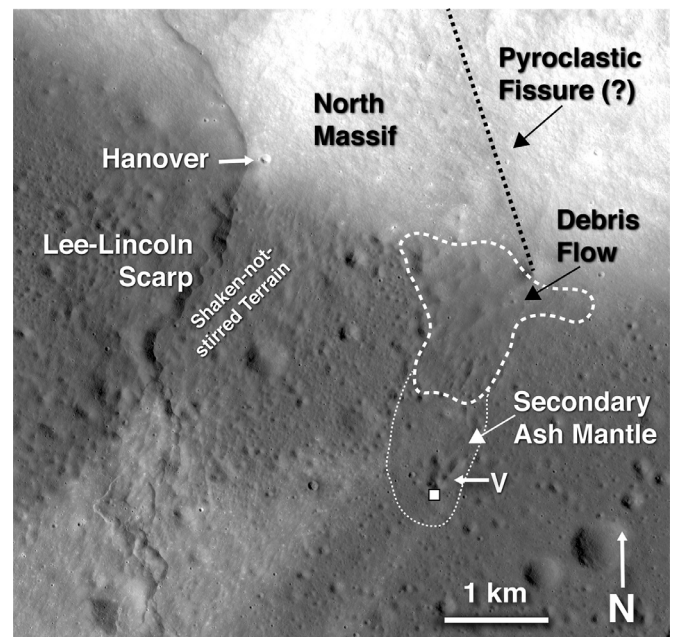

Fig. 22. View of Lee-Lincoln Scarp near the base of the North Massif showing the smooth surface of its hanging wall versus its rougher footwall. Image covers 10 km, left to right. Also shown are the trace of the line of reduced radar reflections (Fig. 11) on the south face of the North Massif that delineates a probable pyroclastic fissure (black dotted line), the outline of a probable debris flow deposit (white dotted line), and a secondary ash mantle (thin dotted line). The secondary ash mantle was sampled at LRV sample stop 7 (white square), where the sample (75115) contained 16% orange glass and black ash. Note the inverted cone-shaped, rimless subsidence crater at the valley (south) end of the fissure line. "V" indicates the location of Victory Crater. LROC Image M104311715LR.

showing about 75–91 Ma for shaken-not-stirred terrain versus about 105 Ma for terrain outside that designation and further from the scarp (Fig. 23). Fassett and Thomson (2015) find that a topographic diffusion model of impact erosion supports a 75 Ma maximum age for the scarp. Work continues, however, on the application of this model to the Lee-Lincoln Scarp (Fasset, 2016, personal communication).

The crater count age of 105 Ma for an area outside of the shaken-not-stirred terrain, however, is still much less than would be expected for the valley surface as a whole, as its regolith began to form on the subfloor basalt surface about 3.7 billion years ago. Possible explanations for this apparent crater count discrepancy may be (1) the maximum size of craters used in the van der Bogert study represents the saturation crater size, (2) repeated shaking of the valley floor by faulting has accelerated crater aging (Schmitt and Robinson, 2010), and (3) crater size has been depressed by 15–20% or more due to very fine grained ash in the regolith (Lucchitta and Sanchez, 1975). Regional analysis of CSFDs (van der Bogert et al., 2016) that include larger craters has recently indicated that the age of comparable surfaces in the region are roughly consistent with the apparent 3.5 Ga Pb-Pb isotopic age (Tera and Wasserburg, 1976) of volcanic ash sampled at Shorty Crater (Station 4).

6.3. Formation of the Nansen Moat

There also may be a genetic relationship between the Lee-Lincoln Scarp and the Nansen Moat at the base of the South Massif (Fig. 21). The senior author had begun his post-mission speculation about the origin of the Nansen Moat with the idea that the valley floor and South Massif had separated slowly along the original northeast-sloping normal fault that bounded the southwest side of the valley (Schmitt, 1973). A trend toward
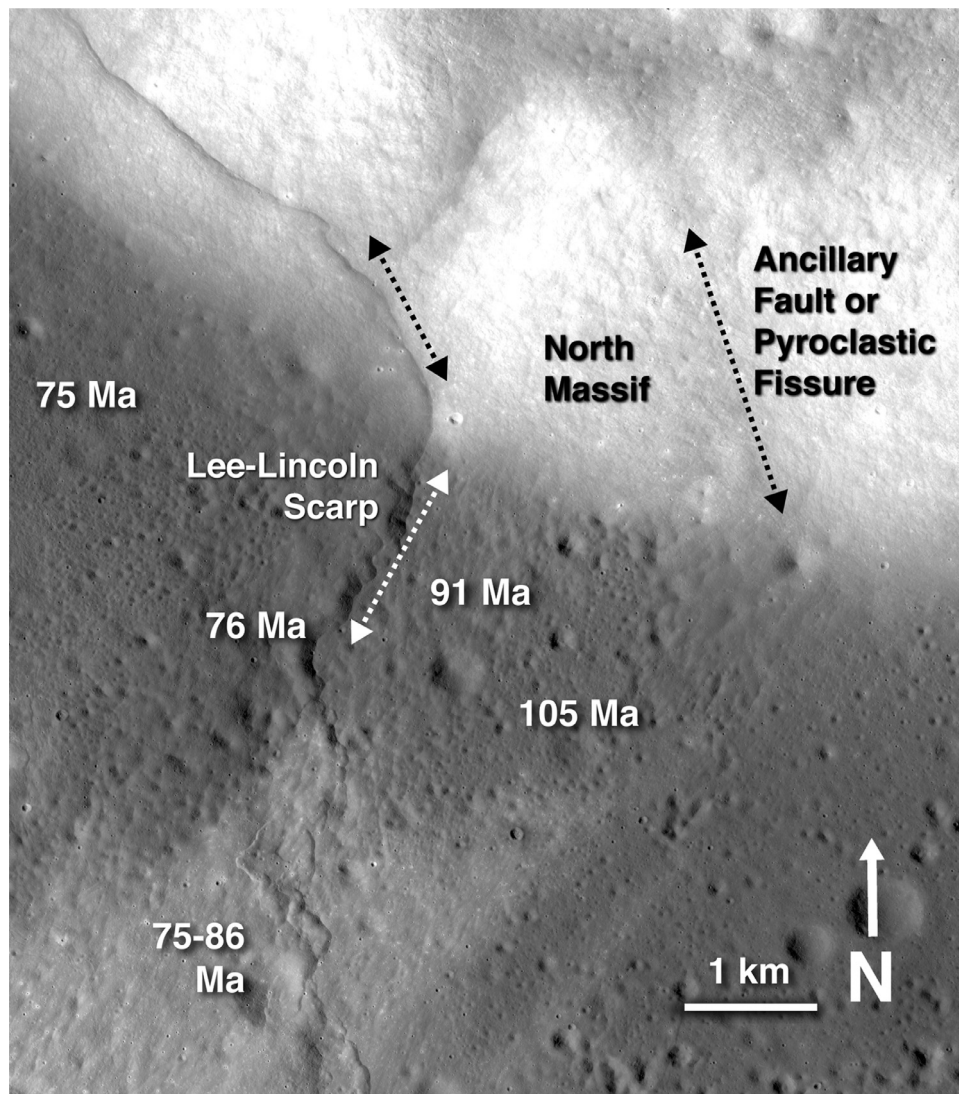
Fig. 23. "Shaken-not-stirred" terrain (Fig. 22) in basaltic regolith around the Lee-Lincoln Scarp. Crater-frequency ages referenced in text are shown by numerals. The line of reduced radar reflectance (Fig. 11) that may define either an ancillary fault or pyroclastic fissure is shown by the right hand, dotted double arrow. At the lower end of that line, a tongue-shaped apparent landslide deposit is visible that also appears to have the "shaken-not-stirred" surface appearance. LROC NAC Image M104311715LR.

isostatic equilibration, resulting in relative subsidence of the mass of the South Massif versus the valley floor, might have been the cause of such gradual separation. In this original hypothesis, the rate of separation would need to open space along the moat faster than the down-slope movement of debris could fill that space.

Reconsideration of the moat's origin and LROC images of the Lee-Lincoln Scarp, however, raise the distinct possibility that the southwest to northeast thrusting expressed by the scarp occurred relatively recently as a single, energetic event. Such a fault could have moved the valley floor away from the more stable South Massif, creating the original Nansen Moat as well as triggering a bottom-up rapid destabilization of the South Massif regolith. Such a rapid initiation of the avalanche may have enhanced the potential for acoustic fluidization to operate along with solar wind volatile fluidization.

In support of the hypothesis that the Lee-Lincoln fault movement opened the Nansen moat and triggered the light mantle avalanche, the CSFD age for the younger, high albedo light mantle (see Fig. 23) approximates that for the hanging wall of the Lee-Lincoln fault (van der Bogert et al., 2012). The ~500 m horizontal width (rim to massif slope) of the Nansen Moat is consistent with the estimated 500–1000 m net horizontal movement of

the Lee-Lincoln fault (Section 6.1). It appears that the dip of the graben fault at the base of the South Massif would be about 60° ±30° to the north northeast (the minimum dip of 30° being the approximate slope of the South Massif lying above Nansen moat).

6.4. Possible pyroclastic fissure or Lee-Lincoln ancillary fault

Mini-RF S-band radar data show a line of reduced reflections that coincide with the trace of the Lee-Lincoln fault scarp along the North Massif and on the valley floor (Fig. 11). It should be noted, however, that topography affects this radar image, brightening southwest-facing slopes and darkening northeast-facing slopes such as those that dominate the fault scarp. On the other hand, the Mini-RF image shows a second line of reduced radar reflections ~3 km to the east of the Lee-Lincoln fault on the south face of the North Massif that is not associated with a northeast-facing slope.

Initially, we considered that the second line of reduced reflections on the North Massif might be along the trace of an ancillary fault related to the Lee-Lincoln fault. Seismic shaking along the immediate line of this possible thrust fault might have caused coarse regolith fragments to move downward in the local regolith due to

Fig. 24. The up-sun locator photo of the ∼3 m diameter crater in the foreground (white ∗) and its location with respect to the *Challenger*, about 119 m distant. The glassy area is the whitish rock patch at bottom center and right of center. Several i.d. markers are also shown for comparison with the LRO photo of Fig. 27. A,B denotes two craters on the other side of the parallel LRV tracks. C denotes a crater in the near field between the distances of A,B. D is a boulder beyond C. The LRV tracks are to the right of A,B. (*Inset*): The direct line-of-sight from the camera is centered on the LMP window in the *Challenger* as indicated by the reseau cross in the enlargement of the black square area given at upper right. (NASA photo AS17-145-22185).

their higher ratio of mass to surface area. The possibility remains that this line of reduced radar reflections indicates a fault line.

Examination of stereo pairs of LROC NAC images, however, shows no definable topographic break along this line. Rather than a fault trace, we hypothesize that the line of reduced reflections is a pyroclastic fissure, now buried by less than a meter of North Massif regolith. This fissure would be similar to those proposed in the Sculptured Hills and discussed in Section 3.2. It is unlikely that the second line of reduced reflections in the radar image constitutes an artifact in the data, but rather the data discloses that there is a significant increase in fine-grained pyroclastics in the regolith formed above the fissure. In fact, a 200 m diameter inverted cone-shaped and rimless crater at the intersection of this possible fissure with the edge of the valley basalt unit may be a post-eruption subsidence feature.

The area on either side of the valley end of this potential pyroclastic fissure appears similar to shaken-not-stirred terrain (Schmitt and Robinson, 2010); however, our recent examination of LROC NAC stereo images suggests that this tongue-shaped area (∼0.7 km²) stands about 30 m above surrounding dark mantle (Fig. 22). The debris flow's lobate distal end consists of a number of smaller lobes while the head area has two wings that suggest some debris moved sideways as it encountered the valley floor at the base of the Massif. The surface physiography of the debris flow consists of distinctive elongate hummocks and swales in the direction of apparent flow. Numerous small irregular depressions characterize the fine scale surface texture. This physiographic appearance is distinct from surrounding dark mantle surfaces that show only the characteristic features of long duration impact cratering.

The head of the debris flow appears to overlie North Massif talus accumulations. This latter fact and the shaken-not-stirred appearance of its surface suggest that the debris flow may have

occurred relatively recently. About 1.5–2.0 km directly ahead of the toe of the debris flow and extending southwest of Victory Crater, the surface appears thinly mantled. This appearance of being "mantled" was also the impression reported by the senior author during a LRV traverse across this area (Schmitt and Cernan, 1972, Second EVA, GET 146:13:56 – 146:14:05).

An LRV sample of regolith (75111) taken at the rim of Victory Crater contains about 16% orange and black pyroclastic ash (Heiken and McKay, 1974). The ∼16% ash content in 75111 is significantly higher than in Heiken and McKay (1974) analyses of basaltic regolith samples from about 1.5 km to the southwest (72150, 9%) and ∼0.7 km and ∼3.0 km to the east (75121, ∼7% and 70181, ∼4%, respectively). In fact, the regolith sample from Station 1 (71061), ∼4.3 km to the southeast, that also has a ∼16% ash content, is the only Apollo 17 regolith sample comparable to 75111. These comparisons support the possibility that a cloud of mixed ash and agitation-released volatiles moved out ahead of the debris flow, depositing a thin, secondary cover of ash. Pyroclastic ash, composed of beads and broken parts of beads, is extremely fine, averaging only about 40 µm in diameter (Meyer, 2008, sample 74002-1).

The farthest-reaching finger of the young light mantle unit (Section 5.2) overlies the toe of the debris flow and the farthest-reaching finger of the old light mantle unit overlies the lightly mantled area southwest of the toe. These relations and the superposition of the debris flow on North Massif talus indicate that the debris flow preceded both avalanches, but possibly not by a long interval. These relations would place the debris flow's age at more than ∼150 Myr.

The debris flow-like deposit at the base of the hypothesized fissure (∼2.3 × 10⁷ m³, assuming a 30 m average thickness) would have an approximate L/H net efficiency (Iverson, 1997, p. 248) of 1, several factors lower than for comparable volume dry debris flows on Earth (Iverson, 1997, p. 249). Based on Iverson's flume experiments, this low L/H efficiency would suggest that the flow material was both well-sorted and fluidized. These results would be consistent with the debris being composed of well-sorted, volatile-rich volcanic ash similar to the ash sampled at Shorty Crater (Schmitt, 1973; Meyer, 2008, sample 74002-1). (See Section 5.2 for comparison with the approximate dynamical analysis of the poorly sorted light mantle avalanche.) Further, most relatively young impact craters on the apparent debris flow have dark ejecta rather than being bright rayed as on surrounding basaltic regolith surfaces, suggesting the flow consists predominately of dark, fine grained material. This latter conclusion is supported by the low radar reflection from the debris flow's surface materials (Fig. 11).

If this pyroclastic fissure and debris flow hypothesis proves true, the flow resulted when ash deposits accumulated on the slope around the proposed fissure and became unstable, possibly when subjected to seismic shock, and moved down to the base of the North Massif. Remaining ash would gradually become incorporated in the downwardly migrating regolith of the North Massif slope. If this fissure eruption roughly coincided with the period of pyroclastic activity represented by the deposits discovered at Shorty Crater (Schmitt, 1973), the eruption occurred about 3.5 billion years ago (Tera and Wasserburg, 1976). As indicated above, the debris flow may be as young as 150 Ma, if penecontemporaneous with the old light mantle unit (Section 5.2).

7. Location and orientation of in situ impact glass sample 70019

7.1. Background

Paleomagneticists have stated that no oriented samples of lunar bedrock were collected from the Moon (Fuller and Cisowski, 1987; Runcorn, 1994). Indeed, no robust paleodirectional measurements
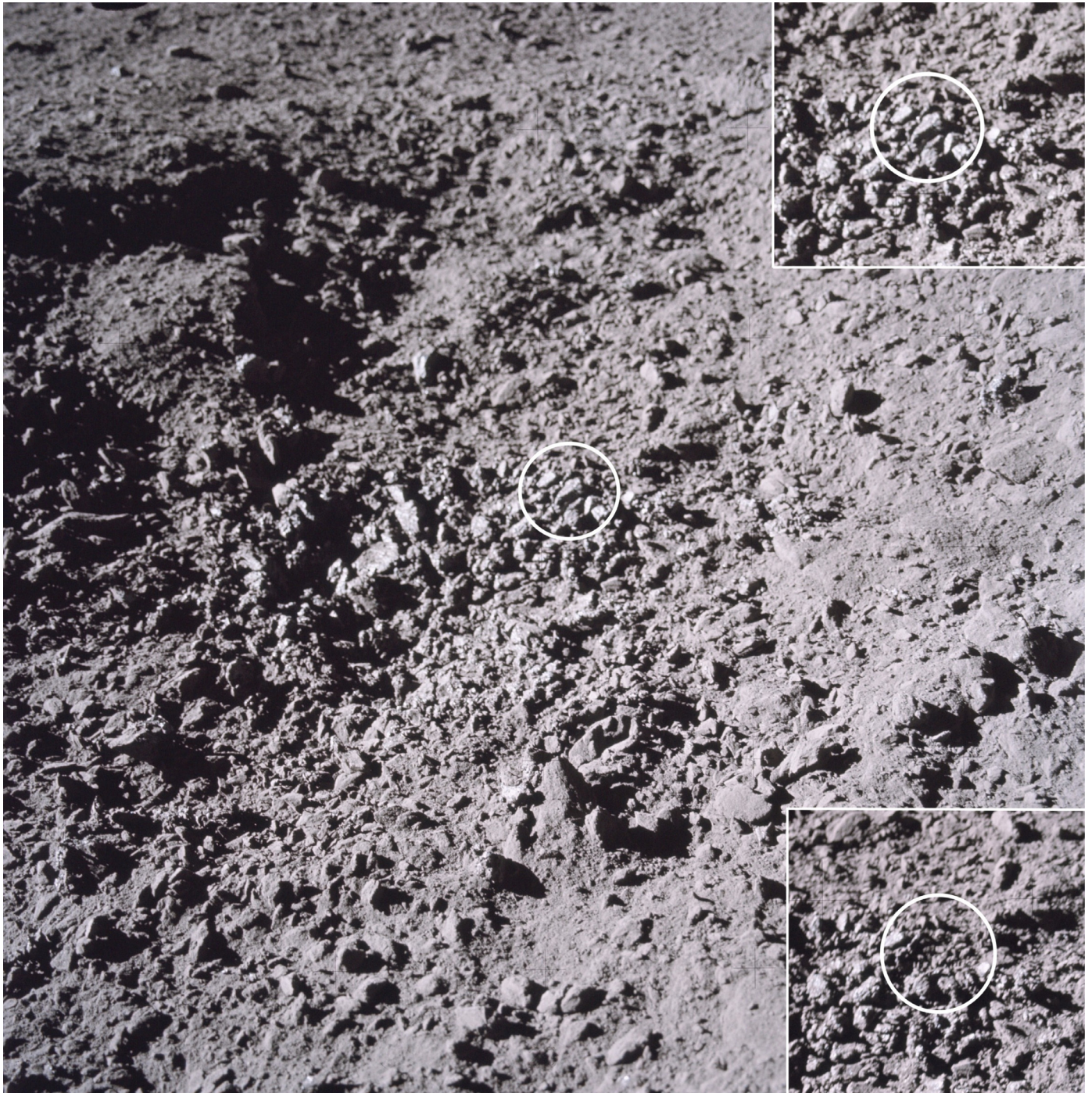
Fig. 25. One photo from a cross-sun stereo pair of the sample area. The elongated sample 70019 is shown centered within the white circle. (*Upper right inset*): Enlargement of the circled sample location. (*Lower right inset*): The same encircled sample area after the sample was removed. An anaglyph version of the stereo pair is given in Fig. 26. (NASA photo AS17-145-22188; lower inset from NASA photo AS17-145-22191).

have ever been acquired from any extraterrestrial body. Before these conclusions were published, however, discussions in preparation for Apollo 17 exploration suggested that impact glass in small lunar craters might provide data on the orientation of any recent lunar magnetic field existing at the time of cooling. Near the end of the second Apollo 17 lunar surface EVA, the senior author collected sample 70019 in pursuit of that objective. The sample came from a glassy mass in the center of a ∼3 m diameter impact crater about half way between the Apollo Lunar Surface Experiment Package (ALSEP) and the Lunar Module *Challenger*

(Figs. 24 and 25). Such a glass-coated sample implies that its orientation would have remained unchanged since formation because not enough time would have elapsed for micro-meteoritic impact to destroy the glass.

Sample 70019 consists of a regolith breccia fragment in a shiny, black glass matrix. The Field Geology team's write-up on 70019 (Wolfe et al., 1981, p. 25) does not refer to photographic documentation of its orientation and location during collection, merely stating that the location is unknown (Wolfe et al., 1981; Fig. 15, p. 26). Later cataloging by the Lunar and Planetary Institute
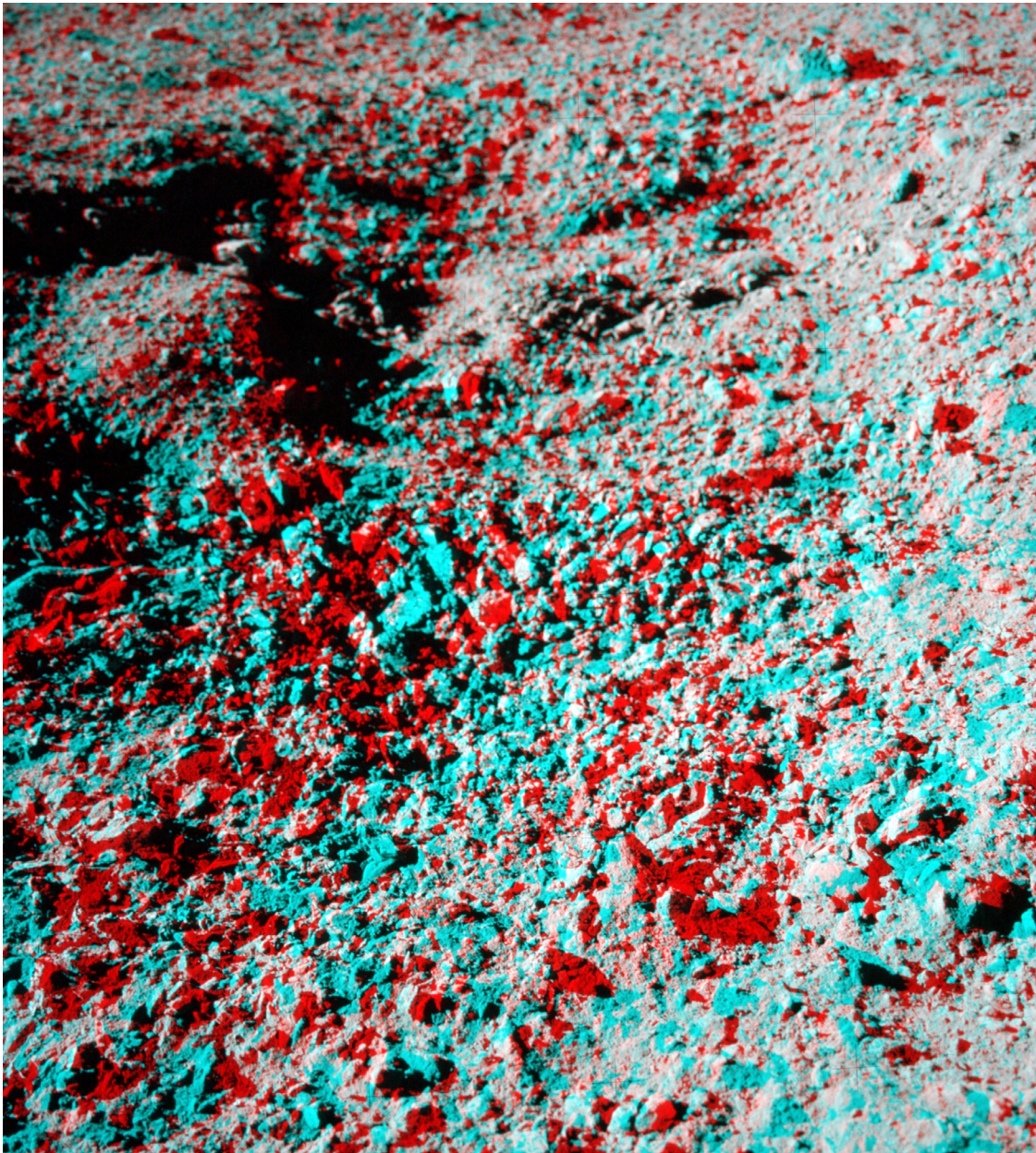
Fig. 26. The cross-sun "before" 3D view of the sample in situ. (From NASA photos AS17-145-22189 and -22188).

recognized only that the sample had been "collected from the bottom of a 3 m crater near the Apollo 17 lunar module" (LPI, 2015). One effort to use this impact glass to gather lunar magnetic field data did not take advantage of available "before" and "after" photographs that could have been used to determine the sample's in situ orientation (Pearce and Chao, 1977). That study confined itself to magnetic hysteresis measurements that reflected the concentration of iron metal in the sample. A paleomagnetic study of 70019 inferred an unusually stable natural remanent magnetization that formed in an apparent field of 2.5 μT (Sugiura et al., 1979); but it also did not use available sample orientation images.

Since Sugiura et al. (1979), no recent remanent magnetism analysis on 70019 has been conducted. The current condition of the remaining portions of sample 70019, however, will permit such a study (R. Zeigler and B. Weiss, *personal communications*). As described below, examination of the high quality "before", "after" cross-sun, and up-Sun stereo pairs documenting the sample's collection makes it possible to orient this sample in three dimensions

relative to its position as it cooled. Also, examination of a high resolution LROC image of the Apollo 17 landing site has provided the location of the crater from which 70019 was obtained.

The materials and methods required to determine the position of sample 70019 comprise the seven Apollo 17 lunar surface photos AS17-145-22185-22191 (ALSJ, 2015); the JPL *Horizons* online ephemeris program (Horizons, 2015); the close-range photogrammetry program, *iWitnessPro* (iWitnessPro, 2015); the 60 mm (focal length) Hasselblad camera calibration report (Lockheed Electronics Company, 1972); and the map of the x,y positions of the fiducial crosses on the reseau plates of the 60 mm cameras (Reseau Map, 2003) as described in the following sub-sections.

7.2. Location of the 70019 sample

The white circle in the cross-sun view in Fig. 25 marks the location of the rock sample, which is seen nearly broadside. The upper and lower right insets compare enlargements of the
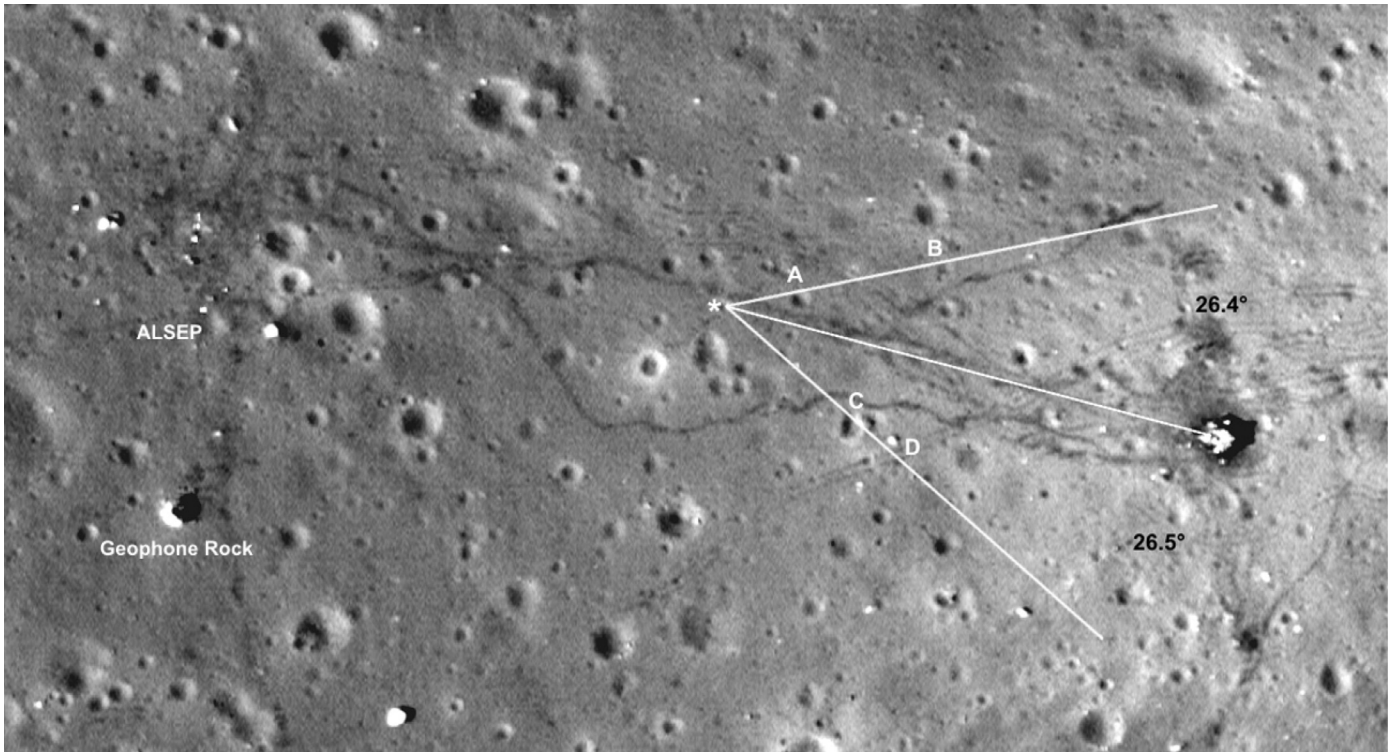
Fig. 27. A portion of the highest resolution LRO NAC photo of the Apollo 17 landing site taken on 08/14/2011 from an altitude of 22 km. The location of the 70019 crater (white star) can be compared with the identification markers A-D depicted in Fig. 24. The senior author initially proposed that this is the location of the 3-m crater shown in Fig. 24. The white lines denote the angular separations of the edges of Fig. 24 with respect to the camera line-of-sight measured from the reseau cross in the LMP's window. (NASA/ASU/GSFC photo M168000580).
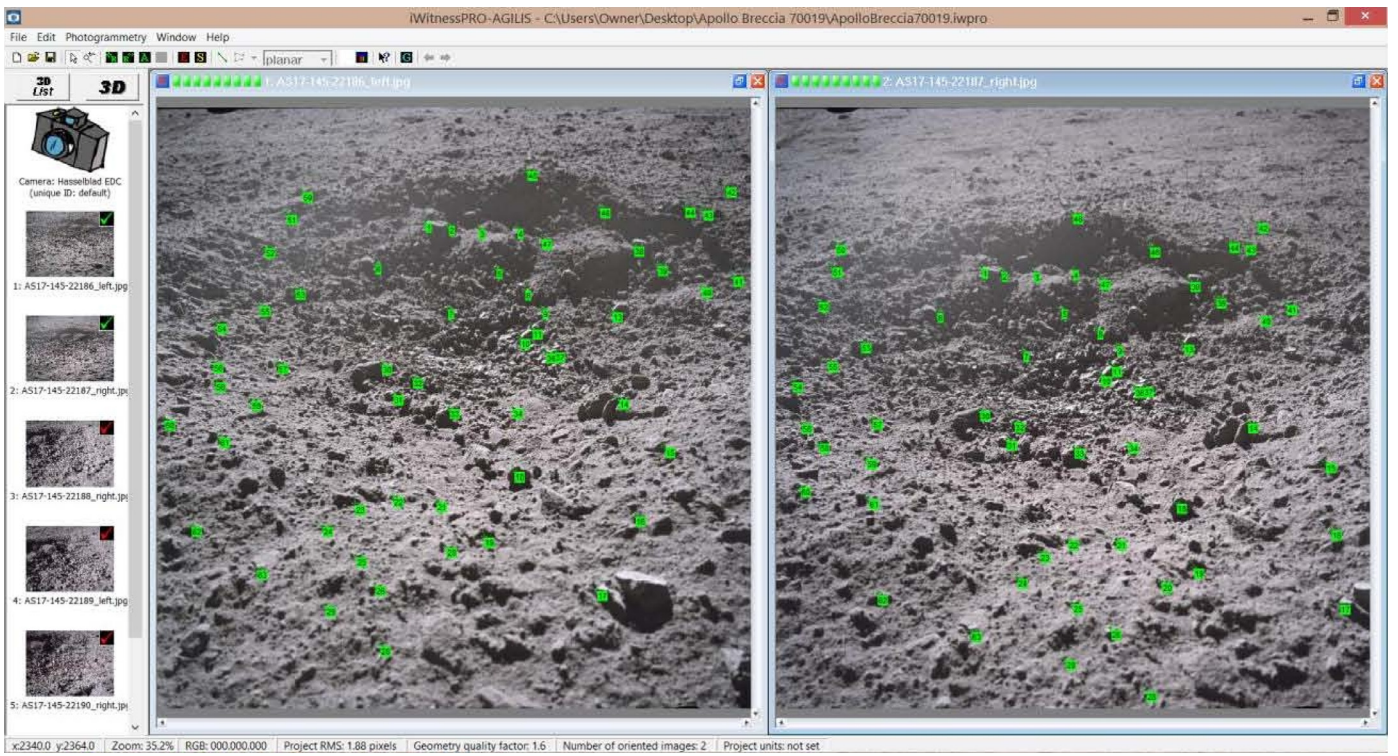
Fig. 28. Screen view of the display of the close-range photogrammetry program *iWitnessPro*. The left and right stereo images in the up-sun direction correspond to the first two thumbnails in the left sidebar panel. A partial series of rock target points are marked in the first two photographs. More were added in subsequent photos. The green labels indicate that the program has correctly determined the relative orientations of the target points between the two photos. The green tick marks in the first two thumbnails indicate that their corresponding images have been successfully triangulated.
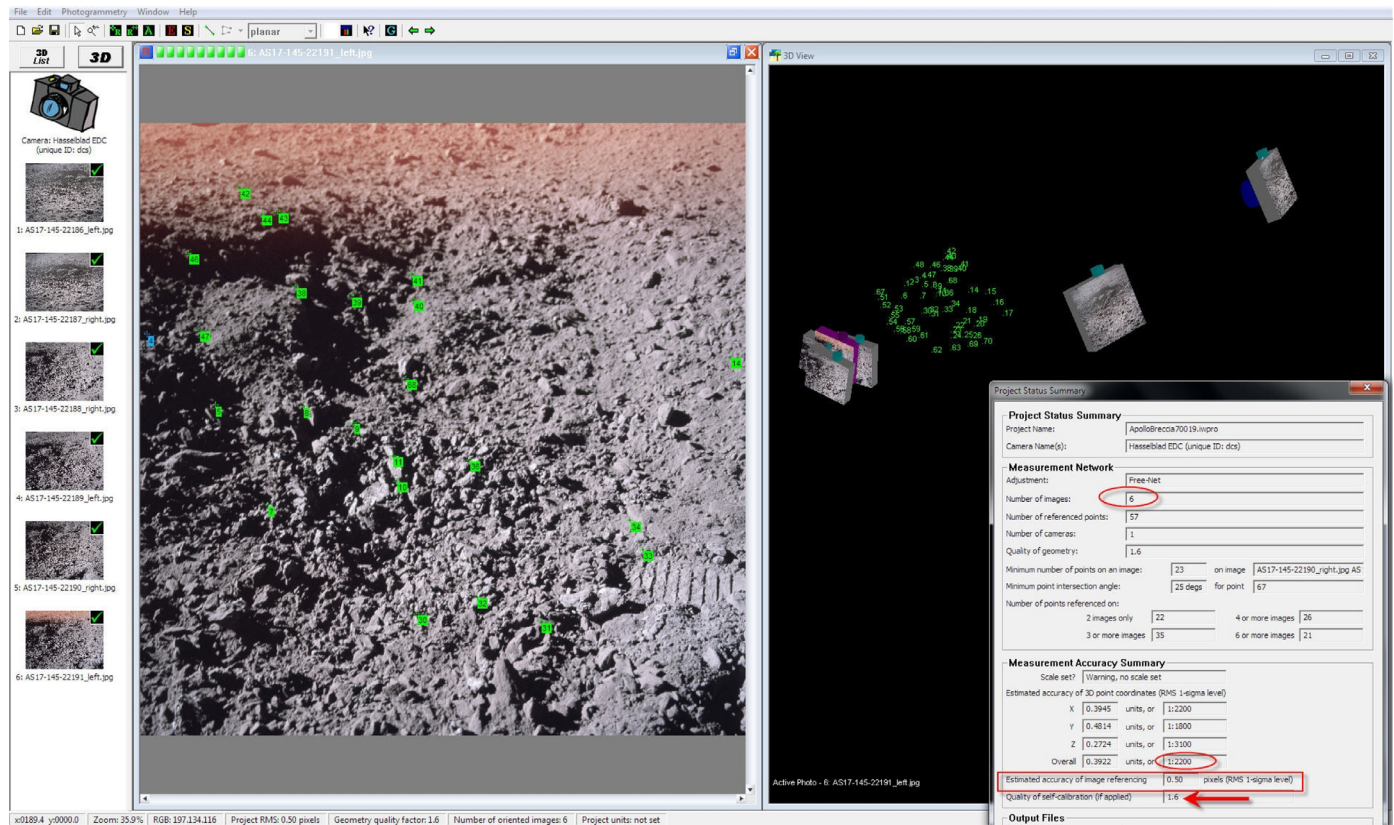
Fig. 29. (*left panel*): The screen display showing the final photo triangulated with its referenced target points in green. (*right panel*): The cloud of all measured target points together with the six triangulated positions in which the senior author held the Hasselblad camera in the cross-sun (leftmost) and up-sun (upper right) directions. The camera position framed in pink is the active photo displayed in the left panel. The smaller inset at right shows the quality of the triangulated model. The image referencing for all six images had an RMS (1-sigma) error of 0.5 pixel (Courtesy of Lee DeChant).

photographs "before" and "after" removal of the sample. An un-marked 3D anaglyph made from the stereo photo pair is given in Fig. 26 (Wells, 2015). A comparison of Figs. 25 and 26 allows the sample to be seen in situ. After these photos were taken, the senior author stepped closer to the sample, faced towards the *Challenger*, leaned over to his right and picked up the rock with a pair of sampling tongs. After picking up the rock, he turned and stepped out of the crater to his left; carefully double bagged the fragile sample; turned around; and took the stereo cross-sun "after" pair showing the rock's former location. The latter lay between two lines of smaller rocks forming a V-shape lying on its side with the open end towards the right, as indicated by the lower inset of Fig. 25.

7.3. Location of the 70019 crater

The locator photo of Fig. 24 can be used to scale the distance of the crater from the *Challenger*. Other identifying markers in the photo can also be used to locate the crater in an LROC photo of the site. Fig. 24 shows four such markers labeled A,B to the left of the lunar rover (LRV) tracks, and C,D to the right of the tracks. The 10.3° spacing of the reseau crosses on the photograph and the 2.83 m width of the prominent round part of the ascent stage (Grumman Aerospace Corporation, 1969; Fig. 2.2) enables the distance to the *Challenger* to be calculated relative to the line of sight of the camera which intersects the Lunar Module Pilot (LMP) window (Fig. 24, inset). The distance to the *Challenger* is therefore 119 m.

The reseau crosses can also be used to determine the angular separations of the left and right edges of the photo measured from the cross in the LMP window (left hand window in Fig. 24). These are almost the same, 26.5° for the right edge, and 26.4° for the left

edge. Corresponding lines can be placed on the highest resolution Lunar Reconnaissance Orbiter photo of the site measured from the putative 70019 crater. The results can be compared with Fig. 24 to verify the i.d. markers A,B and C,D and location of the 70019 crater. Fig. 27 shows these lines.

7.4. Orientation of sample 70019

The orientation of any of the Apollo samples can usually be determined with the aid of a close-range photogrammetry program such as those used in geology, archaeology, architecture, or accident forensics. These programs analyze the location and direction of numerous target points in a set of photos taken at various angles around the scene to be duplicated. The relative orientation of a specific sample in the reconstructed 3D scene can then be measured with respect to the absolute azimuth and elevation of the sun computed for the time(s) of the exposed photograph(s). The particular software used here was *iWitness Pro*™ ver. 3.6 (iWitnessPro, 2015) for the reconstruction of the 70019 sample area and relative orientation measurements. The azimuth and elevation of the sun for the time and date in question were computed from the online JPL *Horizons* web interface using the pre-coded observer site for Apollo 17 (Horizons, 2015).

Photo dates and times for AS17-145-22186-22191 were taken from the time sequences in the *Apollo Lunar Surface Journal* (ALSJ, 2015). Because of the delay in the launch of Apollo 17, all times for this mission at Ground Control and in the journal had 2 hr 40 min added to the actual ground elapsed time (GET) so that the times already printed in the cuff checklists that each astronaut wore on the surface would not have to be changed. GET (converted to UT) was used in the web interface. The averaged time was

Fig. 30. To determine the orientation of the rock sample 70019, shown at middle right by the red line with white crosses, a shadow line was selected at upper middle left from a rock with straight edges raised high enough to cast shadows as unobstructed as possible. These two lines were transferred to the 3D model. The orientation of the shadow line is the solar azimuth. The orientation of 70019 is that angle plus the measured angle between the shadow line and the rock sample line. Its inclination, or slope, is that of the red line with respect to the x,y plane of the model. (NASA photo AS17-145-22189).

1972-Dec-13 06:11:00 UT (a precise value is not needed). The *Horizons* program gave a solar azimuth of 102.9°, and an elevation of 29.4° for this entry.

Generally, the Apollo sample photos had a gnomon in the field of view. The shadow of the gimbaled, vertical post, which came to rest pointing upwards to the zenith after emplacement, determined the solar azimuth direction. In the case of sample 70019, however, the gnomon was not available. A long shadow from an unobstructed rock in the area was therefore used instead.

Fig. 28 illustrates the marking of selected target points (recognizable rocks) in two of the six photos used. This procedure is followed photo-by-photo until a number of common points in each have been marked. The program is quite versatile in that it will predict the locations of target points in the subsequent photos after at least two photos have been triangulated. More points can also be selected which may be visible only in the later photos. With these observations, the program computes the positions of the camera and the orientation of the area. By drawing a straight

line along a chosen rock shadow, its position relative to the orientation of the area is determined. Similarly, a straight line drawn along the direction of the rock sample gives its orientation relative to the shadow line.

Fig. 29 shows the sixth referenced photo (left panel) and the cloud of target points and camera positions (right panel) of the model. Fig. 30 illustrates the lines used to determine the orientation of the sample. The red line on the sample and the white line along the shadow were transferred to the perspective model.

Fig. 31 illustrates the final perspective model determined by the triangulation. The turquoise line in Fig. 31 gives the selected rock shadow line used for the solar azimuth taken from Fig. 30. The corresponding line along the 70019 sample cannot be seen in this figure because the scale is too small. The program, however, produces a plan view of all the measured points and lines (not shown here), i.e., an x,y cross-section of the model from which the orientation of the sample can be determined. The result is 102.9° solar az. + 145° relative rock sample az. = 247.9° absolute. Similarly, the
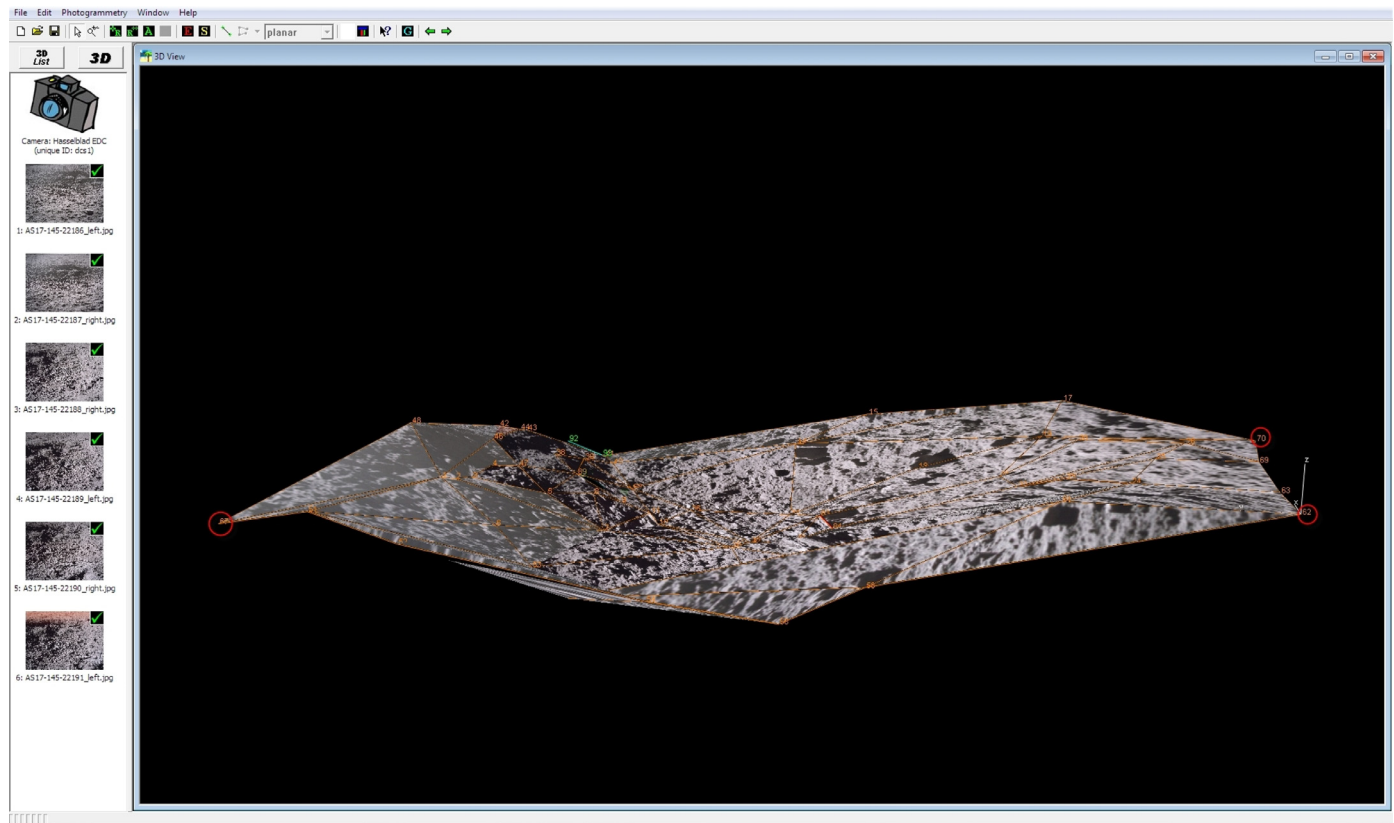
Fig. 31. Perspective view of the 70019 crater determined from the points triangulated in the six photos seen at left and texture mapped by parts of those photos. The up-sun direction is approximately looking left across the crater from the leftmost red circle at right towards the direction of the brighter surface and red circle at left. Orange lines form a polygonal network from the numbered points. The rock sample 70019 cannot be seen at this scale. The turquoise line on the left slope is a rock's uninterrupted shadow line chosen as the solar azimuth (see Fig. 30). The orientation of 70019 is the angle between the shadow line and the rock sample line added to the solar azimuth. Its inclination was deduced directly by determining the upper and lower points of the rock sample with respect to the x,y plane of the model and dividing that distance by the length of the rock. (Courtesy of Lee DeChant).

inclination of the rock sample is 9.7° This latter value is just the slope of the rock sample in Fig. 30 computed with respect to the model horizontal x,y plane as described in the caption for Fig. 31.

7.4. Summary of sample 70019′s location and orientation

The highest resolution LROC photo of the Apollo 17 landing site with the aid of the Apollo locator photo taken in the direction of the *Challenger* made it possible to identify the likely, small, glass-bottomed crater from which sample 70019 was taken more than 44 years earlier. The idea to return a young, glass-coated sample was conceived prior to and again during the planning stages of the mission because of the likelihood that its position would have remained unaltered since formation and cooling through the Curie point. The suite of six stereo photos documented the sample's location, but they were never used in paleomagnetic or paleodirectional studies, in part because of the difficulty in precisely duplicating the rock's position in the laboratory. Today, however, the availability of close-range photogrammetric computer programs can reproduce the in situ characteristics of a geological setting utilizing a series of photos made at various angles around the site. These photos do not necessarily have to have stereo separation.

The *iWitnessPro* program used here made a determination of 70019′s orientation and tilt possible. The program enabled us to produce a 3D texture mapped model from which the data in the x,y cross-section of Fig. 31 were taken. Experience with the versatility of this approach indicates that similar reproductions of the geological settings documented in photographs related to the Camelot rim samples mentioned at the beginning of Section 4.2

and to the melt-breccia contacts in boulders at Stations 6 and 7 as noted in Section 2.4 also might be possible.

8. Conclusions

After over 44 years since the Apollo 17 mission to the Taurus–Littrow valley, new data from the Lunar Reconnaissance Orbiter's (LRO) cameras and radar, Chandrayaan's Moon Mineralogy Mapper (M^3), and renewed sample analyses provide improved context of the geological exploration that mission undertook. The new orbital data provide confirmation of the Imbrian age of the Sculptured Hills ($^{40}Ar/^{39}Ar$ < 3.83 Ga) and the probable stratigraphic position of Crisium melt-breccia ($^{40}Ar/^{39}Ar$ ~3.93 Ga) beneath that of Serenitatis ejecta ($^{40}Ar/^{39}Ar$ ~3.83 Ga). With this additional information, the origins and context of samples from the North Massif and Sculptured Hills and their possible connections to large impact basins (Crisium, Serenitatis, Imbrium) become clearer.

Evidence suggests that the Sculptured Hills are ejecta that comprise portions of a large Mg-suite pluton excavated from the Imbrium basin. Pyroclastic fissures that erupted dark ash have been identified in the Sculptured Hills and on the North Massif. The accumulation of ash around the proposed fissure on the North Massif apparently resulted in a relatively young debris flow of dark ash.

The new visible and radar images of both the bright and more subdued portions of the light-mantle indicate multiple debris flow events created these features. This observation leads to the conclusion that faulting events likely triggered the light mantle avalanches and the paint splatter debris flows in the Sculptured Hills. The apparent existence of two light mantle avalanches of sig-

nificantly different ages makes it unlikely that secondary impacts from Tycho triggered either one. Seismic shocks associated with Lee-Lincoln thrust faulting appear to be a more likely triggering mechanism. The burial of the Lee-Lincoln fault scarp by the light mantle avalanche and the scarp's spatial association with the Nansen Moat at the base of the South Massif, suggest that the fault probably occurred or was reactivated between about 70 and 110 Ma.

Lastly, with the high-spatial resolution of the orbital images as well as excellent rectification enabled by the accurate LOLA based control network (Wagner et al., 2017) and new computer programs, the source crater for the impact melt of sample 70019 has been identified and the exact orientation of this sample prior to collection is now known. With this detailed information the sample now has a completely "new life" as a source for constraining the absolute direction of the paleomagnetic field when this recent crater formed. Similarly, the re-interpretation that Camelot Crater rim boulders are in situ upper wall rocks, a possible horizontal orientation of contacts in the Station 6 and 7 boulders, and the use of these new sample orientation techniques may add additional samples to the search for data on the orientations of ancient lunar magnetic fields.

The enhanced analysis enabled by new data sets and images shows that the Apollo 17 mission sampled materials from events recorded in a wide range of the lunar stratigraphic column, from the basin forming events that deposited and modified the massifs and Sculptured Hills to the relatively recent craters that formed in the valley floor to the avalanche events that created the light mantle. The joint analysis of multiple datasets over a single landing site clearly shows the value of integrating such data in the search for correct interpretations and for the continued acquisition of similar data across the Moon. Such analysis also shows what will be possible for future lunar surface exploration and in the selection of scientifically important sample sites.

When it is possible to return to the Taurus–Littrow field area, as often is the case with terrestrial fieldwork, our current work suggests specific related targets for additional investigation and sampling.

1. A large number of tracked boulders at the bases of the North and South Massifs should be documented and sampled in order to more fully resolve the history of the many basins whose formative impacts deposited ejecta in the area. If feasible, in situ sources of these boulders should be investigated and sampled in order to understand their context in outcrop.
2. Investigation and sampling of numerous crests in the Sculptured Hills should be undertaken in order to understand the structure, compositional variability, and age of a large Mg-Suite pluton. Samples from Bear Mountain, Family Mountain, and other features that project above the subfloor basalt would also constrain the possibility of a shared source of these features with the Sculptured Hills.
3. A broad relative age spectrum of impact craters having exposed basaltic wall rocks at their rims and cooled impact melt concentrations in situ should be investigated to obtain oriented samples for lunar magnetic field investigations. Improved photographic procedures in the field connected with the use of close-range photogrammetric programs would facilitate post-orientation determinations.
4. Regolith samples gathered as necessary to confirm multiple ages of debris flows from valley walls and the Sculptured Hills and to better understand their flow mechanics, volatile abundances, and possible relationships to continued moonquakes.

On-going considerations of various additional aspects of the geology and samples related to Taurus–Littrow, but beyond the scope of this paper, reveal many other new field investigations to

undertake in the future when that opportunity presents itself. We should work toward that end.

Supplementary materials

Supplementary material associated with this article can be found, in the online version, at doi:10.1016/j.icarus.2016.11.042.

References

Aeschlimann, U., et al., 1982. On the age of cumulate norite 78236, Abstract, Lunar and Planetary Science Conference 13. Lunar Planetary Institute, Houston (see Meyer, C, 2008, Lunar Sample Compendium, http://curator.jsc.nasa.gov/lunar/lsc/78235.pdf).

Grumman Aerospace Corporation, 1969. Vehicle Familiarization Manual: Lunar Module LM10 through LM14, LMA790-2, Fig. 2.2, p. 2-3, Grumman Aerospace Corp., Nov. 1 (LM12 was flown as the Apollo 17 LM, *Challenger*).

ALSJ, 2015. https://www.hq.nasa.gov/alsj/a17/images17.html (use image 145-22185 to get to the group) and https://www.hq.nasa.gov/alsj/a17/a17.clsout2.html#1471953 (for the transcript and annotations).

Apollo Lunar Geological Investigation Team, 1972. Geologic setting of the Apollo 15 samples. Science 175, 407–415.

Boardman, J.W., Pieters, C.M., Green, R.O., Lundeen, S.R., Varanasi, P., Nettles, J., Petro, N., Isaacson, P., Besse, S., Taylor, L.A., 2011. Measuring moonlight: an overview of the spatial properties, lunar coverage, selenolocation, and related level 1B products of the Moon Mineralogy Mapper. J. Geophys. Res. 116, E00G14. doi:10.1029/2010JE003730.

Bray, V.J., Tornabene, L.L., Keszthelyi, L.P., et al., 2010. New insight into lunar impact melt mobility from the LRO camera. Geophys. Res. Lett. 37, L21202. doi:10.1029/2010GL044666.

Cadogan, P.H., Turner, G., 1976. The chronology of the Apollo 17 Station 6 boulder. In: Merrill, R.B. (Ed.), Lunar and Planetary Science Conference Proceedings, 7, pp. 2267–2285.

Carrier III, W.D., 1973. Lunar soil grain size distribution. Moon 6, 250–263.

Carrier III, W.D., Bromwell, L.G., Martin, R.T., 1973. Behavior of returned lunar soil in vacuum. J. Soil Mech. 99, 979–996.

Cheek, L.C., Donaldson Hanna, K.L., Pieters, C.M., Head, J.W., Whitten, J.L., 2013. The distribution and purity of anorthosite across the Orientale basin: new perspectives from Moon Mineralogy Mapper data. J. Geophys. Res. 118, 1805–1820.

Collins, G.S., Melosh, H.J., 2003. Acoustic fluidization and the extraordinary mobility of sturzstroms. J. Geophys. Res. 108. doi:10.1029/2003JB002465.

Croft, S.K., 1980. Cratering flow fields - implications for the excavation and transient expansion stages of crater formation. In: Lunar and Planetary Science Conference 11, pp. 2347–2378.

Crozaz, G., Drozd, R., Hohenberg, C., Morgan, C., Ralston, C., Walker, R., Yuhas, D., 1974. Lunar surface dynamics: some general conclusions and new results from Apollo 16 and 17. In: Proceedings Lunar Science Conference 5, pp. 2475–2499.

Dalrymple, G.B., Ryder, G., 1993. ⁴⁰Ar/³⁹Ar age spectra of Apollo 15 impact melt rocks by laser step-heating and their bearing on the history of lunar basin formation. J. Geophys. Res. 98 (E7), 13085–13095.

Dalrymple, G.B., Ryder, G., 1996. Argon-40/Argon-39 age spectra of Apollo 17 highlands breccia samples by laser step heating and the age of the Serenitatis basin. J. Geophys. Res. 101 (E11), 26069–26084. doi:10.1029/96JE02806.

Denevi, B.W., Koeber, S.D., Robinson, M.S., Garry, W.B., Hawke, B.R., Tran, T.N., Lawrence, S.J., Keszthelyi, L.P., Barnouin, O.S., Ernst, C.M., Tornabene, L.L., 2010. Physical constraints on impact melt properties from Lunar Reconnaissance Orbiter Camera images. Sci. Direct 219, 665–675.

Drozd, R.J., Hohenberg, C.M., Morgan, C.J., Podosek, F.A., Wroge, M.L., 1977. Cosmic-ray exposure history at Taurus-Littrow. In: Merril, R.B. (Ed.), Lunar and Planetary Science Conference Proceedings, 8, pp. 3027–3043.

Eberhardt, P., Eugster, O., Geiss, J., Graf, H., Grogler, N., Morgeli, M., Stettler, A., 1974. 81Kr-Kr exposure ages of some Apollo 14, Apollo 16 and Apollo 17 rocks (abs). In: Lunar Science Conference 7. Lunar Planetary Institute, Houston, pp. 233–235.

Edmunson, J, Borg, L.E., Nyquist, L.E., Asmerom, Y., 2009. A combined Sm–Nd, Rb–Sr, and U–Pb isotopic study of Mg-suite norite 78238: further evidence for early differentiation of the Moon. Geochim. Cosmochim. Acta 73, 514–527. doi:10.1016/j.gca.2008.10.021.

Evensen, N.M., Murthy, V.R., Coscio Jr., M.R., 1973. Rb-Sr ages of some mare basalts and the isotopic and trace element systematics in lunar fines. In: Lunar and Planetary Science Conference Proceedings, 4, p. 1707.

Fassett, C.I., Thomson, B.J., 2014. Crater degradation on the lunar maria: topographic diffusion and the rate of erosion on the Moon. J. Geophys. Res. 119, 2255–2271.

Fassett, C.I., Thomson, B.J., 2015. A landscape evolution perspective on how young is young on the lunar surface. Lunar and Planetary Science Conference 46 Abstract 1120.

Fassett, C.I., Head, J.W., Smith, D.E., Zuber, M.T., Neumann, G.A., 2011. Thickness of proximal ejecta from the Orientale basin from Lunar orbiter laser altimeter (LOLA) data: implications for multi-ring basin formation. Geophys. Res. Lett. 38, 17201. doi:10.1016/j.gca.2008.10.021.

Fassett, C.I., Head, J.W., Kadish, S.J., Mazarico, E., Neumann, G.A., Smith, D.E., Zuber, M.T., 2012. Lunar impact basins: Stratigraphy, sequence and ages from superposed impact crater populations measured from Lunar orbiter laser altimeter (LOLA) data. J. Geophys. Res. 117, E00H06.

Fleischer, R.L., Price, P.B., Walker, R.M, 1975. Ancient energetic particles in space. In: Fleischer, R.L., Price, P.B., Walker, R.M. (Eds.), Nuclear Tracks in Solids. University of California Press Chapter 6.

Fuller, M., Cisowski, S.M., 1987. Lunar paleomagnetism. In: Jacobs, J.A. (Ed.), Geomagnetism. Academic Press, Orlando, pp. 307–455.

Gnos, E., Hofmann, B.A., Al-Kathiri, A., et al., 2004. Pinpointing the source of a Lunar Meteorite: implications for the evolution of the Moon. Science 305, 657–659.

Grange, M.L., Nemchin, A.A., Pidgeon, R.T., Timms, N., Muhling, J.R., Kennedy, A.K., 2009. Thermal history recorded by the apollo 17 impact melt breccia 73217. Geochim. Cosmochim. Acta 73, 3093–3107.

Green, R.O., Pieters, C., Mouroulis, P., et al., 2011. The Moon mineralogy mapper (M3) imaging spectrometer for lunar science: instrument description, calibration, on-orbit measurements, science data calibration and on-orbit validation. J. Geophys. Res. 116. doi:10.1029/2011JE00G19.

Hartmann, W.K., Wood, C.A., 1971. Moon: origin and evolution of multi-ring basins. Moon 3, 3–78.

Head, J.W., 1974. Morphology and structure of the Taurus–Littrow highlands (Apollo 17) – evidence for origin and evolution. Moon 9, 327–395.

Head, J.W., 1979. Serenitatis multi-ringed basin: regional geology and basin ring interpretation. Moon Planets 21, 439–462.

Heiken, G., Vaniman, D., French, B.M., 1991. Lunar Sourcebook. Cambridge University Press, Cambridge, p. 736.

Heiken, G.H., McKay, D.S., 1974. Petrology of Apollo 17 soils. In: Lunar Science Conference 5, pp. 843–860.

Henriksen, M.R., et al., 2017. Extracting accurate and precise topography from LROC narrow angle camera stereo observations. Icarus 283, 122–137.

Hiesinger, H., van der Bogert, C.H., Pasckert, J.H., Funcke, L., Giacomini, L., Ostrach, L.R., Robinson, M.S., 2012. How old are young lunar craters? J. Geophys. Res. 117, E00H10.

Hood, L.L., Huang, Z., 1991. Formation of magnetic-anomalies antipodal to lunar impact basins - 2-dimensional model-calculations. J. Geophys. Res. 96, 9837–9846.

Horizons, 2015. http://ssd.jpl.nasa.gov/horizons.cgi. A web-based tutorial describing how to generate an ephemeris is also given at: http://ssd.jpl.nasa.gov/?horizons_tutorial.

Horn, P., Jessberger, E.K., Kirsten, T., Richter, H., 1975. Ar39/Ar40 dating of lunar rocks - Effects of grain size and neutron irradiation. In: Lunar and Planetary Science Conference Proceedings, 6, pp. 1563–1591.

Hörz, F., Brownlee, D.E., Fechtig, H., Hartung, J.B., Morrison, D.A., Neukum, G., Schneider, E., Vedder, J.F., Gault, D.E., 1973. Lunar microcraters: implications for the micrometeoroid complex. Planet. Space Sci. 23, 151–172.

Howard, K.A., Larsen, B.R., 1972. Orbital-Science Investigation: Part G: Lineaments that are Artifacts of Lighting, in Apollo 15 Preliminary Science Report NASA 289, 25-58–25-62.

Hudgins, J.A., Spray, J.G., Kelley, S.P., Dorotev, R.L., Sherlock, S.C., 2008. A laser probe 40Ar/39Ar and INAA investigation of four Apollo granulitic breccias. Geochim. Cosmochim. Acta 72, 5781–5798. doi:10.1016/j.gca.2008.10.021.

Huneke, J.C., Jessberger, E.K., Podosek, F.A., Wasserburg, G.J., 1973. 40Ar/39Ar measurements in Apollo 16 and 17 samples and the chronology of metamorphic and volcanic activity in the Taurus-Littrow region. In: Lunar and Planetary Science Conference Proceedings, Vol. 4, p. 1725.

Hurwitz, D., Kring, D.A., 2016. Identifying the geologic context of Apollo 17 impact melt breccias. Earth and Planetary Science Letters 436, 64–70.

Iverson, R.M., 1997. The physics of debris flows. Rev. Geophys. 35, 245–296. doi:10.1029/97RG00426.

iWitnessPro, 2015. http://www.iwitnessphoto.com/. A 12-step online tutorial through the program essentials showing how to use the software is given at: http://www.iwitnessphoto.com/tour/0.html. A more detailed PDF user guide can be downloaded from: http://www.iwitnessphoto.com/solutions/iwitness_tutorial.pdf.

Jiang, M., Shen, Z., Thornton, C., 2013. Microscopic contact model of regolith for high efficiency discrete element analysis. Comput. Geotech. 54, 104–116.

Kissin, S.A, 1982. Phase relations involving pyrrhotite below 350 °C. Econ. Geol. 77, 1739–1754.

Klima, R.L., Peters, C.M., Boardman, J.W., et al., 2011. New insights into lunar petrology: distribution and composition of prominent low-Ca pyroxene exposures as observed by the Moon mineralogy mapper (M3). J. Geophys. Res.J. Geophys. Res. 116. doi:10.1029/2010JE003719.

Kirsten, T., Horn, P., Heymann, D., 1973. Chronology of the Taurus-Littrow region I: Ages of two major rock types from the Apollo 17-site. Earth and Planetary Science Letters 20, 125–130.

Kirsten, T., Horn, P., 1974. Chronology of the Taurus-Littrow region. In: III - Ages of mare basalts and highland breccias and some remarks about the interpretation of lunar highland rock ages. Lunar and Planetary Science Conference Proceedings, 5, pp. 1451–1475.

Kovach, R.L., Watkins, J.S., Talwani, P., 1973. Lunar Seismic Profiling Experiment, Apollo 17 Preliminary Science Report NASA SP-330, 10-4–10-6.

Liu, D., Jolliff, B.L., Zeigler, R., et al., 2012. Comparative zircon U–Pb geochronology of impact melt breccias from apollo 12 and lunar meteorite SaU 169, and implications for the age of the Imbrium impact. Earth Planet. Sci. Lett. 319-320, 277–286.

Lockheed Electronics Company, Calibration of Apollo 16 Lunar Surface 60 mm Hasselblad Cameras on Wild T-4 Goniometer. Lockheed Electronics Co., Houston Aerospace Systems Division, LEC/HASD No. 640-TR-055, Project Work Order 63-0117-5704, Houston, Feb. 4, 1972, This Apollo 17 camera, S/N1023, originally was to be flown on the Apollo 16 mission but ultimately was assigned to Apollo 17. The senior author used this camera to document 70019 because it was loaded with a color film magazine.

LPI, 2015. http://www.lpi.usra.edu/lunar/samples/atlas/detail/?mission=Apollo%2017&sample=70019

Lucchitta, B.K., 1972. Geologic map of part of the Taurus–Littrow region of the Moon. In: Scott, D.H., Lucchitta, B.K., Carr, M.H. (Eds.), Geologic Maps of the Taurus–Littrow Region of the Moon. U.S. Geological Survey Misc. Geological Investigations Map I-800 Sheet 2, Scale, 1:50,000.

Lucchitta, B.K., 1977. Crater clusters and light mantle at the Apollo 17 site – a result of secondary impact from Tycho. Icarus 30, 80–96.

Lucchitta, B.K., Sanchez, A.G., 1975. Crater studies in the Apollo 17 region. In: Lunar Science Conference, 6th Proceedings, Geochim. Cosmochim. Acta, pp. 2427–2441.

Lugmair, G.W., Scheinin, N.B., Marti, K., 1975. Sm-Nd age and history of Apollo 17 basalt 75075 - Evidence for early differentiation of the lunar exterior. In: Lunar and Planetary Science Conference Proceedings, 6, pp. 1419–1429.

Lunar Science Institute, 1973-present. Proceedings Lunar Science Conferences 4-8 and Lunar and Planetary Science Conferences 9-21. Lunar and Planetary Institute, Houston.

McCauley, J.F., 1981. Orientale exterior. In: Wilhelms, D.E. (Ed.), The Geologic History of the Moon. U.S. Geological Survey Professional Paper 1348, pp. 66–72.

Melosh, H.J., 1979. Acoustic fluidization: a new geologic process? J. Geophys. Res. Solid Earth 84, 7513–7520.

Mercer, C., 2015, personal communication of recalculated data from Cadogan P.H., and G. Turner, 1976, The chronology of the Apollo 17 Station 6 boulder. Lunar Science Conference 7, p. 2267-2285, and Stettler A., et al., 1974, 39Ar- 40Ar ages of samples from the Apollo 17 Station 7 boulder and implications for its formation, Earth and Planetary Science Letters, 23, p. 453-461.

Mercer, C.M., Young, K.E., Weirich, J.R., Hodges, K.V., Jolliff, B.L., Wartho, J.-A., van Soest, M.C., 2015. Refining lunar impact chronology through high spatial resolution 40Ar/39Ar dating of impact melts. Sci. Adv. 1 (1e1400050). doi:10.1126/scoadv.1400040.

Merle, R.E., Nemchin, A.A., Grange, M.L., Whitehouse, M.J., Pidgeon, R.T., 2014. High resolution U-Pb ages of Ca-phosphates in Apollo 14 breccias: implications for the age of the Imbrium impact. Meteorit. Planet. Sci. 49, 2241–2251.

Merrill, M.T., McElhinny, M.W., McFadden, P.L., 1998. The Magnetic Field of the Earth: Paleomagnetism, the Core, and the Deep Mantle, 2nd ed. Academic Press, San Diego.

Meyer, C., 2008. Lunar Sample Compendium http://curator.jsc.nasa.gov/lunar/lsc/.

Minnaert, M., 1961. Photometry of the Moon. In: Kuiper, G.P., Middlehurst, B.M. (Eds.), Planets and Satellites. University of Chicago Press, Chicago, p. 601.

Mitchell, T.M., Smith, S.A.F., Anders, M.H., Toro, G.D., Nielsen, S., Cavallo, A., Beard, A.D., 2015. Catastrophic emplacement of giant landslides aided by thermal decomposition: Heart Mountain, Wyoming. Earth Planet. Sci. Lett. 411, 199–207. doi:10.1016/j.epsl.2014.10.051.

Morris, R.V., 1978. Lunar Science Conference 9. Geochim. Cosmochim. Acta (Supplement 10) 2287–2297.

Murthy, V.R., Coscio Jr., M.R., 1977. Rb-Sr Isotopic Systematics and Initial SR Considerations for Some Lunar Samples. In: Lunar and Planetary Science Conference, 8, pp. 706–708.

NASA, 1973. Apollo 17 Preliminary Science Report. National Aeronautics and Space Administration, Washington NASA SP-330.

Nemchin, A.A., Tidgeon, R.T., Healy, D., Grange, M.L., Whitehouse, M.J., Vaughn, J., 2009. The comparative behavior of apatite-zircon U-Pb systems in Apollo 14 breccias: implications for the thermal history of the Fra Mauro formation. Meteorit. Planet. Sci. 44, 1717–1734.

Nozette, S., Spudis, P., Bussey, B., et al., 2010. The Lunar reconnaissance orbiter miniature radio frequency (Mini-RF) technology demonstration. Space Sci. Rev. 150, 285–302.

Nyquist, L.E., Jahn, B.-M., Bansal, B.M., Wiesmann, H., 1974. Taurus-Littrow chronology - Some constraints on early lunar crustal development. In: Lunar and Planetary Science Conference Proceedings, 5, pp. 1515–1539.

Nyquist, L.E., Bansal, B.M., Wiesmann, H., 1975. Rb-Sr ages and initial Sr-87/Sr-86 for Apollo 17 basalts and KREEP basalt 15386. In: Lunar and Planetary Science Conference Proceedings, 6, pp. 1445–1465.

Nyquist, L.E., Shih, C.-Y., Wooden, J.L., Bansal, B.M., Wiesmann, H., 1979. The SR and Nd isotopic record of Apollo 12 basalts - Implications for lunar geochemical evolution. In: Hinners, N.W. (Ed.), Lunar and Planetary Science Conference Proceedings, 10, pp. 77–114.

Nyquist, L.E., Reimold, W.U., Bogard, D.D., Wooden, J.L., Bansal, B.M., Wiesmann, H., Shih, C.-Y, 1981. A comparative Rb-Sr, sm-nd and K-Ar study of shocked norite 78236: evidence of slow cooling in the lunar crust? In: Lunar and Planetary Science Conference 12, pp. 67–97.

Paces, J.B., Neal, C.R., Taylor, L.A., Nakai, S.I., Halliday, A.N., 1991. A strontium and neodymium isotopic study of Apollo 17 high-Ti mare basalts - Resolution of ages, evolution of magmas, and origins of source heterogeneities. Geochimica et Cosmochimica Acta 55, 2025–2043.

Pearce, G.W., Chao, C.-L., 1977. Lunar Science Conference 8. Geochim. Cosmochim. Acta (Supplement 8) 669–677.

Petro, N.E., Pieters, C.M., 2006. Modeling the provenance of the Apollo 16 regolith. J. Geophys. Res. 111, 09005.

Petro, N.E., Pieters, C.M., 2008. The lunar-wide effects of basin ejecta distribution on the early megaregolith. Meteorit. Planet. Sci. 43, 1517–1529.

Petro, N., Klima, R.L., Ostrach, L.R., 2015. Constraining the origin of Apollo 17's station 8 boulder: implications for the origin of the sculptured hills and the Mg–suite. Lunar and Planetary Conference 46. Lunar and Planetary Institute, Houston Abstract 2687.

Petrowski, C., Kerridge, J.F., Kaplan, I.R., 1974. Lunar and Planetary Science Conference 5. Geohim. Cosmochim. Acta (Supplement 5) 1943.

Phinney, D., Kahl, S.B., Reynolds, J.H., 1975. Ar40/Ar39 dating of Apollo 16 and 17 rocks. In: Lunar and Planetary Science Conference Proceedings, 6, pp. 1593–1608.

Pike, R.J., 1974. Depth/diameter relations of fresh lunar craters: revision from spacecraft data. Geophys. Res. Lett. 1, 291–294.

Plescia, J.B., Spudis, P.D., 2014. Impact melt flows at Lowell crater. Planet. Space Sci. 103. doi:10.1016/j.pss.2014.08.003.

Raney, R.K., 2007. Hybrid-polarity SAR architecture. IEEE Trans. Geosci. Remote Sens. 45, 3397–3404. doi:10.1109/TGRS.2007.895883.

Raney, R.K., Spudis, P., Bussey, B., et al., 2011. The Lunar Mini-RF Radars: hybrid polarimetric architecture and initial results. Proceedings. IEEE 99, 808–823. doi:10.1109/JPROC.2010.2084970.

Reseau Map, 2003. http://www.hq.nasa.gov/alsj/alsj-reseau.html. The dimensions and spacings of the fiducial crosses and the size of the reseau plate given here allow the x,y coordinates of the crosses to be calculated.

Robinson, M.S., Jolliff, B.L., 2002. Apollo 17 landing site: topography, photometric corrections, and heterogeneity of the surrounding highland massifs. J. Geophys. Res. 107 (E11), 5110. doi:10.1029/2001JE001614.

Robinson, M.S., Byrlow, S.M., Tschimmel, M., et al., 2010. Lunar reconnaissance orbiter camera (LROC) instrument overview. Space Sci. Rev. doi:10.1007/s11214-010-9634-2.

Runcorn, S.K., 1994. The early magnetic-field and primeval satellite system of the Moon - clues to planetary formation. Philos. Trans. R. Soc. London, A 349, 181–196.

Schaeffer, O.A., Mueller, H.W., Grove, T.L., 1977. Laser Ar-39-Ar-40 study of Apollo 17 basalts. In: Merril, R.B. (Ed.), Lunar and Planetary Science Conference Proceedings, 8, pp. 1489–1499.

Schmitt, H.H., 1973. Apollo 17 report on the valley of Taurus–Littrow. Science 182, 681–690.

Schmitt, H.H., 1989. Lunar crustal strength and the large basin-KREEP connection. In: Taylor, G.J., Warren, P.H. (Eds.), Workshop on the Moon in Transition: Apollo 14, KREEP, and Evolved Lunar Rocks, Technical Report #89-03. Lunar and Planetary Institute, Houston, pp. 111–112.

Schmitt, H.H., 2003. Apollo 17 and the Moon. In: Mark, H. (Ed.), Encyclopedia of Space and Space Technology. Wiley, New York, p. 91. Chapter 1.

Schmitt, H.H., 2006. Return to the Moon. Springer, New York, pp. 89–92.

Schmitt, H.H., 2013. Field Geology on the Moon with Apollo 17: Results, Abstract, GSA Annual Meeting.

Schmitt, H.H., 2014. Apollo 17: new insights from the synthesis and integration of field notes, photo-documentation, and analytical data. Lunar and Planetary Conference 45. Lunar and Planetary Institute, Houston Abstract 2732.

Schmitt, H.H., Robinson, M.S., 2010. Geology of the Apollo 17 Taurus–Littrow site in light of LRO imagery. Geological Society of America Annual Meeting.

Schmitt, H.H., Cernan, E.AJones, E.M. (Ed.), 1972. Transcripts. Apollo Lunar Surf. J. <http://www.hq.nasa.gov/alsj/a17/a17.html>.

Schreve, R.L., 1968. The blackhawk debris flow. Geol. Soc. Am. 108, 1–48 Special Paper.

Scott, R.F., 1987. Failure. Geotechnique 37, 423–466.

Shea, E.K., Weiss, B.P., Cassata, W.S., Shuster, D.L., Tikoo, S.M., Gattacceca, J., Grove, T.L., Fuller, M.D., 2012. A long-lived lunar core dynamo. Science 335, 453–456. doi:10.1126/science.1215359.

Snape, J.F., Nemchin, A.A., Grange, M.L., Bellucci, J.J., Thiessen, F., Whitehouse, M.J., 2016. Phosphate ages in Apollo 14 breccias: resolving multiple impact events with high precision U–Pb SIMS analyses. Geochim. Cosmochim. Acta 174, 13–29.

Spudis, P.D., Wilhelms, D.E., Robinson, M.S., 2011. The sculptured hills of the Taurus highlands: implications for the relative age of Serenitatis, basin chronologies and the cratering history of the Moon. J. Geophys. Res. 116, E00H03. doi:10.1029/2011JE003903.

Staid, M.I., Pieters, C.M., Besse, S., et al., 2011. The mineralogy of late stage lunar volcanism as observed by the Moon mineralogy mapper on Chandrayaan-1. J. Geophys. Res. 116.

Steiger, R.H., Jäger, E., 1977. Subcommission on geochronology: Convention on the use of decay constants in geo- and cosmochronology. Earth and Planetary Science Letters 36, 359–362.

Stettler, A, Eberhardt, P., Geiss, J., Grogler, N., 1974. 39Ar–40Ar ages of samples from the Apollo 17 station 7 boulder and implications for its formation. Earth Planet. Sci. Lett. 23, 453–461.

Stettler, A., Eberhardt, P., Geiss, J., Grögler, N., Maurer, P., 1973. Ar39-Ar40 ages and Ar37-Ar38 exposure ages of lunar rocks. In: Lunar and Planetary Science Conference Proceedings, 4, p. 1865.

Stettler, A., Eberhardt, P., Geiss, J., Grogler, N., Guggisberg, S, 1978. Chronology of the Apollo 17 Station 7 Boulder and the South Serenitatis Impact. In: Lunar and Planetary Science Conference, 9, pp. 1113–1115.

Stuart-Alexamder, D.E., Howard, K.A., 1970. Lunar Maria and circular basins—a review. Icarus 12, 440–456.

Sugiura, N., Wu, Y.M., Strangway, D.W., Pearce, G.W., Taylor, L.A., 1979. A new magnetic paleointensity value for a "young lunar glass". In: Proceedings Lunar Planetary Science Conference 10, pp. 2189–2197.

Swann, G.A, Bailey, N.G., Batson, R.M., et al., 1972. Apollo 15 Preliminary Science Report NASA SP-289, 5-1–5-112.

Tatsumoto, M., Nunes, P.D., Knight, R.J., Hedge, C.E., Unruh, D.M., 1973. U-Th-Pb, Rb-Sr, and K measurements of two Apollo 17 samples. Eos 54, 614–615.

Tera, F., Papanastassiou, D.A., Wasserburg, G.J., 1974. Isotopic evidence for a terminal lunar cataclysm. Earth and Planetary Science Letters 22, 1.

Tera, F., Wasserburg, G.J., 1976. Lunar ball games and other sports. In: Abstracts of the Lunar Science Conference 7, pp. 858–860.

Turner, G., Cadogan, P.H., 1974. Possible effects of 39Ar recoil in 40Ar-39Ar dating. In: Lunar and Planetary Science Conference Proceedings, 5, pp. 1601–1615.

Turner, G., Cadogan, P.H., Yonge, C.J., 1973. Argon selenochronology. In: Lunar and Planetary Science Conference Proceedings, 4, p. 1889.

Turner, G., Cadogan, P.H., 1975. The history of lunar bombardment inferred from 40Ar-39Ar dating of highland rocks. In: Proceedings Lunar Science Conference 6, pp. 1509–1538.

Valentine, G.A., 1987. Stratified flow in pyroclastic surges. Bull. Volcanol. 49, 616–630.

Valverde, J.M., Castellanos, A., 2006. Compaction of fine powders: from fluidized agglomerates to primary particles. Gran. Matter 9, 19–24.

van der Bogert, C., Hiesinger, H.H., Banks, M.E., Watters, T.R., Robinson, M.S., 2012. Derivation of absolute model ages for lunar lobate scarps. Lunar and Planetary Science Conference 43 Abstract 1847.

van der Bogert, C.H, Gaddis, L., Hiesinger, H., Ivanov, M., Jolliff, B., Mahanti, P., Pasckert, J.H., 2016. Revisiting the csfds of the Taurus Littrow dark mantle deposit: implications for age determinations of pyroclastic deposits. LPSC 47 Abstract 1616.

Wagner, R.V., Nelson, D.M., Plescia, J.B., Robinson, M.S., Speyerer, E.J., Mazarico, E., 2017. Coordinates of anthropogenic features on the Moon. Icarus 283, 92–103.

Watters, T.R., et al., 2010. Evidence of Recent Thrust Faulting on the Moon Revealed by the Lunar Reconnaissance Orbiter Camera. Science 329, 936–940.

Weiss, B.P., Tikoo, S.M., 2014. The lunar dynamo. Science 346, 1198. doi:10.1126/science.1246753.

Wells, R.A., 2015. Apollo on the Moon in Perspective: 3D Anaglyph Composites Apollo 17 section, 224 http://americasuncommonsense.com/blog/editors/wells-downloads/.

Wilhelms, D.E., 1987. The Geologic History of the Moon. USGS Geological Survey Professional Paper 1348, p. 302.

Wolfe, E.W., Bailey, N.G., Lucchitta, B.K., Muehlberger, W.R., Scott, D.H., Sutton, R.L., Wilshire, H.G., 1981. The Geologic Investigation of the Taurus–Littrow Valley: Apollo 17 Landing Site. Geological Survey Professional Paper 1080, US Government Printing Office, p. 280.

Zuber, M., et al., 2010. The Lunar Reconnaissance Orbiter Laser Ranging Investigation. Space Science Reviews 150, 63–80.

Zuber, M.T., Smith, D.E., Watkins, M.M., et al., 2013. Gravity field of the Moon from the gravity recovery and interior laboratory (GRAIL) mission. Science 339, 668–671.